

Department of Exploration Geophysics

**Seismic characterization of Volcanogenic Massive Sulfides – The
Semblana Orebody, Portugal**

Sinem Yavuz

**This thesis is presented for the Degree of
Doctor of Philosophy
of
Curtin University**

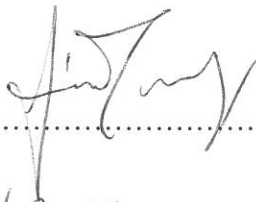
March 2015

Declaration

To the best of my knowledge and belief this thesis contains no material previously published by any other person except where due acknowledgment has been made.

This thesis contains no material, which has been accepted for the award of any other degree or diploma in any university.

Signature:

A handwritten signature in black ink, appearing to be 'J. J. J.', written over a dotted line.

Date:13/03/2015

To

Jai Kinkela,

and to my parents

Hediye & Haluk Yavuz

Abstract

Neves Corvo is one of the biggest mining districts on the Portuguese side of the Iberian Pyrite Belt. It hosts six different Lower Carboniferous copper, zinc, lead and tin orebodies, including Lombador, Neves, Graça, Corvo, Zambujal and Semblana. Extensive exploration has been undertaken for volcanogenic massive sulfide deposits at Neves Corvo during the past 50 years, where geological, geochemical and geophysical methods have all been applied. The principal geophysical methods employed include electromagnetic, earth resistivity and gravimetry techniques.

In 1996, a 2D seismic reflection survey was acquired over the Neves Corvo mine tenement, which imaged an amplitude anomaly related to the Lombador orebody. In 2011, initial elastic property measurements were conducted on numerous core samples to determine the seismic properties of the major formations of Neves Corvo as a step towards further derisking the seismic reflection technique. A significant acoustic impedance contrast was observed when comparing mineralisation relative to the surrounding host rocks, which provided the basis to acquire a 3D seismic reflection survey. The objectives of this survey were to image known deep volcanogenic massive sulfide mineralisation to categorically validate the seismic reflection technique as well as to potentially identify new mineralisation targets.

Based on the results of the 3D seismic survey acquired over the Neves Corvo mine and its south-eastern extents, the Semblana and Lombador deposits were unambiguously imaged, along with key lithological contacts and geologic structures. Additionally, copper sulfide extensions south of Semblana were discovered. A number of high-priority targets were identified from the seismic data predominantly based on amplitude strength and which were subsequently drilled. Unfortunately,

most of them were found to be non-mineralised. This result raised the question of amplitude non-uniqueness within the original seismic data and how lithologies of weakly contrasting acoustic impedances in contact with one another could appear as relatively strong reflectors.

The main objective of this study was to overcome the amplitude non-uniqueness issue by establishing a comprehensive methodology inspired by routine soft rock seismic processing applications. The end result would better delineate the major geological structures and further discriminate massive sulfide from other non-mineralised lithologies. A well-defined seismic understanding of the geology was established with the addition of comprehensive elastic property measurements. The full waveform sonic and pseudo logs were then used to model different interfaces and calibrate the seismic data. These results indicated that preserved relative amplitude processing might be of importance in helping to reduce the ambiguity in the direct detection and targeting of volcanogenic massive sulfides based on seismic amplitude anomalies.

The customized relative amplitude processing of a sub dataset over the Semblana deposit was then performed. The newly obtained seismic cube was calibrated with existing drillholes and a volumetric interpretation was performed utilising amplitude-based geobodies. Eventually, superior target zonation and precision was achieved with the revised interpretation clearly showing that the high priority targets originally identified from the legacy data would not have passed the targeting criteria in the reprocessed data due to their relatively weak amplitude response. The results obtained from this study inspired the subsequent reprocessing of the full seismic dataset.

In the final step, a quantitative interpretation of the Semblana deposit's seismic response was carried out through the application of acoustic and elastic impedance inversion as well as the AVO analysis. The model based acoustic impedance inversion was utilized to obtain additional information related to lithology. AVO and AVO attribute analysis were performed to demonstrate the unique nature of the massive sulfide response. Finally, an elastic impedance inversion on partial stacks verified the unique distribution of massive sulfides.

Acknowledgements

I would like to thank to my supervisors Milovan Urosevic, Andrej Bona and Roman Pevzner for their outstanding supervision and continued support.

I would like to thank Lundin Mining Corporation for granting permission to use their data and continued support. I would like to particularly thank Dick West - Exploration Technology and Group Resources Director of Lundin Mining Corporation - for providing to me the opportunity to work on this project and for valuable suggestions and comments when reviewing my work.

I would like to thank HiSeis Pty Ltd for providing access to the data and continued support. I am grateful to Don Pridmore - CEO of HiSeis Pty Ltd - for providing to me the opportunity to work on this project and for many hours of discussion, insight and assistance while undertaking this project. His expertise and supervision have been invaluable during this work.

I am grateful to Aleksandar Dzunic for sharing his experience in seismic processing and numerous insightful discussions. I am grateful to Maxim Lebedev, J. Christian Dupuis and Andrew Greenwood for their valuable technical assistance and shrewd comments in times of need.

Core samples for the elastic property measurements were provided by Lundin Mining Corporation. The measurements were performed in the rock physics laboratory under the supervision and help of Maxim Lebedev and Andrew Greenwood.

The high-resolution 3D Neves Corvo seismic dataset was acquired by HiSeis Pty Ltd on behalf of Lundin Mining Corporation in February-April 2011. Initial conventional data processing of the Neves Corvo seismic dataset was carried out by HiSeis Pty Ltd in September 2011 and preserved relative amplitude processing of the same dataset was finalized in June 2013 by HiSeis Pty Ltd.

I would like to acknowledge the Department of Exploration Geophysics and Curtin University for financial support through a Curtin University International Postgraduate Research Scholarship (CIPRS), the Cooperative Research Centre for Landscape Environments and Mineral Exploration (CRC LEME) for financial support through a top-up scholarship and the Australian Society of Exploration Geophysicists (ASEG) Research Foundation for providing a three year research grant to perform laboratory measurements, purchase the licenses for necessary software and to attend workshops and conferences.

The work has been supported by the Deep Exploration Technologies Cooperative Research Centre, whose activities are funded by the Australian Government's Cooperative Research Centre Programme. This is DET CRC Document 2015/666.

I am also grateful to Landmark Graphics - a Halliburton Company, Paradigm, Hampson & Russell - a CGG company and Golden Software Inc. for providing software packages under their university program grants.

My special thanks go to Lee and Frank Kinkela, Olivia Collet, Ugur Ekinici, Serra and Levent Yavuz for their continued and unwavering encouragement and support. I couldn't have asked for a better family than this.

Contents

Abstract	I
Acknowledgements	III
Contents	V
List of Figures	VII
List of Tables	X
List of Abbreviations	XI
1 Chapter 1 Introduction	1
1.1 Seismic Methods for Copper Exploration.....	5
1.2 Motivation and Research Objectives.....	9
1.3 Thesis Outline	13
2 Chapter 2 Seismic for Minerals – Processing and Data Analysis	15
2.1 Surface-Consistent Amplitude Corrections.....	16
2.2 Surface-Consistent Deconvolution.....	19
2.3 Surface-Consistent Residual Static Corrections.....	21
2.4 Linear Radon Transform	25
2.5 Kirchhoff Migration	26
2.6 AVO Analysis and Elastic Impedance Inversion.....	28
3 Chapter 3 Geological Setting and Rock Physics	32
3.1 Geological Setting.....	33
3.1.1 Iberian Pyrite Belt.....	35
3.1.2 Neves Corvo Mine	36
3.1.3 Semblana Ore Body	37
3.1.4 Lithology.....	39
3.2 Elastic property measurements.....	43
3.3 Drillhole Data Calibration.....	49
3.4 Summary	56

4 Chapter 4 Preserved Relative Amplitude Processing	57
4.1 Seismic Data Acquisition	58
4.2 Conventional Data Processing and Interpretation	61
4.3 Preserved Relative Amplitude Processing	64
4.3.1 Data Conditioning	66
4.3.2 Surface-Consistent Amplitude and Deconvolution	68
4.3.3 Radon Filter	69
4.3.4 Surface-Consistent Residual Static Corrections	73
4.3.5 Interactive Velocity Analysis.....	75
4.3.6 Pre-stack Kirchhoff 3D Time Migration	77
4.4 Volumetric Interpretation	79
4.5 Discussions and Conclusions	85
5 Chapter 5 Seismic Characterization of the Semblana Orebody	87
5.1 Acoustic Impedance Inversion	87
5.1.1 Database Creation and Correlation	89
5.1.2 Model Building	93
5.1.3 Inversion Analysis	96
5.1.4 Inversion and Interpretation.....	97
5.2 AVO Analysis	99
5.2.1 AVO attributes	105
5.2.2 Partial Stacking	109
5.3 Elastic Impedance Inversion	111
5.3.1 Near-offset and Far-offset Inversion.....	111
5.3.2 Crossplots.....	115
5.4 Discussion and Conclusions	117
6 Chapter 6 Discussions and Conclusions	120
6.1 Further work	123
References	125
Appendix	136
Copyright consent	136

List of Figures

Figure 1.1 World map showing the locations of existing 2D and 3D hard-rock seismic surveys.	5
Figure 1.2 Location Map (above) and a cross-section through the Semblana ore body (below).	12
Figure 2.1 Source and receiver locations and principal trace organizations.	17
Figure 2.2 Surface diagrams.....	22
Figure 2.3 Super trace cross-correlation for the stack power maximization method.	24
Figure 2.4 The map of several arrivals on both the CMP gather and the corresponding τ - p gather.	26
Figure 3.1 Geological map of the Iberian Pyrite Belt over the South Portuguese Zone with selected massive sulfide deposits and the main geological units displayed.	34
Figure 3.2 3D View of the Neves Corvo mine.....	37
Figure 3.3 Acoustic properties of the most common crystalline rocks and ore mixtures.....	38
Figure 3.4 Tectono-stratigraphic sequence of the Neves Corvo mine area	42
Figure 3.5 The set-up for ultrasonic velocity measurements at atmospheric pressure.	44
Figure 3.6 The NQ size samples of PSJ50, including a) massive sulfide, b) stockworks and c) rhyolite samples	45
Figure 3.7 A P-wave velocity and density cross-plot.....	47
Figure 3.8 Acoustic and elastic impedance cross-plot	48
Figure 3.9 Drillhole PSJ50 (a) FWS and pseudo log correlation and (b) drillhole-to-seismic tie.....	51
Figure 3.10 Drillhole-to-seismic tie of: (a) PSK50 and (b) SZ24A.....	54
Figure 3.11 Drillhole-to-seismic tie of: (a) PSK48 and (b) PSO44.....	55
Figure 4.1 Plan view of the seismic data acquisition area.	60

Figure 4.2 Semblana sub-data set CDP fold map overlapped with the source and receiver lines coloured by elevation.....	61
Figure 4.3 Signal-to-noise ratio analysis diagrams displaying the RMS values of amplitudes	67
Figure 4.4 The interactive radon (τ -P) analysis for shot number 1776.....	70
Figure 4.5 (a) A raw 3D shot gather and (b) the same gather after pre-processing..	71
Figure 4.6 In-line 61 after the application of a Radon filter for the attenuation of ground roll and guided wave in the CDP domain.	72
Figure 4.7 Surface-consistent residual static correction comparison.....	74
Figure 4.8 Interactive velocity analysis.....	76
Figure 4.9 Impulse response test for the determination of migration aperture and dip angle	78
Figure 4.10 PRA processed Semblana sub-dataset with selected a) inlines and b) crosslines displayed.....	79
Figure 4.11 PRA processed Semblana sub-dataset with depth slices	80
Figure 4.12 Comparison of a) PRA and b) AGC processing results on selected inlines.....	82
Figure 4.13 a) 3D view of the intersection of orthogonal sections of the PRA (SE – NW) and AGC (SW-NE) processed cubes and b) with superimposed wireframes...	83
Figure 4.14 Comparison of AGC and PRA approaches through the generation of iso-shells.....	84
Figure 5.1 a) The seismic section for crossline 46 and b) its location in green on the base map.....	91
Figure 5.2 The interpolated time slices for the a) CULM and b) Neves Corvo thrust marker horizons.....	92
Figure 5.3 a) The initial P-wave velocity and b) density model cubes for crossline 46.....	94
Figure 5.4 a) The initial P-impedance model and b) synthetic seismic cubes for crossline 46.	95
Figure 5.5 The error analysis for drillhole PSJ50.	96
Figure 5.6 The acoustic impedance inversion results	98
Figure 5.7 An example of how a 3D CDP supergather is created.	100
Figure 5.8 A CDP supergather example for inline 62.....	101
Figure 5.9 a) The interpolated time slice for the horizon corresponding to the Semblana orebody and b) the RMS amplitude variation for the same horizon.....	102
Figure 5.10 An axample AVO analysis on CDP supergather	103
Figure 5.11 Target A & Target B are overlain on a) PRA and b) AGC crossline 51. The CDP supergather which sits on crossline 51 underwent an interactive AVO analysis as shown in c)	104

Figure 5.12 The variation of a) intercept, b) gradient, c) curvature and d) scaled Poisson's ratio changes over the AVO horizon.	106
Figure 5.13 The variation of relative a) V_p , b) V_s and c) density changes over the AVO horizon.	107
Figure 5.14 Variation of AVO attributes in 3D.	108
Figure 5.15 a) Near offset (0-500 m) and b) far-offset (500-1750 m) stacks for inline 62.	110
Figure 5.16 Near offset elastic impedance inversion cube.	113
Figure 5.17 Far offset elastic impedance inversion cube.	114
Figure 5.18 Crossplots of the elastic impedance inversion results with seismic sections.	116

List of Tables

Table 1.1 Summary of main copper deposit types.	6
Table 4.1 Acquisition parameters for PRA processing of the Semblana sub-dataset.	59
Table 4.2 AGC processing flow	63
Table 4.3. PRA processing flow	65
Table 5.1 3D CDP supergather creation parameters.	100

List of Abbreviations

3D	Three dimensional
2D	Two dimensional
VMS	Volcanogenic massive sulfide
TEM	Transient electromagnetic
IP	Induced polarization
FWS	Full waveform sonic
PRA	Preserved relative amplitude
AVO	Amplitude versus offset
PSTM	Pre-stack time migration
CDP	Common depth point
NMO	Normal move-out
CMP	Common mid-point
RMS	Root mean square
DMO	Dip move-out
P-wave	Primary (compressional) wave
S-wave	Secondary (shear) wave
AGC	Automatic gain control

CVS	Constant velocity stack
QC	Quality control
VSP	Vertical seismic profiling

Chapter 1

Introduction

Since the beginning of civilization, mining has played a key role in sustaining the existence and evolution of humankind. As time has passed, mineral exploration has become more and more important to humanity. Mineral exploration can be described as the process of exploring the commercially valuable minerals or other geological materials from on or above the earth. From a wider perspective, it also includes the exploration of any hydrocarbon resource such as petroleum, natural gas, or even water. The challenges of modern mineral exploration in hard rock terrains are very well-known, particularly in the fields of area selection, risk assessment, target generation, resource evaluation, reserve definition and extraction. To aid these fields, geological, geophysical and geochemical methods have been used to assist in mineral exploration both separately and collaboratively.

Exploration geophysics plays an important role in the target generation phase. One of the most efficient and most common methods of geophysical prospecting in mineralised environments has been the use of airborne geophysics (Nabighian and Asten 2002). Mineral exploration has also largely focused on the time and cost-effective earth-resistivity, magnetic and gravimetry methods, which have proven to be successful at detecting shallow targets (Telford *et al.* 1990). Another powerful geophysical prospecting technique is reflection seismology, which has been successfully utilized as the primary exploration technique in hydrocarbon exploration

for the last century. However, mineral exploration couldn't reap the same benefits as the petroleum industry from seismic due to several factors. These issues include such as complex three dimensional (3D) geology, complex faulting and fractures of all scales highly variable intrusive geometries, high attenuation, high scattering, highly variable inhomogeneity, ground roll and guided waves, weathered cover (regolith) and an intrinsically low signal-to-noise ratio (Malehmir *et al.* 2012b; Pretorius *et al.* 2003 ; Urosevic 2013).

In the last decade, the significant increase in mineral commodity prices and conversely the considerable decrease in the number of large and shallow mineral deposit discoveries have obligated the mineral industry to explore at greater depths. Among all the geophysical methods, it is reflection seismology that offers the most promise in achieving this goal due to its comparably great depth penetration and high resolution. The application of seismic reflection surveys on an experimental basis in mine planning, site characterizations and mineral exploration has been long known. Since the early 50's, various surface and downhole seismic reflection techniques has been tested in the exploration of numerous minerals such as iron, gold, silver, nickel, copper, potash, kimberlites, (e.g., Schmidt 1959; Gendzwill 1990; Juhlin *et al.* 1991; Friedel *et al.* 1995; Friedel *et al.* 1996; Urosevic and Evans 1998; Urosevic and Evans 2000; Perron *et al.* 2003; Chen *et al.* 2004). A great amount of effort has also been invested in tests for the cross-hole methods and on research into the determination of the elastic and mechanical properties of the rock mass (e.g. Cosma 1983; Wong *et al.* 1983; Gustavsson *et al.* 1984; Duncan *et al.* 1989; Young *et al.* 1989; Cao and Greenhalgh 1997). As reported in Gupta (1972), Ruskey (1981), Gladwin (1982), Maxwell and Young (1992), Frappa and Molinier (1993), Bierbaum and Greenhalgh (1998) and Duweke *et al.* (2002), many different seismic techniques, survey designs and source types has also been evaluated in an attempt to optimize mine safety, design and planning for the exploitation of mineral resources.

There were numerous deep and large-scale seismic research projects carried out in between 1850 and 2005, with an overview provided by Prodehl and Mooney (2012) in a compendium of controlled-source seismic studies of the earth's crust. These studies cover most of the controlled-source seismic research projects from around the world, including important studies from Europe (EUROPROBE), the USA (COCORP), Canada (LITHOPROBE), South America (SALIERI), Russia

(GRANIT), India (HIMPROBE), China (National DSS programme), South Africa (National Geophysics Programme) and Australia (ACORP). These have significantly contributed to the development of seismic techniques designed to delineate complex geologic structures in the crystalline environment (Ruskey 1981; Odgers and du Plessis 1993; Clowes *et al.* 1996; Juhlin *et al.* 1996; Milkereit *et al.* 1996; Singh 2004; Sallarès *et al.* 2005; Li *et al.* 2006; Eaton *et al.* 2010; Finlayson 2010). Another important contribution to hard rock seismic imaging was achieved with the successful characterization of nuclear-waste repository sites through fault and fracture zone imaging (Juhlin *et al.* 1991; Brocher *et al.* 1998; Juhlin and Stephens 2006). As it was first reported in Salisbury *et al.* (1996), the systematic petrophysical measurements during the Lithoprobe project on massive sulfide deposits and their host rock showed that the acoustic impedance contrast is highly dependent on the grade and the mineralogy of the target. This study also demonstrated the significance of the identification of the acoustic impedance contrast through petrophysical measurements for successful seismic imaging in base metal exploration.

In order to answer the question as to whether or not orebodies themselves could be imaged directly (Dahle *et al.* 1985), extra effort has been spent on considering the size and geometry of the target mineralization and on synthetic modelling to understand the possible seismic response (Adam *et al.* 1996; Bohlen *et al.* 2003, Bellefleur *et al.* 2012 and Greenhalgh and Manukyan 2013). Signal-to-noise ratios in hard rock seismic have also been improved with the attuned seismic acquisition and processing parameters that have been investigated through these modelling studies. Further advancement in hard rock seismic imaging has been achieved through downhole (e.g., Greenwood 2013) and in-mine seismic surveys that have been used to delineate steeply dipping geological structures. Their higher resolutions compare to surface seismic methods allow them to better image the more complex structures such as fractures and fault zones. Moreover, they could provide information to build better constructed velocity fields that would enable the application of more rigorous seismic data processing algorithms such as pre-stack time and depth migrations (Malehmir *et al.* 2012b). As reported in Eaton *et al.* (2003a) and overviewed in Eaton *et al.* 2003b, the collaboration of well integrated petrophysical measurements performed both in the drillholes and in the laboratory, downhole logging, two

dimensional (2D) and 3D modelling and surface seismic could aid in fine tuning the constraints of seismic interpretation and drastically increase the success of hard rock seismic exploration. As it was first reported in Matthews (2002) the very first blind discovery of a deep massive sulfide deposit succeeded through this integrated approach in the Halfmile Lake area, Canada. In Australia, 2D and 3D seismic reflection exploration programs were organised by the Curtin Department of Exploration Geophysics through MERIWA 363 grants, which included investigations in several mine sites (Urosevic *et al.* 2007). Many more integrated efforts in mineral exploration are also reported by several authors in Australia (e.g., Goleby *et al.* 2002; Urosevic *et al.* 2002; Evans *et al.* 2003; Harrison *et al.* 2007; Urosevic and Juhlin 2007; Yavuz *et al.* 2012), in Canada (e.g., Wu *et al.* 1995; Adam *et al.* 1997; Calvert and Li 1999; Erick *et al.* 2003; Adam *et al.* 2004) and in Europe (e.g., Malehmir *et al.* 2009; Malehmir *et al.* 2011; Malehmir *et al.* 2012a; Dehghannejad *et al.* 2012; Yavuz *et al.* 2013; Yavuz *et al.* 2014).

All the recent advancements made in the application of the seismic technique along with the reduction in equipment cost have made both surface and downhole seismic surveys become a viable alternative to blind target exploration by blanket drilling and also an important driving force for the subsequent deep drilling of targets identified from seismic data. As stated in Malehmir *et al.* (2012b), until now there have been several 2D and 3D surface seismic surveys acquired all around the world for the purpose of mineral exploration (Figure 1.1).

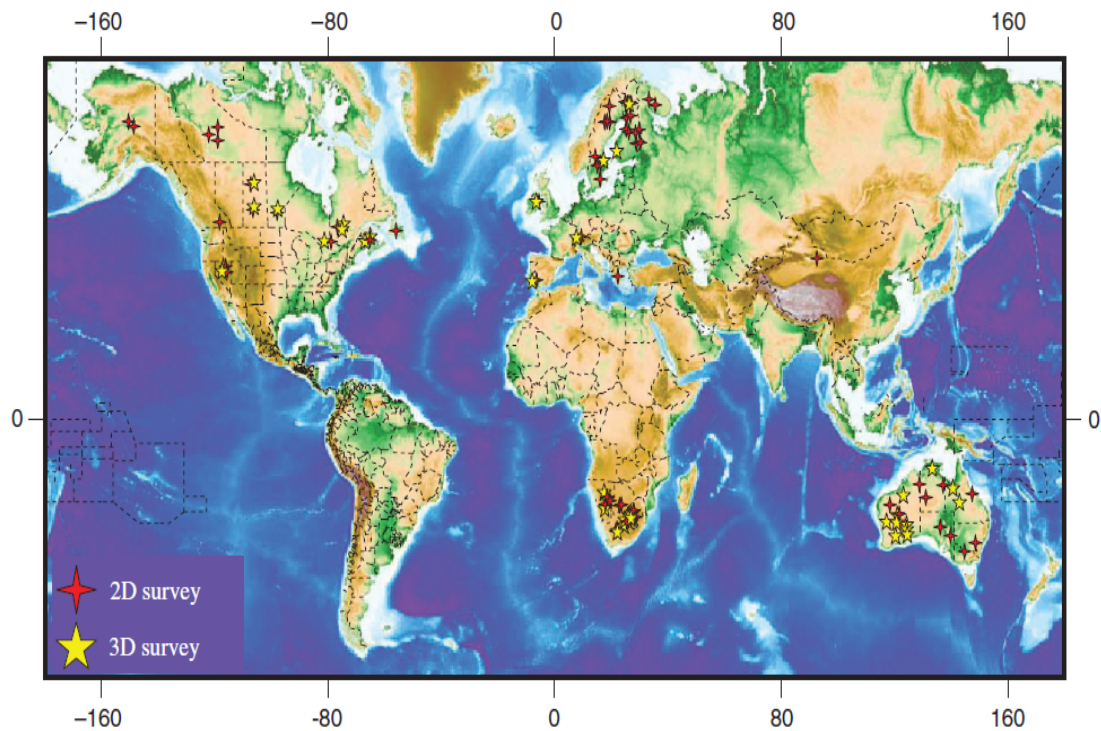


Figure 1.1 World map showing the locations of existing 2D and 3D hard-rock seismic surveys. These surveys were conducted for mineral exploration, site characterizations, and mine planning (After Malehmir *et al.* 2012b).

1.1 Seismic Methods for Copper Exploration

Copper, with its reddish brown colour, is a non-ferrous base metal and is one of the best conductors of electricity and heat. Many archaeological digs from all over the world have signified that copper was one of the first metals to have been used by humans. Beginning over 10,000 years ago, it can be found in weapons, utensils and jewellery. Copper is one of the most ductile and malleable metals and can easily be worked to serve many purposes in modern life such as in the creation of coins, jewellery, architecture, building wire, plumbing and heating, automotive, power utilities, air conditioning and refrigeration, and telecommunication. Copper bearing metal alloys have also been used in several different ways by industrialized nations, which has consequently maintained the demand for the metal to be very high. There are a few types of mineral deposits that contain copper and are found in different geological environments worldwide. Globally, the hydrothermal deposits form the major copper resources, although magmatic and supergene deposits are also important on a local scale. However, these are of limited economic importance. The main copper deposit types are summarized in Table 1.1.

Table 1.1 Summary of main copper deposit types. (Adopted from NERC BGS (2007).)

Deposit type	Synonyms	Description	Examples
Porphyry		Large, relatively low-grade stockwork disseminated related to intrusions to deposits	Chuquicamata and La Escondida, Chile; Bingham Canyon, USA; Grasberg, Indonesia
Sediment-hosted	Shale-hosted copper, stratiform copper, Kupferschiefer-type, Central African type	Stratabound disseminations of copper minerals occurring in a range of sedimentary rocks	Nchanga, Zambia; Lubin, Poland; White Pine, USA
Red-bed	Sandstone-hosted, continental red-bed, basaltic copper, volcanic-hosted copper, copper mantos	Copper mineralisation occurring in oxidised zones in sedimentary (s) and volcanic (v) rocks	Dzhezkazgan (s), Kazakhstan; Mantos Blancos (v), Chile
Volcanogenic massive sulphide (VMS)	Volcanic-associated, volcano-sedimentary-hosted massive sulphide deposits	Mineralisation hosted by submarine volcano-sedimentary sequences	Bathurst and Kidd Creek, Canada; Rio Tinto, Spain
Magmatic sulphide deposits		Sulphide concentrations associated with a variety of mafic and ultramafic magmatic rocks	Sudbury and Voisey's Bay, Canada; Noril'sk-Talnakh, Russia; Kambalda, Australia
Sedimentary exhalative (SEDEX)		Bodies of polymetallic sulphides deposited from hydrothermal fluids vented into sedimentary basins with no obvious volcanic source	Damaran Supergroup, Zambia; Red Dog, Alaska
Epithermal		Veins, stockworks and breccias associated with high-level or near surface volcanic-related low-temperature hydrothermal systems	El Indio, Chile; Lepanto, Philippines; Monywa, Burma.
Copper skarns	Contact metasomatic copper deposits	Mineralisation formed by chemical alteration associated with intrusions into carbonate rocks	Ok Tedi, Papua New Guinea; Copper Canyon, USA; Rosita, Nicaragua
Vein-style deposits	Polymetallic veins	Mineralised structures often developed along fractures varying from centimetres up to tens of metres wide from a variety of sources	El Indio, Chile; Olympic Dam and Hillside (IOCG), Copper Hills, Australia; Butte, USA
Supergene		In-situ natural secondary enrichment of primary mineralisation	Erdenet, Mongolia; La Escondida, Chile; Sarcheshmeh, Iran

The world's major source of copper, which accounts for approximately 60% of the world's production, are composed of porphyry copper deposits which also contain molybdenum, rhenium, gold, silver and tin as well as a range of by-product metals. Porphyry deposits occur in plate boundary collision areas as they are associated with subduction-related felsic igneous intrusions. In porphyry deposits, a core of severe

alteration passages in the host rock formed by other secondary alteration minerals is the typical zones of mineralisation (McMillan and Panteleyev 1988). A stockwork of quartz veins and breccias contain the fracture-controlled mineralisation that bears the copper sulfides and by-product metals. Porphyry deposits, with their enormous sizes, contain fairly high amounts of ore with a copper grade generally ranging from 0.2 to 1 per cent.

The world's second biggest sources of copper, with around 20% of the world's production, are the sediment-hosted deposits. They are also the world's main source of cobalt and one of the most important sources of lead, zinc and silver. These deposits comprise fine-grained disseminations of sulfide in different types of sedimentary rocks, such as sandstone, limestone and black shale (Gustafson and Williams 1981; Cox *et al.* 2003). Their sizes differ from the average of 20 million tonnes to several hundred million tonnes with an average copper grading of 2%.

Red-bed copper deposits are another worldwide source of copper. They can be found as two different types depending on their host rocks. The disseminations of sulfide occur in permeable volcanoclastic sedimentary rocks that are formed as mafic lava flows and are associated with volcanic-hosted red-bed copper deposits (Van Houten 1973). The volcanic-hosted red-bed copper deposits are an economically important source of copper due to both their size and grading, which can range from hundreds of thousands to hundreds of millions of tonnes at 1 - 4% respectively. In contrast, the sedimentary-hosted red-bed deposits are generally considered non-economic sources of copper due to their small size. These are formed by oxygen-rich fluids rising through red continental sediments and consist of disseminated sulfides, which accumulate in the permeable layers.

Volcanogenic massive sulfide (VMS) deposits are another important source of copper, as other precious metals such as gold and silver. VMS deposits have significant sizes that range from hundreds of thousands tonnes and up to half a billion tonnes with relatively high grades. The comparably large ore bodies associated with VMS deposits are seen as stratiform lenses and sheets that are generated by metal-rich hydrothermal fluid flows that permeate through marine-based volcanogenic rocks, which are formed at oceanic spreading centres (Barrie and Hannington 1999; Galley *et al.* 2007). Strata and time-bound VMS bodies are

associated with specific stratigraphic sequences underlain by a stockwork feeder zone within a province and are likely to occur in distinct lithological suites (Klemm and Schneider 1977; Morgan 2012; Shanks and Thurston 2012).

The last economically important type of copper deposit is the magmatic sulfide deposit, which contains copper along with nickel and platinum-group elements. When the sulphur content of the magma rise is sufficient, a distinct liquid sulfide phase can occur, which transforms elements such as nickel, copper, platinum-group elements and iron from the sulfide phase into the mafic and ultramafic rocks. Global deposit sizes vary from a few hundred thousand tonnes to tens of millions of tonnes with copper grade of 0.2-2%.

Copper can also be seen as a major by-product in sedimentary exhalative and epithermal deposits. Additionally, while the skarn coppers are associated with porphyry copper deposits, the vein-type deposits are intimately associated with the other major copper deposit styles.

To date, the exploration of copper deposits has been mainly carried out through an understanding of the geology and drilling. These primary discovery methods were assisted with several different geophysical and geochemical techniques. As discussed in Holliday and Cooke (2007) geophysics has assisted in the exploration of porphyry copper deposits as a contributory discovery method through such techniques as magnetic, transient electromagnetic (TEM) and induced polarization (IP). Despite complex geology with a thick weathered layer and steeply dipping structures, the strong alteration zones as well as the typical deposit dimensions of porphyry copper deposits have allowed the seismic method to be used as an effective exploration tool. The proper consideration of the target followed by a modelling study can increase the chance of success of seismic surveys, which could provide valuable information in the delineation of faults and other geological structures as well as to directly detect the orebodies themselves (e.g., Roy and Clowes 2000; Li and Eaton 2005; Jones 2008). An example of this was reported in Milkereit *et al.* (1992), where a 2D seismic reflection study was able to overcome issues related to complex geological geometries in order to image the major geological structures as well as assist in the orebody delineation of a Ni-Cu deposit located in the Sudbury magmatic sulfide complex.

In other examples, despite a thick layer of cover, there are a number of instances where seismic refraction and reflection surveys have been successfully implemented to aid in the exploration of vein-style Pb-Zn-Cu deposits (e.g., Hawkins and Whiteley 1980; Nelson 1984). Additionally, some special seismic techniques such as refraction tomography, multichannel analysis of surface waves, s-wave imaging and diffraction imaging were combined with conventional reflection seismic to contribute to the exploration of various iron oxide copper gold deposits such as Olympic Dam (e.g., Rutter and Esdale 1985; Drummond *et al.* 2006; Korsch and Kositsin 2010) and Hillside (e.g., Yavuz *et al.* 2012; Bona *et al.* 2013; Tertyshnikov 2014), which are well-known and contain extremely complex geology, shear zones and steeply dipping structures.

Similarly, in the right geological setting VMS deposits can provide favourable seismic targets. This can be attributed to its anomalously high density (high ore concentration), the specific geometry of the orebody and association with iron oxide (particularly pyrites) that produce impedance values much higher than that of the host rock. Compared to all the other stated deposits above, high-resolution seismic imaging has been utilized the most in VMS exploration in order to detect and delineate deep massive sulfide deposits as well as to image important lithological contacts and geologic structures (e.g., Dahle *et al.* 1985; Read 1989; Spencer *et al.* 1993; Milkereit *et al.* 1996; Milkereit *et al.* 2000; Eaton *et al.* 2003b; Urosevic *et al.* 2012).

1.2 Motivation and Research Objectives

This study focuses on the Iberian Pyrite Belt, which has been one of Europe's major metallogenic provinces with a history of over 3000 years of mining activity. The VMS deposits of the Iberian Pyrite Belt have been the subject of intensive geological and geophysical exploration activities during the past 50 years (Strauss *et al.* 1977). Since 1960, geophysical methods such as airborne electromagnetic, earth resistivity, induced polarization and gravimetry were utilized to assist in the geological and geochemical exploration of nearly all the VMS deposits of the region. One of the largest mines in the Iberian Pyrite Belt is Neves Corvo, which is located on the Portugal side of the South Portuguese Zone. Semblana – a high-grade copper rich

orebody –is one of six massive sulfide lenses associated with the Neves Corvo mine and is the specific focus of this study.

The area over the Semblana orebody was originally considered prospective primarily due to a priori geological knowledge as its location coincided with the down dip geological extension of the Zambujal orebody and along strike of the Corvo orebody. This area was also adjacent to gravity and TEM anomalies (Meyer and Owen 2013). The discovery was based on a drill hole targeting an off-hole TEM anomaly. In addition to the conventional mineral exploration methods, in 1996 2D seismic reflection profiling was also utilized in the exploration of the area surrounding the Neves Corvo mine and provided an amplitude anomaly related to Lombador orebody (O'Brien and West 2013).

In 2011, a high-resolution 3D seismic reflection survey was successfully acquired to better delineate the known deep massive sulfide deposits (Lombador and Semblana) as well as to detect new targets in the vicinity of the Neves-Corvo mine, Portugal. The main result of the survey was that Semblana and Lombador massive sulfide orebodies were clearly imaged as well as the structures associated with them. Subsequently, copper sulfide extensions south of Semblana were discovered with drilling based on the seismic data (Lundin Mining Corporation 2013). The survey was also successful in detecting important lithological contacts and geological structures allowing mapping out the prospective stratigraphy. However, all of the high-priority targets that were identified by anomalously high amplitude responses were drilled and many of them were found to be non-economic rhyolites (Figure 1.2).

The problem of non-unique amplitude responses from two very different lithological contacts has been discussed by Taner and Koehler (1981) and Eaton *et al.* (1997). This same issue has motivated our study. It became necessary to further analyse and understand the seismic response of the mineralised system in order to properly utilize the information provided by the 3D seismic. Therefore, the main objective of this study became to mitigate the issue of non-uniqueness in order to discriminate the seismic response of massive sulfide from the other lithologies and to better delineate the major geological structures in the area. As such, this study is of importance to

future seismic surveying not only of the entire Iberian Pyrite Belt, but for VMS exploration worldwide.

The first step was to establish the prerequisite geological understanding and to create a database of the elastic properties of the major lithological units. Laboratory measurements on core samples from the Neves Corvo mine site provided crucial quantitative petrophysical properties such as acoustic and elastic impedances, with the latter being first introduced by Connolly (1998). These could be utilized to infer geo-mechanical properties of the ore and surrounding major formations. The first attempt at using elastic impedances for hard rock seismic characterisation was done by Harrison (2009) on a 2D seismic dataset. This study presents the first attempt to utilise elastic impedances for hard rock seismic characterisation from 3D seismic reflection data. Since such an approach was previously untested by the research community, it was necessary to include numerical simulations in evaluating the results of the field data analysis. For the numerical computations both full waveform sonic (FWS) and pseudo log data were utilised in order to obtain a reliable synthetic seismic response that can be correlated and tied to the 3D surface seismic response. The high correlation between the FWS and pseudo log data from this modelling study also showed that in the right setting, the cost and time effective pseudo logs could replace the expensive FWS logs. This has the potential to significantly advance the application of seismic imaging through more frequent drillhole-to-seismic ties and therefore a more accurate representation of the seismic velocities.

Afterwards, through preserved relative amplitude (PRA) processing of the 3D seismic data, the reflectivity non-uniqueness issue was addressed to make direct targeting of mineralisation from surface seismic data more reliable. This study is the first known application of full PRA processing on a 3D hard rock seismic dataset (Malehmir *et al.* 2012b). As such, the subsequent success of the PRA processing would be evaluated through a volumetric interpretation of the seismic data set utilizing mineralisation wireframes, interpreted geological surfaces and iso-shells. This study shows very encouraging results of the first known application of PRA processing on 3D hard rock seismic data.

The following step was to generate an acoustic impedance cube from the seismic data using a model based inversion so that it can be used as a crucial aid to the

comprehensive volumetric interpretation for the purpose of direct mineral targeting. Finally, an amplitude versus offset (AVO) analysis and elastic inversion were performed on the pre-stack seismic data to fine-tune the seismic response over the Semblana deposit. The very first known application of AVO analysis on 3D hard rock seismic data, followed by an elastic impedance inversion, was used to help discriminate the copper sulfides from other non-economical lithologies (including disseminated mineralization).

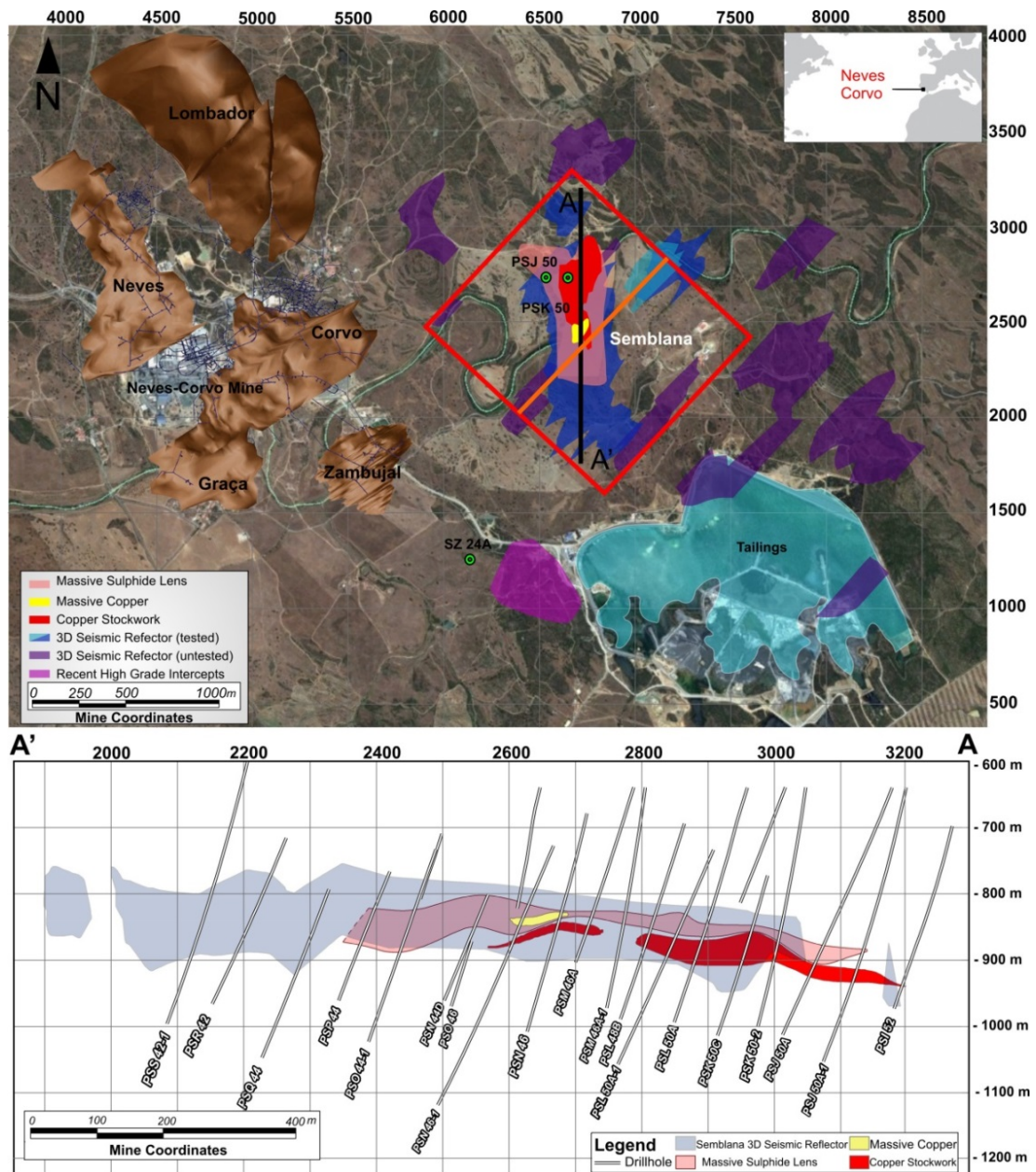


Figure 1.2 Location Map (above) and a cross-section through the Semblana ore body (below). The Neves Corvo ore bodies and the tailings dam are shown on the location map, as well as the massive sulfide lens (pink), massive copper (yellow), copper

stockwork (red) and 3D seismic reflectors (purple). All the mineralized zones were generated with the drillhole data. The study area (red rectangle), some drillholes (green dots), the cross section below (black line) are highlighted on the location map. Both maps are displayed in mine coordinates. While the massive sulfide lens consists mainly of copper, zinc, lead, silver, gold and tin, the massive copper lens consists of high grade copper. The initial technical success of the seismic reflection survey is obvious through a significant match between the Semblana 3D seismic reflector and the massive sulfide lens, massive copper, copper stockworks and several drill holes. On the other hand, the cross-section also revealed the amplitude non-uniqueness issue and the necessity of PRA processing. (Courtesy of Lundin Mining Corporation, 2012).

1.3 Thesis Outline

Including this introduction, this thesis consists of six chapters. The content of these chapters are organized as the following:

Chapter 2 - An overview into the theoretical background and basic concepts of hard rock seismic imaging. Also covered are the principals of the major PRA processing steps, acoustic and elastic inversion and AVO analysis. These approaches provide the basis for the application of the subsequent study.

Chapter 3 - The first sub-section of Chapter 3 begins with detailed information regarding the geology of the copper rich Semblana orebody as well as the Neves Corvo mine. It also provides information on a more regional scale by looking at the geology of the Iberian Pyrite Belt, South Portuguese Zone and the Iberian Massif. All geological aspects pertinent to exploration, such as structural geology, ore types, main lithologies and marker horizons are discussed from a geophysical perspective. This geological understanding plays a key role in defining the outlines and constraints for the application of the techniques and their subsequent analysis.

The second sub-section deals with the laboratory measurements carried out on the drill core samples from the Neves Corvo mine to create a database of the elastic properties of the major lithological units. Along with the standard cross-plots and graphs, it includes pseudo logs that are collated by drillhole, lithology and depth to grasp the seismic parameters of different lithologies as well as the different types of mineralization. Additionally, a basic modelling study was carried out in this chapter using FWS and pseudo logs in order to obtain the seismic response of different interfaces and to calibrate the seismic data. An additional zero offset modelling study

was also carried out on the logs to estimate the effect of geometry (thickness) and mineral content of the orebody, the interference effect and complexity of the seismic wave propagation and the wavelet itself on the seismic data. The results from these modelling studies are then taken into account to structure the subsequent data processing, inversion and data analysis.

Chapter 4 - A look at all the major stages of the seismic reflection survey that was conducted on the Neves Corvo mine in 2011 is carried out here. The first section begins with the acquisition and the initial conventional processing. The following section focuses on the preserved relative amplitude processing of the seismic sub-data set that encompasses the Semblana orebody. Here it explains key processing steps such as surface-consistent amplitude corrections, the application of a surface-consistent deconvolution, Radon (τ - p) filtering, interactive velocity analysis, surface-consistent residual reflection statics corrections and pre-stack Kirchhoff 3D time migration (PSTM). The success of PRA processing was further investigated in the final section of this chapter with a volumetric interpretation of the seismic data set utilizing mineralisation wireframes, interpreted geological surfaces and iso-shells.

Chapter 5 - The last technical chapter of this thesis consists of the model based acoustic and elastic inversion as well as the AVO analysis. The first section of this chapter consists of creating a database with FWS logs, pseudo logs and pre and post stack seismic data. A model based acoustic impedance inversion is then carried out including a calibration with drillhole logs with post-stack seismic data to be able to provide additional important information for rock type identification within the recovered impedance cube. Following this, AVO analysis was performed on the pre-stack seismic data to fine-tune the seismic response over the Semblana deposit. An elastic inversion was then utilized to aid in discriminating its response from the other non-economical lithologies.

In the final chapter of this thesis, the main conclusions are summarized and the findings that require further work are mentioned to steer future studies.

Chapter 2

Seismic for Minerals – Processing and Data Analysis

Preserved relative amplitude processing through the application of surface consistent principles is commonplace in soft rock seismic data processing. The main objective in soft rock seismic is to use amplitude information to infer the change of fluid in pore space. In hard rock seismic, PRA processing has different objectives depending on the mineralisation type. In the case of massive ore the PRA processing aims to preserve relative amplitude differences where an elevated amplitude response may indicate the presence of concentrated ore. In the case of copper systems, PRA processing is indeed aimed at enhancing the subtle amplitude differences that may be of interest for rock characterisation and targeting.

In this chapter, the relevant theoretical concepts behind PRA processing are presented. The well-established principals, assumptions and final mathematical equations used by the software algorithms that were chosen to carry out the major PRA processing steps are briefly summarized, with the major aim to extract and enhance primary signals. Finally, properly recovered preserved relative amplitudes enabled pre-stack amplitude studies, otherwise known as AVO studies.

It should be noted that the reciprocity and surface consistency principles are based on the concept of energy propagating as plane waves. While this far-field condition is

well obeyed for deep oil targets, in the case of mineral targets these conditions may not always be met. Instead of plane waves, spherical waves are encountered in the case of shallow mineral targets. Hence surface consistent approaches may not always provide fully preserved amplitudes and may therefore require modified procedures to be utilised. Because of this, PRA processing in hard rocks is not straightforward and its application to hard rock 3D seismic has not been frequently, if at all, noted.

Since these well-established theories for soft rocks are published in several papers and text books, the derivations of the mathematical equations will not be repeated here.

2.1 Surface-Consistent Amplitude Corrections

The variations of the amplitude of seismic energy depend on a large number of factors. The reflection coefficient, the interference of reflections and their attenuation are the primary interests of the reflection seismic method. The variations caused by spherical divergence, ray-path curvature, loss in transmission through intermediate reflectors, peg-leg multiples, reflector rugosity, and curvature are also associated with the subsurface factors that lithology or hydrocarbon accumulation information could be indirectly extracted (Sheriff 1975). Additionally, there are such variations that are not associated with any subsurface information, such as strength of the shot, the response and coupling of the receivers, the performance of the amplifier channel, the offset of the traces, geophone sensitivity, array directivity, instrument balance and scattering in the near-surface (Sheriff 1975).

Surface-consistent amplitude corrections were first introduced by Taner and Koehler (1981), which aimed to handle variations that are not associated with the subsurface. In this section, the theory behind surface-consistent amplitude corrections is explained.

Firstly, to sort the traces for the analysis a coordinate system was set up by Taner and Koehler (1981), called a surface diagram. As shown in Figure 2.1a, to simplify the analysis they used the distances along the line from the origin to the source (s) and to the receiver (r) as the two coordinates of the trace. The source and receiver positions along the seismic line is shown in Figure 2.1a, which corresponds to a point (s, r) on

the surface diagram Figure 2.1b and four principal trace organizations. These coordinates include common source traces, common receiver traces, common offset traces and common midpoint traces as shown in Figure 2.1c. The zero-offset line represents the moveout-corrected traces that are used as input to the common depth point (CDP) stacking.

The near-surface effects on the data are seen not only as time shifts or amplitude decays, but also as frequency dependent, time-varying filter effects that are present throughout the data. In order to handle these issues during the application of surface consistent corrections to a reasonable approximation, Taner and Koehler (1981) assumed the reciprocity of source and receiver positions (Knopoff and Gangi 1959) and that the near-surface effect is the same along the wave path (upward and downward) at a particular surface position. It was also assumed that the factors due to near-surface effects are time constant and surface consistent, as well as all traces at a particular CDP gather position have had essentially the same subsurface information and corrections for spherical divergence, normal move-out, and field statics applied.

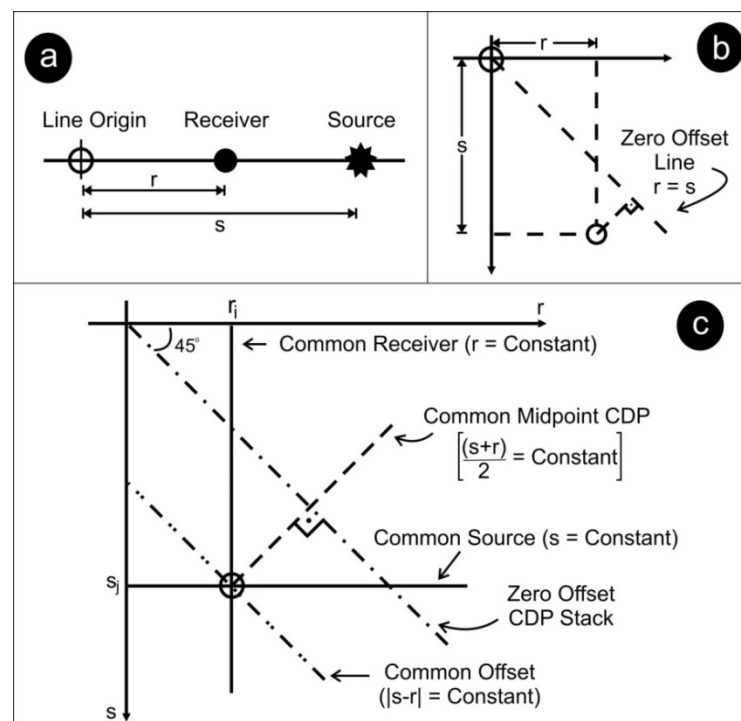


Figure 2.1 Source and receiver locations and principal trace organizations. (a) Source and receiver locations along the seismic line, (b) source and receiver locations on the surface diagram and c) principal trace organizations on the surface diagram (Adapted from Taner and Koehler (1981)).

Based on these assumptions, the surface consistent factors were simplified into the following four basic categories. They were also separated into their real (amplitude) and imaginary (phase or time shift) components for the corrections of near-surface anomalies. The equation for trace amplitude corrections was formulated as below;

$$f_{nm} = s_n + r_m + c_k + d_l \quad (2.1)$$

where,

f_{nm} = natural logarithm of root mean square (RMS) amplitude of trace with its source and receiver at surface positions n and m , respectively,

s_n = source performance factor at n^{th} surface position,

r_m = receiver performance factor at m^{th} surface position,

c_k = subsurface performance factor at k^{th} surface position, with $k = 1/2 (m + n)$

d_l = offset performance factor at offset $l = m - n$.

The performance factor is obtained from the natural logarithm of the average amplitude spectrum of the response function and the nontrivial solution for equation 2.1, which contain indeterminacies of a quadratic order for each trace but can be obtained by the least-mean error- squares technique.

The equation for phase corrections (time shifts) was formulated as below;

where,

$$\tilde{f}_{nm} = \tilde{s}_n + \tilde{r}_m + \tilde{c}_k + \tilde{d}_k (m - n)^2 \quad (2.2)$$

\tilde{f}_{nm} = total time shift of the trace with its source and receiver at surface positions n and m , respectively,

\tilde{s}_n = source time shift correction at surface position n ,

\tilde{r}_m = receiver time shift correction at surface position m ,

\tilde{c}_k = CDP gather time shift correction at surface position k ,

$\tilde{d}_k(m - n)^2$ = offset related time shift correction.

The offset related correction usually includes errors that originate from velocity field errors caused by near surface anomalies. The offset related corrections were modified to spatially varying residual normal move-out (as a function of k) in order to better approximate a parabola as a function of offset, which made the equation 2.2 identical to equation (2) of Taner *et al.* (1974) for near-surface time anomalies.

2.2 Surface-Consistent Deconvolution

Deconvolution can be described as the process of restoring the basic wavelet to its original form before it underwent convolution (a linear filtering action) (Sheriff and Geldart 1995). Deconvolution is utilized to remove unacceptable filtering effects of the original wavelet in order to improve the recognisability and resolution of reflected events. There are a few different types of deconvolution that are commonly applied to both pre and post-stack data. Deconvolution could be used in the removal of the filtering effects of the recording system (system deconvolution), the removal of filtering action of a surface water layer or other near-surface layers (Backus filter and gapped deconvolution), attenuation of multiples created by the surface or near-surface reflectors (predictive deconvolution), the removal of the effects of energy that leaves the source in an upward direction (deghosting), to equalize the amplitudes of all frequency components within a certain frequency band (whitening or equalizing), or in shaping the amplitude-frequency and/or phase response to match that of adjacent channels (Sheriff and Geldart 1995). Different phase assumptions, gate locations or widths, or operator lengths are the most important parameters in the application of a deconvolution.

Surface-consistent deconvolution is a type of deconvolution that was first introduced by Taner and Coburn (1981), which considers near-surface effects in order to apply necessary filters in land seismic. Surface-consistent deconvolution (spectral decomposition) decomposes convolutional effects related to the source, receiver, offset and the earth's impulse response in order to restore the wavelet that is affected by near-source and near-receiver conditions and source-receiver separation. The Earth's impulse response is then recovered by inverse filtering (Yilmaz 2001). The surface-consistency of the spectral decomposition is formulated with the assumption

that the basic wavelet shape depends only on the source and receiver locations and the near-surface effect is the same throughout the wave path (Yilmaz 2001). The convolutional model to estimate the earth's impulse response can be described as below;

$$x(t) = w(t) * e(t) + n(t) \quad (2.3)$$

where,

$x(t)$ is the recorded seismogram,

$w(t)$ is the source waveform,

$e(t)$ is the earth's impulse response,

$n(t)$ is the noise component.

A postulated surface-consistent convolutional model is given by Yilmaz (2001);

$$x'_{ij}(t) = s_j(t) * h_l(t) * e_k(t) * g_i(t) + n(t) \quad (2.4)$$

where,

$x'_{ij}(t)$ is a model of the recorded seismogram,

$s_j(t)$ is the waveform component associated with source location j ,

$h_l(t)$ is the component associated with offset dependency of the waveform defined for each offset index $l = i - j$,

$e_k(t)$ is the earth's impulse response at the source-receiver midpoint location, $k = (i + j)/2$,

$g_i(t)$ is the component associated with receiver location i

$n(t)$ is the noise component.

After modifications due to the consideration of the amplitude spectrum, the four components could be decomposed by solving equation 2.3 with the application of a

least-squares minimization to the following set of equations (Cary and Lorentz 1993; Yilmaz 2001),

$$\tilde{S}_j^m = \frac{1}{n_r} \sum_i^{n_r} \{\tilde{X}_{ij}\} - \frac{1}{n_r} \sum_i^{n_r} \{\tilde{H}_i^{m-1} - \tilde{E}_k^{m-1} - \tilde{G}_i^{m-1}\}, \quad (2.5a)$$

$$\tilde{G}_i^m = \frac{1}{n_s} \sum_j^{n_s} \{\tilde{X}_{ij}\} - \frac{1}{n_s} \sum_j^{n_s} \{\tilde{H}_i^{m-1} - \tilde{E}_k^{m-1} - \tilde{S}_j^{m-1}\}, \quad (2.5b)$$

$$\tilde{H}_l^m = \frac{1}{n_e} \sum_k^{n_e} \{\tilde{X}_{ij}\} - \frac{1}{n_e} \sum_k^{n_e} \{\tilde{S}_j^{m-1} - \tilde{E}_k^{m-1} - \tilde{G}_i^{m-1}\}, \quad (2.5c)$$

$$\tilde{E}_k^m = \frac{1}{n_h} \sum_l^{n_h} \{\tilde{X}_{ij}\} - \frac{1}{n_h} \sum_l^{n_h} \{\tilde{S}_j^{m-1} - \tilde{H}_l^{m-1} - \tilde{G}_i^{m-1}\}, \quad (2.5d)$$

where,

$\sum X_{ij}$ is input data and m is the iteration index,

\tilde{S}_j , \tilde{G}_i , \tilde{H}_l , and \tilde{E}_k , are the spectral components associated with the source and receiver locations, offset dependency, and earth's impulse response.

The Gauss–Seidel method is an iterative method that is commonly used to solve this linear system of equations in order to decompose the input into surface-consistent components. In practice, the application of a surface-consistent deconvolution on field data is usually performed for only the source and receiver terms (Yilmaz 2001).

2.3 Surface-Consistent Residual Static Corrections

Static corrections are time shifts that are applied to the seismic data to compensate for the effects of variations in topography and the near surface weathered layer. The calculation of residual static corrections can be approximated as surface-consistent static time shifts designed to handle variations in elevation, the base and the velocity of the weathered layer as well as to aid in imaging deeper reflections that can also be affected by deep and complex geological structures. The constant time shifts associated with deeper reflectors can be done by taking the surface locations of shots

and receivers down to a datum below the weathered layer in a surface-consistent manner (Hileman *et al.* 1968; Taner *et al.* 1974).

As explained in Taner *et al.* (1974), trace-to-trace variations of the reflection arrival times depend on both static and dynamic effects. Similar to explaining surface-consistent amplitude corrections, surface diagrams can simplify the analysis to be performed for the separation of these effects (Figure 2.2).

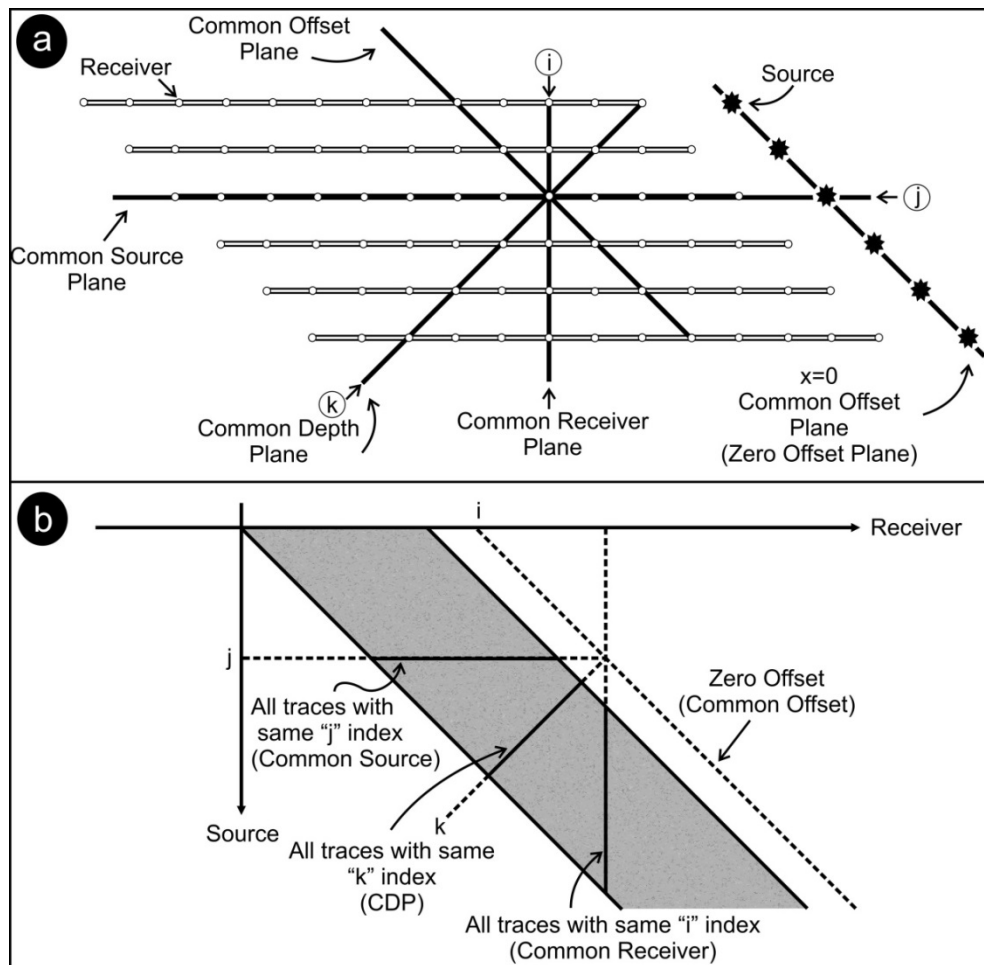


Figure 2.2 Surface diagrams. (a) Source and receiver position diagram showing four principal trace planes. (b) Surface diagram showing the trace coordinate relationship. i is the index for the traces that belong to a common receiver plane, j is the index for the traces that belong to a common source plane and k is the index for the traces that belong to a common depth plane (Adapted from Taner *et al.* (1974)).

The residual time shifts (T_{ijk}) for an individual trace with surface coordinates i and j can be computed with a surface-consistent assumption and by considering the surface diagram (Figure 2.2) to produce equation 2.5 (Taner *et al.* 1974; Wiggins *et al.* 1976);

$$T_{ijk} = R_i + S_j + C_k + M_k(j - i)^2 \quad (2.5)$$

where,

R_i = source receiver static at i^{th} receiver position,

S_j = performance factor at j^{th} surface position,

C_k = arbitrary time shift at k^{th} CDP gather,

M_k = offset performance factor at offset

$(j - i)$ = source-to-receiver distance

$k = 1/2 (i + j)$

These equations could be separated by the least-mean square error technique and then the final sets of equations may be solved either by an iterative process or by normal matrix operations.

The time variant estimation of static shifts on normal move-out (NMO) corrected gathers for land seismic data is prone to errors due to low fold and poor signal-to-noise ratio, which may consequently result in an erratic and unstable residual static solution (Yilmaz 2001). The minimization of the difference between modelled and actual travel time deviations associated with a reflective event on move out corrected gathers could provide more robust surface-consistent residual static estimates. Therefore, the utilization of stacked traces is common (Ronen and Claerbout 1985). A super-trace can be built by stacking all of the traces of any selected domain (i.e., shot domain) in sequence. The basis of the method of stack power maximization involves creating two super-traces from the common-shot or common-receiver gather traces before and after stacking as in Figure 2.3. The stack power $P(\Delta t)$ was formulated by Ronen and Claerbout (1985) as below, where the first two terms are the powers of the two super-traces that can be defined by a constant, and the third term is the cross-correlation of the two super-traces. Therefore, maximizing the stack power is equivalent to maximizing the cross-correlation and it is calculated for each shot gather in order to estimate the best residual static corrections.

$$P(\Delta t) = \sum_t F^2(t - \Delta t) + \sum_t G^2(t) + 2 \sum_t F(t - \Delta t)G(t) \quad (2.6)$$

where Δt is the trial static shift, $F(t)$ is the shot or the receiver super-trace and $G(t)$ is the stack super-trace.

Residual statics are of prime importance in the application of seismic for mineral exploration. The bulk of the time delays related to the presence of the regolith zone is accounted for by the application of refraction statics. The remaining (residual) statics are often observed as 4-8 ms shifts, which are sufficient to destroy high-resolution images or to drastically reduce the frequency content. In either case residual statics has the ability to restore the coherency and the resolution of seismic data. In this study particular attention was devoted to the application of residual statics for this reason.

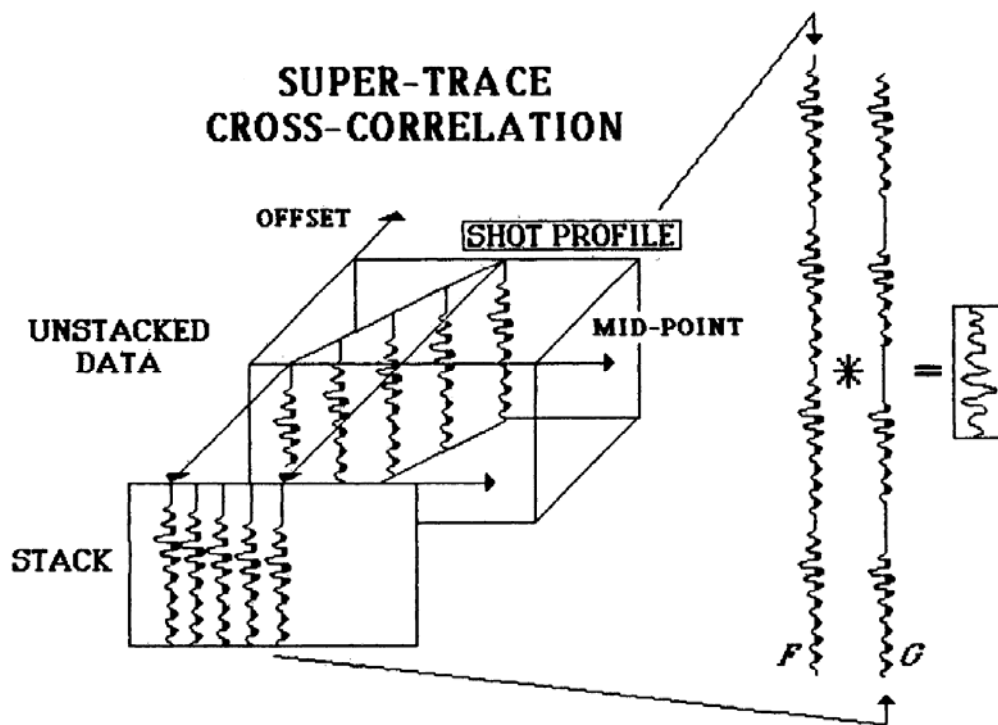


Figure 2.3 Super trace cross-correlation for the stack power maximization method. The plane containing the shot profile in the unstacked data volume is moved up or down according to the static shift of the shot. The CDP stack is changed as a function of that static shift. Maximizing the power of the CDP stack as a function of that particular shot static is equivalent to maximizing the cross-correlation between two super traces built from the shot profile (trace F) and the relevant part of the CDP stack (trace G). The procedure is then repeated for every shot and geophone (After Ronen and Claerbout 1985).

2.4 Linear Radon Transform

The linear Radon transform (slant-stack) is a common processing routine to transform the data into the Tau-P (τ - p) domain (intercept time – ray parameter) in order to separate the signal from coherent noise and allow it to be more easily filtered or muted. A linear Radon transform decomposes the data into a series of straight lines to map points and hyperbolic events to map elliptical curves. An inverse routine is then used to reverse the transform. Since it can provide amplitude consistent results, it is commonly used in multiple suppression and it may also be used to optimally attenuate the ground roll, guided waves, refractions and other types of interference.

Yilmaz (2001) defines the Radon transform as a relationship between the input coordinates (h, t) and the transform coordinates (p, τ) as given by the linear move-out equation;

$$t = \tau + 2ph \quad (2.7)$$

where p is the ray parameter, t is the two-way travelttime, τ is the two-way intercept time at $p = 0$, and h is the half offset, then an event with linear moveout in the time-offset domain can be mapped to a point within the slant-stack domain (Figure 2.4) using the summation below;

$$s(p, \tau) = \sum_h d(h, t = \tau + 2ph) \quad (2.8)$$

where $d(h, t)$ represents the common mid-point (CMP) gather, and the output $s(p, \tau)$ represents a plane wave.

If the relationship between the input coordinates (h, t) and the transform coordinates (v, τ) is integrated into the hyperbolic move-out equation;

$$t^2 = \tau^2 + \frac{4h^2}{v^2} \quad (2.9)$$

where t is the two-way travelttime, τ is the two-way zero offset time, and h is the half offset and v is the stacking velocity, then an event with hyperbolic move-out, such as

a primary or a multiple event, in the time-offset domain can be mapped to an ellipse in the τ - p domain (Figure 2.4) using the summation below;

$$u(v, \tau) = \sum_h d\left(h, t = \sqrt{\tau^2 + 4h^2/v^2}, \right) \quad (2.10)$$

where $d(h, t)$ represents the CMP gather, and the output $u(v, \tau)$ represents the velocity-stack gather.

This technique can drastically improve signal-to-noise ratio. However, in the case of hard rock seismic its application is not straightforward as it may result in attenuation or elimination of steeply dipping primary reflections.

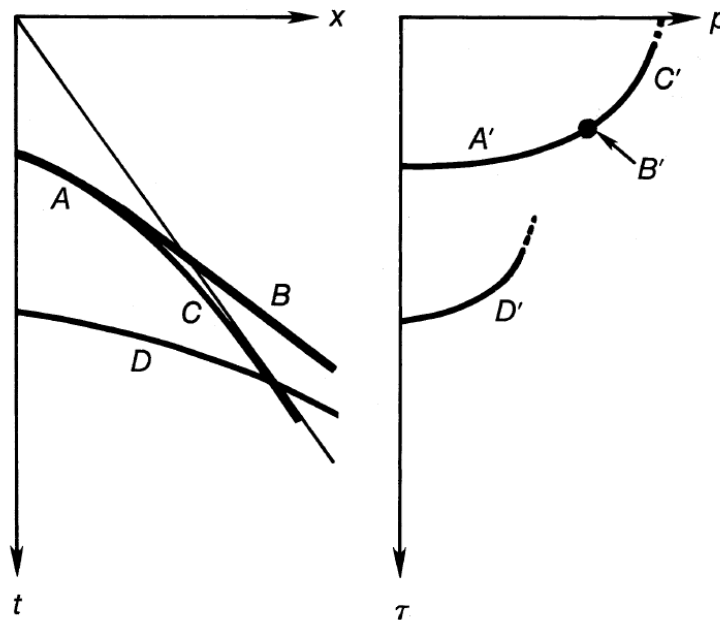


Figure 2.4 The map of several arrivals on both the CMP gather and the corresponding τ - p gather. The events A , B , C and D on the CMP gather (left) are mapped onto A' , B' , C' and D' in the τ - p gather (right) (After Yilmaz 2001).

2.5 Kirchhoff Migration

Seismic migration is one the most important of all seismic data processing steps that significantly improves the spatial resolution by back-propagating the seismic wavefield from the position where it was detected to its true subsurface position as well as collapsing diffractions. Over the last 40 years, there have been various methods developed to perform different types of migration (Bancroft 1998; Yilmaz

2001). These include, but are not limited to, the Gazdag or Phase shift migration, Finite Difference migration, Steep Dip Explicit migration, FX (Explicit) Migration and FK migration (Stolt migration). The Kirchhoff migration is one of the most robust migration techniques, which is performed by integrating along diffraction curves using the Kirchhoff equation and positioning the the results at the apexes of the diffraction curves (Sheriff and Geldart 1995). This technique is of particular importance to hard rock seismic data processing as it can handle irregular geometries and steep (vertical) dips. If low frequencies are preserved, this technique is capable of imaging vertical structures in hard rock seismic environments (Urosevic *et al.* 2007).

The migration method was initially based on the characterization of point sources in the subsurface with two practical migration schemes. The first scheme is defined by a zero-offset section consisting of a single arrival at a single trace recorded in a constant velocity medium that migrates to a semicircle. This migration method is based on the superposition of semicircles, where the final migrated section is called migrated impulse response (Yilmaz 2001). The second scheme is defined by a zero-offset section consisting of a single diffraction hyperbola migrated to a single point. The second migration method is based on the summation of amplitudes along hyperbolic paths and is known the diffraction summation method, diffraction stack or more generally a Kirchhoff migration (Yilmaz 2001). The velocity of the medium has control on the curvature of the hyperbolic trajectory for the amplitude summation. An RMS velocity function at the apex of the hyperbola at time τ is used to compute the travel-time trajectory for a horizontally layered velocity-depth model as below;

$$t^2 = \tau^2 + \frac{x^2}{v_{rms}^2} \quad (2.11)$$

Yilmaz (2001) states a diffraction summation using assumptions for obliquity, spherical spreading and wavelet shaping factors is called a Kirchhoff summation. The migration method based on this summation is called the Kirchhoff migration. The integral solution to the scalar wave equation that defines the mathematical treatment of the Kirchhoff migration method is reported in Schneider (1978).

The integral solution of the scalar wave equation consists of the far-field term and two other terms. The far-field term mostly contributes to the summation and is used in the practical application of the Kirchhoff migration. The output image P_{out} at a subsurface location (x_0, z) using only the far-field term is computed from the 2D zero-offset wavefield P_{in} , which is measured at the surface ($z = 0$) by the following summation over a spatial aperture;

$$P_{out} = \frac{\Delta x}{2\pi} \sum \left[\frac{\cos\theta}{\sqrt{v_{rms}r}} \rho(t) * P_{in} \right] \quad (2.12)$$

where v_{rms} is the RMS velocity at the output point (x_0, z) and r is the distance between the input and the output points. The rho filter $\rho(t)$ convolution is represented with the asterisk in equation 2.12 and is the derivative of the measured wavefield with the input wavefield P_{in} . The summation in equation 2.12 is carried out at $t = 0$ for each output location to obtain the final migrated section. The range of the summation is called the migration aperture (Yilmaz 2001).

As reported in Bancroft *et al.* (1998), if a subsurface model is comprised of scatter points that scatter energy from a source to all receivers and a coherent reflection is caused by an organized arrangement of scatter points, pre-stack migration is capable of collecting all of the scattered energy and migrating it to the true spatial position of the scatter points. Pre-stack Kirchhoff migration assumes an output location (or scatter point) and performs the summation for the appropriate energy from all available input traces for every output sample. One of the advantages of the pre-stack Kirchhoff migration is that the selected CMP gathers can be output in their migrated positions, which allows certain flexibility for velocity picking. It also accommodates irregular topography (Bancroft 1998) and is sensitive to lateral velocity changes. However, if the seismic velocities are quite high as in hard roc seismic imaging, without a need for dip move-out (DMO) it can provide drastically better solutions than post-stack time migration (Yilmaz 2001).

2.6 AVO Analysis and Elastic Impedance Inversion

In seismic processing, it is assumed that seismic waves propagate through rock layers, each of which have different elastic moduli, and that the energy of the seismic

waves both reflects and is partitioned at each boundary. While some of the incident energy related to the compressional source is mode-converted to a shear wave (depending upon the angle of incidence), both the compressional- and shear-wave energy are partly reflected from and partly transmitted through each of the layers according to Snell's law. The reflection amplitudes can be analysed as a function of offset/angle to identify lateral changes in the elastic properties of the rocks, such as a change in P-wave velocity, S-wave velocity and density, thereby allowing the calculation of Poisson's ratio (Yilmaz 2001).

The amplitude variation with offset can be analysed by plotting the peak amplitudes against offset for a target horizon at each CMP gather. An AVO curve is then fitted on this variation, which can be used to obtain reservoir parameters. This curve shows a pattern depending on the rock and fluid properties and the detection of this pattern depends on the signal-to-noise ratio and the range of the incidence angle. The dip of the reflecting boundary and its curvature affect the reflection amplitudes, but this affect can be eliminated with pre-stack time migration (Yilmaz 2001).

Zoeppritz equations (Zoeppritz 1919) are used in the modelling of the reflection amplitude variations with angle of incidence and therefore with offset. These were derived based on a two layered earth model separated by a horizontal interface. The derivation of Zoeppritz equations starts with the derivation of the equations of motion and Hooke's law, which were the basis for the wave equation for elastic waves in isotropic media. Since then, the equations for continuity, plane-wave solutions to the wave equation and Snell's law were derived and used to obtain the Zoeppritz equations (Yilmaz 2001).

Due to the complexity of the Zoeppritz equations, the first approximation was given by Aki and Richards (1980) to drive the P-to-P reflection amplitude. In order to get a more practical application, Shuey (1985) then modified the Aki-Richards equation as below;

$$R(\theta) = \left[\frac{1}{2} \left(\frac{\Delta V_P}{V_P} + \frac{\Delta \rho}{\rho} \right) \right] + \left[\frac{1}{2} \frac{\Delta V_P}{V_P} - 4 \frac{V_S^2}{V_P^2} \frac{\Delta V_S}{V_S} - 2 \frac{V_S^2}{V_P^2} \frac{\Delta \rho}{\rho} \right] \sin^2 \theta \quad (2.13)$$

$$+ \left[\frac{1}{2} \frac{\Delta V_P}{V_P} \right] (\tan^2 \theta - \sin^2 \theta)$$

where $R(\theta)$ is the angle-dependent reflection amplitude, θ is angle of incidence, V_P is the compressional-wave (P-wave) velocity, V_S is shear-wave (S-wave) velocity and ρ is density.

As reported in Wiggins *et al.* (1984), the first-order approximation to the Zoeppritz equation was rearranged in order to obtain more practical AVO attributes as below;

$$R(\theta) = A + B\sin^2\theta + C(\tan^2\theta - \sin^2\theta) \quad (2.14)$$

where A is the first term and is called the intercept, which is a linearized version of the zero offset reflection coefficient, and B is the second term or otherwise known as the gradient. While the intercept (A) is a function of only density and P-wave velocity, the gradient (B) is dependent on changes in P-wave velocity, S-wave velocity, and density, therefore it has the most considerable effect on amplitude changes as a function of offset. C is the third term and is called the curvature, which is controlled by P-wave velocity only. The solution of the third term may lead to the full seismic characterization of the prospect zone, however this term may be dropped at intermediate angles ($0 < \theta < 30$ degrees).

AVO attributes can be used to estimate P-wave velocity, S-wave velocity and in ideal conditions (very high signal to noise ratio, very long offsets) the density of the zone of interest in order to provide information about fluid and/or lithology. One of the techniques to obtain an estimation of these seismic parameters is range-limited stacking. The range-limited stacking method utilizes constant offsets or constant angle stacks and is known to be a very robust method due to efficient noise suppression during the process of stacking. However it was further improved to an elastic impedance inversion by Connolly (1999). Connolly (1999) proposed that, similar to acoustic impedance (AI), elastic impedance (EI) can be defined as below;

$$R(\theta) \approx \frac{1}{2} \frac{\Delta EI}{EI} \approx \frac{1}{2} \ln(EI) \quad (2.15)$$

The derivation of equation 2.15 by considering only the first two terms of equation 2.14 in order to have a straight line fit for higher angles (larger offsets) provides the mathematical definition of elastic impedance as;

$$EI(\theta) = V_P^{(1+\sin^2\theta)} V_S^{(-8K\sin^2\theta)} \rho^{(1-4K\sin^2\theta)} \quad (2.16)$$

where, $K = \left(\frac{V_S}{V_P}\right)^2$, $EI(\theta)$ is the angle-dependent elastic impedance, θ is angle of incidence, V_P is compressional-wave (P-wave) velocity, V_S is shear-wave (S-wave) velocity and ρ is density.

It can be deduced from equation 2.16 that for zero offset data ($\theta = 0^\circ$) the elastic impedance is equal to acoustic impedance and can be formulated as below;

$$EI(0^\circ) = AI = V_P \rho \quad (2.17)$$

In this chapter the fundamental steps required for PRA processing, which is considered a prerequisite for the subsequent acoustic impedance inversion, AVO analysis and elastic impedance inversion, are explained. However, the conventional physical and mathematical derivation for sedimentary geology is not directly relevant to hard rock seismic data processing and analysis. Issues such as the amplitude loss mechanisms in hard and soft rock are not identical. Additionally, in hard rock geology there is a general lack of porosity and fluids in the pore space, which govern the P-wave propagation in soft rocks. Hence, in hard rocks the V_p/V_s ratio, or Poisson's ratio, tends to be a monotonic function (Urosevic *et al.* 2007, personal communication). Consequently, amplitude variations (AVO anomalies) in hard rock geology are very subtle and are not related to the fluid type or change of the fluid type in the pore space. It is more common for AVO anomalies to be associated with the mineral composition change, textural variations and structural deformation. Hence, in the case of VMS deposits with high iron content, the application of AVO analyses may be used to infer the rock composition and help in direct mineral targeting. In particular, the relationship between acoustic and elastic impedance may be indicative of the presence of massive ore, especially in the case of high pyrite content where the P-wave velocity tends to reach a maximum value of well over 7000 m/s.

The significance of this observation for mineral exploration could potentially lead to a step change in how seismic data is viewed and implemented by the mining industry.

Chapter 3

Geological Setting and Rock Physics

It was considered crucial to possess an in-depth understanding of all the major geological aspects related to the Semblana orebody as well as the greater Iberian Pyrite Belt in order to maximise the effectiveness of the seismic processing and the subsequent analysis. The first section of this chapter summarizes the geology of the copper rich Semblana orebody. This includes an insight into the structural geology, ore types, main lithologies and marker horizons from a geophysical perspective. This insight is also vital to establishing a solid link between the geology and the seismic volume using all feasible techniques to improve the accuracy of the imaging.

The following section focusses on the laboratory measurements carried out on the core samples obtained from the Neves Corvo mine in order to create a database of the elastic properties of the major lithological units. The results were then utilized in the final section to create pseudo logs to correlate along with recorded FWS and seismic data. This would facilitate the calibration of different geologic interfaces with reflectors identified within the seismic data.

This chapter includes excerpts from the paper “Yavuz S., Kinkela J., Dzunic A., Penney M., Araujo V., Neto R., Ziramov S., Pevzner R. and Urosevic M., 2015. Physical Property Analysis and Preserved Relative Amplitude Processed Seismic

Imaging of Volcanogenic Massive Sulfides – A Case Study from Neves Corvo, Portugal. *Geophysical Prospecting - Hard Rock Seismic Imaging Special Issue 63 (4)*, 798-812.” that was published by the EAGE in July 2015 (Copyright 2015 by the European Association of Geoscientists & Engineers). This reference is no longer cited in the following.

3.1 Geological Setting

In this section we cover the geological setting of the Iberian Pyrite Belt, Neves Corvo mine and the Semblana orebody. The structural geology of the Neves Corvo area is also reviewed in order to create a well-defined geological framework within which to review the seismic data.

The Iberian Pyrite Belt, with its numerous giant and super-giant mines, is considered one of the most important VMS regions of not only Europe but the rest of the world. The super-giant Neves Corvo mine is located on the Portugal side of the Iberian Pyrite Belt. Since 1989, five massive sulfide lenses have been actively mined at Neves Corvo. These are comprised of the Neves, Corvo, Graça, Zambujal and Lombador lenses with a metal zoning consisting of copper, tin and zinc as well as barren massive pyrite. In 2010, a new copper rich orebody referred to as Semblana was discovered at the Neves Corvo VMS camp. The recent discovery of the Monte Branco orebody demonstrates that Neves Corvo continues to reside in an under-explored region of the Portugal side of the South Portuguese Zone (Barriga *et al.* 1997; Rosa *et al.* 2012; Lundin Mining Corporation 2013).

The complex structural geology of the Neves Corvo area is associated with felsic submarine volcanism, which is similar to the Iberian Pyrite belt's other mines, with the same repeating lithostratigraphic sequences such as Phyllite-Quartzite group, volcanic sedimentary complex and Flysch. The Neves Corvo thrust is a key structural feature, which provides a strong control on the geology in this region. The mineral deposits can occur as high-grade copper and/or zinc mineralisation within massive sulfide pyritic lenses with a typically underlying feeder zone of so called stockworks. Figure 3.1 shows a geological map of the Iberian Pyrite Belt over the South Portuguese Zone with selected massive sulfide deposits, the main geological units and major faults and thrusts displayed.

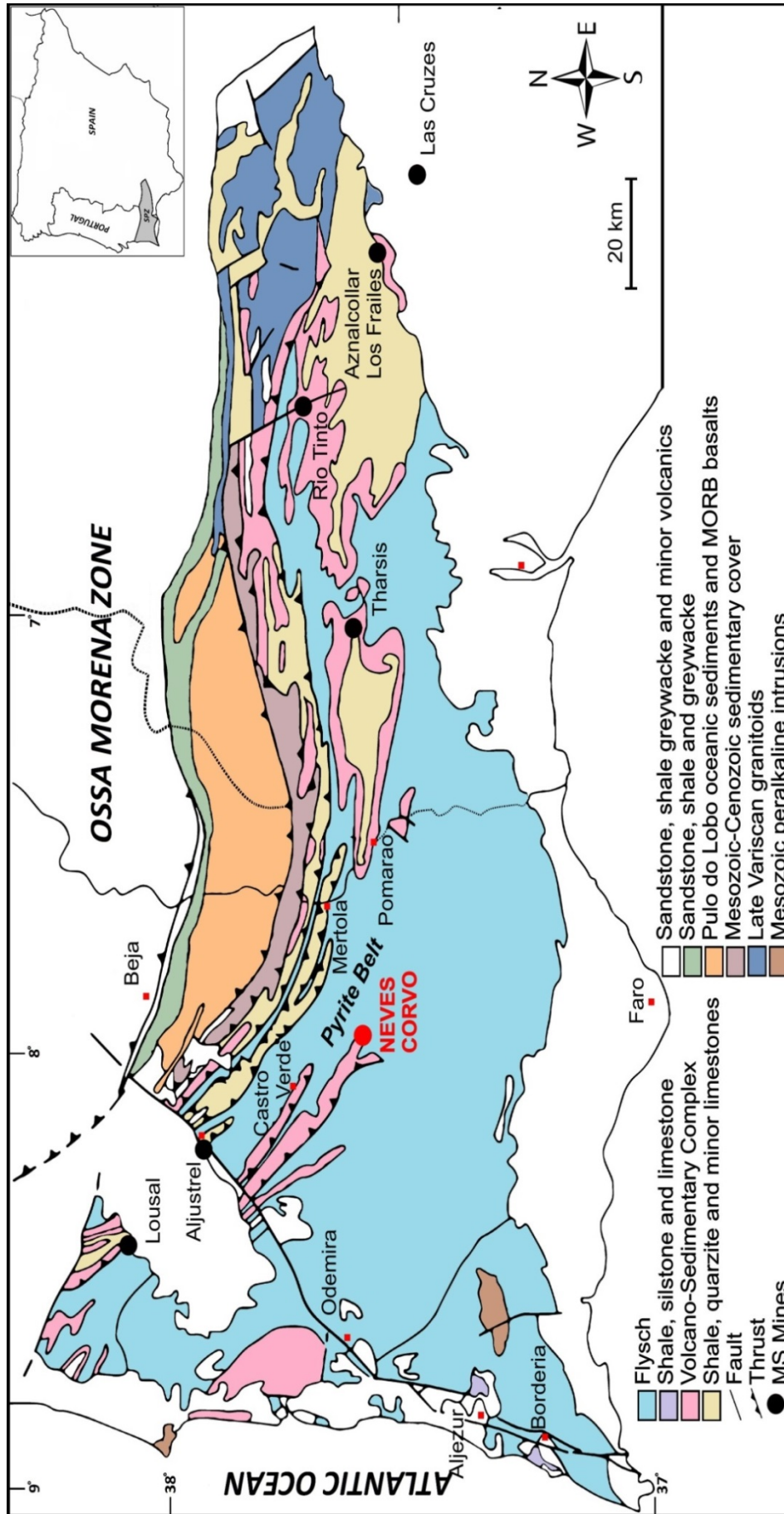


Figure 3.1 Geological map of the Iberian Pyrite Belt over the South Portuguese Zone with selected massive sulfide deposits and the main geological units displayed. (Adapted from Barriga *et al.* (1997), Leistel *et al.* (1997) and Oliveira *et al.* (2004).)

3.1.1 Iberian Pyrite Belt

The Devonian/Carboniferous Iberian Pyrite Belt located in the SW corner of the Iberian Peninsula is one of the oldest mining districts as well as one of the biggest VMS metallogenic provinces in the world. The 280 km long and 30-40 km wide Iberian Pyrite Belt partly overlays on the regions of Baixo Alentejo in Portugal and Huelva and Sevilla in Spain. It was formed during the Variscan Orogeny and covers most of the South Portuguese Zone (Barriga *et al.* 1997; Carvalho *et al.* 1999; Soriano and Casas 2002), which is immediately to the south of the Ossa-Morena zone and separated by the Ferreira-Ficalho Major Thrust (Figure 3.1).

There are numerous important time and strata-bound cupreous pyrite orebodies that occur within the Iberian Pyrite Belt together with various small manganese deposits. All VMS deposits of the Iberian Pyrite Belt are associated with felsic submarine volcanism (Gaspar and Pinto 1991). As reported by Strauss and Madel (1974), more than 60 pyrite mines of the Iberian Pyrite Belt produced around 280 million tons of cupreous pyrites for 100 years. The Iberian Pyrite Belt's stratiform pyrite deposits total reserves estimation is 1000 million tons with 500 million tons proven reserves and the remaining inferred reserves plus eroded deposits (Strauss and Madel 1974). Some of the mines of the Iberian Pyrite Belt include several giant and super giant deposits such as Rio Tinto, Las Cruces, Tharsis, La Zarza, Sotiel, Aznalcóllar and Los Frailes in Spain and Sao Domingo, Aljustrel, Lousal and Neves Corvo in Portugal (Barriga *et al.* 1997; Leistel *et al.* 1997; Sáez *et al.* 1996). Sulfide, copper, iron, zinc, lead and manganese ores have been predominantly mined over the last century (Sáez *et al.* 1999).

Some of the mines within the Iberian Pyrite Belt include several giant and super giant deposits such as Rio Tinto, Tharsis, La Zarza, Perrunal, Sotiel and Aznalcóllar in Spain and Sao Domingo, Aljustrel, Lousal and Neves Corvo in Portugal (Barriga *et al.* 1997; Leistel *et al.* 1997; Sáez *et al.* 1996). Sulfide, copper, iron, zinc, lead and manganese ores have been the predominantly mined minerals for the last century from among all the Iberian Pyrite Belt's mines (Sáez *et al.* 1999).

3.1.2 Neves Corvo Mine

The Neves Corvo mine covers an area of 13.5 km² and is located in the Alentejo province of southern Portugal, which is situated approximately 220 km southeast of Lisbon and 15 km southeast of Castro Verde. Since the commencement of mining in 1989, it has been considered as one of the largest and richest VMS mines in the world. It has produced more than 300 Mt of sulfides including 100 Mt of copper and zinc ores at 3.46% and 3.54% respectively, 50 Mt of zinc ore at ~6% and 300,000 tons of tin metal (mainly cassiterite and stannite) (Rosa *et al.* 2008). These quantities make it bigger than a medium-sized porphyry copper mine with a much higher grade (O'Brien and West 2013).

The Neves Corvo mine is comprised of six different orebodies including the Neves, Corvo, Graça, Zambujal, Lombador and Semblana recently discovered (Figure 3.2). Like all the other Iberian Pyrite Belt mines it is associated with submarine volcanism and three unique lithostratigraphic sequences. These are the Phyllite-Quartzite group, volcanic sedimentary complex and Flysch. The Neves Corvo orebodies are found at a depth of between 230 to 1300 m and on both sides of the Roário-Neves Corvo anticline. Another common geological feature in Neves Corvo are the bridges of thin massive sulfide mineralization in between the massive sulfide lenses. These bridges are conformable with the stratigraphy linking the lenses over the crest of the fold. All the deposits are located under the massive sulfide lenses and in between discontinuous black shale units and felsic volcanic rocks, which occur close to the top of the volcanogenic sedimentary complex (Gaspar 2002).

Stockworks are structurally controlled and randomly oriented vein type ore deposits that typically underlie very large, regular, continuous and predictable massive sulfide pyritic lenses. The mineralisation in Neves Corvo mimics these structures at depth in terms of their geologic complexity (Neil 2008). Stockworks are spotted within both footwall and hanging wall rocks and can be laterally disrupted by abrupt barren pyrite. It consists of very high grade copper, zinc and tin, similar to the other deposits of the Iberian Pyrite Belt.

3.1.3 Semblana Ore Body

The Neves and Corvo orebodies of the Neves Corvo mine were discovered in 1977. Over the next 11 years three more orebodies were added to the mine, namely the Graça, Zambujal and Lombador orebodies. However, the discovery of the sixth orebody took almost 22 years of continuous exploration work. The newly discovered copper rich orebody was subsequently named Semblana and was discovered only 1.3 km northeast of the Zambujal copper-zinc orebody in 2010. The Semblana orebody relative to the Neves Corvo mine is illustrated in Figure 3.2. Almost sub-horizontal in nature, the Semblana orebody consists of a gentle dip of 15° to 20° to the north and exists at 820 – 1170 m depth with up to 100 m thickness containing massive sulfide, massive copper and copper stockworks. As of September 2013, Lundin Mining Corporation had announced an inferred resource estimate for the Semblana deposit of 7.8 million tons grading at 2.9% copper +26 g/t silver.

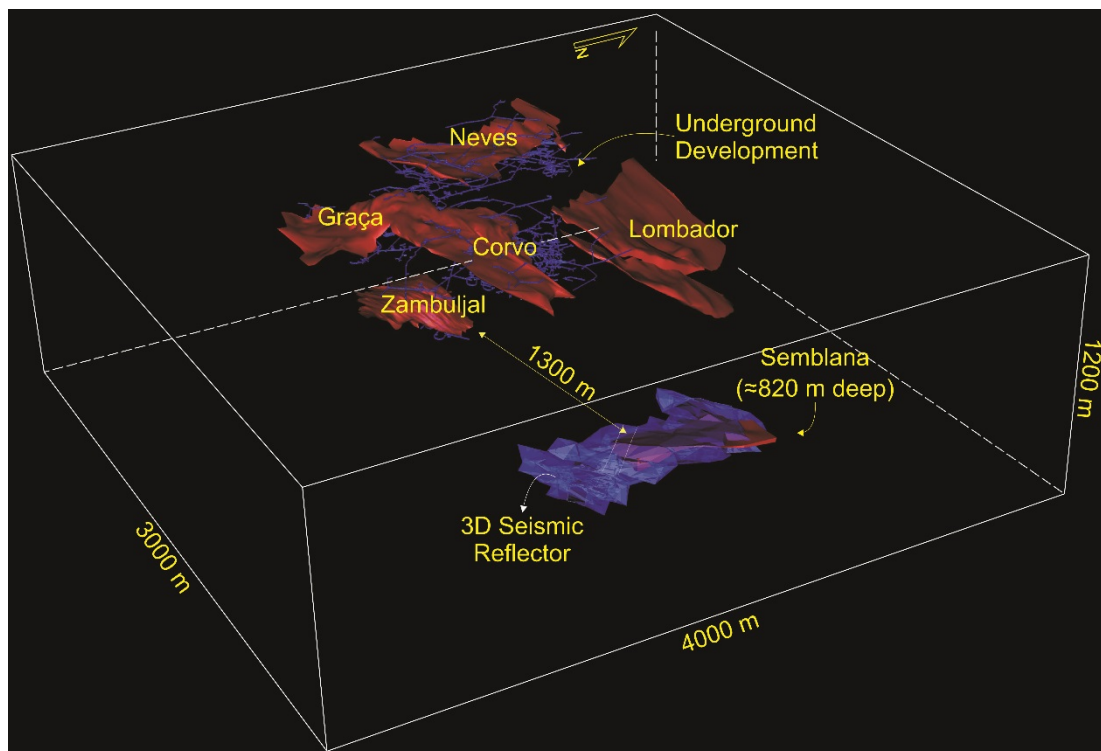


Figure 3.2 3D View of the Neves Corvo mine with massive sulfide lenses in red and main infrastructure in blue. (Courtesy of Lundin Mining Corporation). The Neves orebody sits at a depth of 700 m while the Corvo orebody lies between 230-800 m.

The Semblana orebody has similar VMS characteristics to the other orebodies of Neves Corvo and the Iberian Pyrite Belt. The massive sulfide lens of Semblana overlies a high grade massive copper lens with a copper bearing stockwork zone

underneath. Rhyolites, with occasional non-economic mineralization, exhibit a strong control over the stratigraphy of the footwall of Semblana, with varying widths from a few metres to tens of metres. In the northern part of the Semblana orebody tin concentrations are identified in the stockwork as well as the massive ores. Despite the presence of massive and stockwork copper there was no fissural zinc identified. However, pods of zinc mineralisation were found to the south. Due to existing drillhole lithology logs and seismic data as well as its high pyritic content the Semblana orebody presented a promising seismic target for this study (Figure 3.3). As an end member, the Semblana orebody has very high velocity and high density. However, due to its complex internal structure, the subsequent interpretation justified the challenges that conventional seismic processing experienced.

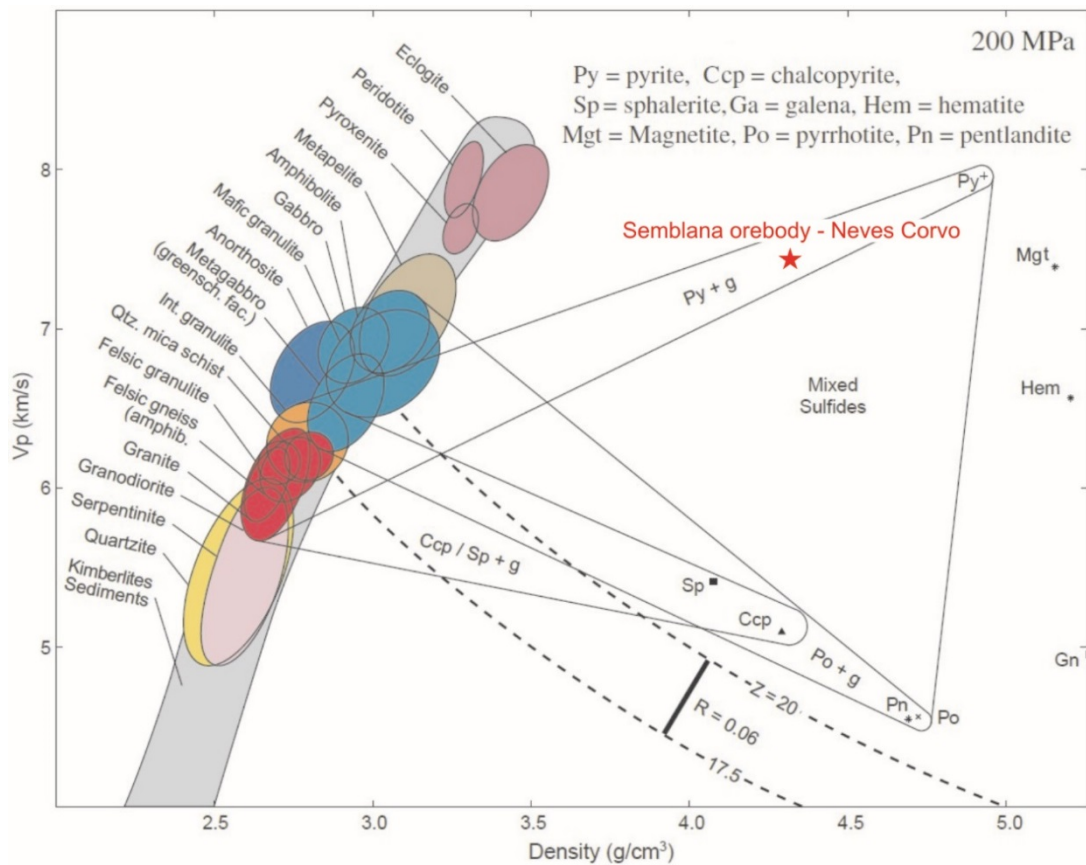


Figure 3.3 Acoustic properties of the most common crystalline rocks and ore mixtures (modified after Salisbury and Snyder 2007). P-wave velocity and density fields are displayed for common rocks on a Nafe-Drake curve (grey) with constant acoustic impedance iso-contours at a standard confining pressure of 200 MPa. Galena (Gn, off scale) has a velocity of 3700 m/s and a density of 7.5 g/cc. The Semblana orebody with its high pyrite content takes its place on a significantly high density and velocity zone. The acoustic impedance contrast of the Semblana orebody to host rocks, which fall into the Nafe-Drake curve, shows the high potential for direct seismic imaging.

3.1.4 Lithology

Based on the contributions of Schermerhorn and Stanton (1969), Oliviera and Quesada 1998 and Carvalho *et al.* 1999 the Iberian Pyrite Belt's lithostratigraphic sequence consists of three major units: the Phyllite-Quartzite group, volcanic sedimentary complex and Flysch group (CULM). All these units were tectonically shaped by the Variscan deformation. This was associated with syn-orogenic NW-SE trending and SW-NE verging folds with accompanying thrusting and cleavage and late orogenic NE-SW trending faults (Oliveira *et al.* 2004), which also cause the abrupt facies changes and highly variable lithological units above and below the sulfides. Figure 3.4 shows the schematic of the stratigraphic sequence and the position of the mineralisation in the Neves Corvo mine area.

Lithologically distinctive stratigraphic units that are large enough to trace and map and may be subdivided into members and gathered with other formations into groups can be described as lithostratigraphic sequence. The first and the lowermost lithostratigraphic unit is the Phyllite-Quartzite group. The Phyllite-Quartzite formation of the late Famennian Phyllite-Quartzite group is composed of dark shales, thin-bedded siltstones and quartzite at Neves Corvo. The Phyllite-Quartzite formation also has limestone, which transitions into the lower volcanic sedimentary complex.

A late Famennian to late Viséan volcanic sedimentary complex conformably overlays the Phyllite-Quartzite formation. This stratigraphic unit repeats itself in two distinct lithological suites: the lower autochthonous and upper allochthonous volcanic sedimentary complexes (Oliveira *et al.* 2004). The volcanic sedimentary complex's thickness typically varies from 100 to 1000 m, while locally being around 1,300 m thick and hosts all of the ore bodies at Neves Corvo (Tornos 2006; Rosa *et al.* 2008). The lower autochthonous volcanic sedimentary complex comprises units containing jasper and carbonate, massive sulfides and felsic volcanic rocks as well as the Neves formations. Jasper and carbonates with chloritic and seritic shales often overlay the massive sulfides, which are mostly composed of pyrite, chalcopyrite, sphalerite and cassiterite interbedded with black shales. Felsic volcanic rocks with rhyolites-rhyodacites and tuffs as well as the Neves formation, with its dark and

black pyritic shales and thin-bedded siltstones, are found in between the massive sulfide and Phyllite-Quartzite formations (Oliveira *et al.* 1997; Oliveira *et al.* 2004).

In the upper allochthonous volcanic sedimentary complex the Graça formation, with its grey siliceous shales and black shales with dispersed siliceous-phosphatic nodules, is the deepest formation. Felsic volcanic rocks made up of rhyolites that are interbedded and inter fingered with the Graça formation. Strongly altered basic intrusive volcanic rocks that consist of sills intrude rocks intercalated with the Graça and Grandaços formations. The Grandaços formation has the similar lithological signature as the Graça formation showing of carbonate lenses and nodules. The Violetas formation has purple and green shales interbedded with lenses and nodules of manganese oxide. Meanwhile, tuffites and grey siliceous shales with chert lenses compose the Godinho formation. Brancanes is the shallowest formation of the upper volcanic sedimentary complex and consists of pyrite-rich black shales, fine greywackes and thin layers of graded siltstone.

The CULM can be described as a thick sequence of geological strata that forms the final and uppermost lithostratigraphic unit of the Iberian Pyrite Belt. It is dated as being of Viséan to Serpukhovian age and covers most of the South Portuguese Zone. The CULM is locally known as the Mertola formation and has a thickness of up to a few kilometres in Portugal (Schermerhorn and Stanton 1969). It also occurs in between the tectonically repeated lithological suites of the volcanic sedimentary complex and acts as an excellent stratigraphic marker horizon to separate these two major structural panels. The Mertola formation is comprised of greywackes and dark grey shales, which form locally as near thrust sheets intercalated with conglomerates (Oliveira *et al.* 2004). The CULM is considered an important indicator of mineralisation proximity when directly overlaying jasper/carbonate exhalative units (which normally feature in the immediate hanging wall of massive sulfides).

The Strunian age (354.8 to 354.0 Ma) Neves Corvo VMS deposits are formed as product of deep submarine volcanism and hydrothermal alteration (Relvas *et al.* 2006a; Relvas *et al.* 2006b; Rosa *et al.* 2008). Stockworks, massive sulfide lenses and disseminations are the different morphological structures of the Neves Corvo orebodies that may be formed in close relationship or separately (Leistel *et al.* 1997). A major locally disturbed thrust referred as the Neves Corvo thrust controls all VMS

mineralisation at Neves Corvo as well as the stockworks and some deeply rooted feeder zones.

In this lithostratigraphic setting the CULM and main Neves Corvo thrust are the marker horizons that have been used in the exploration of VMS mineralisation at Neves Corvo.

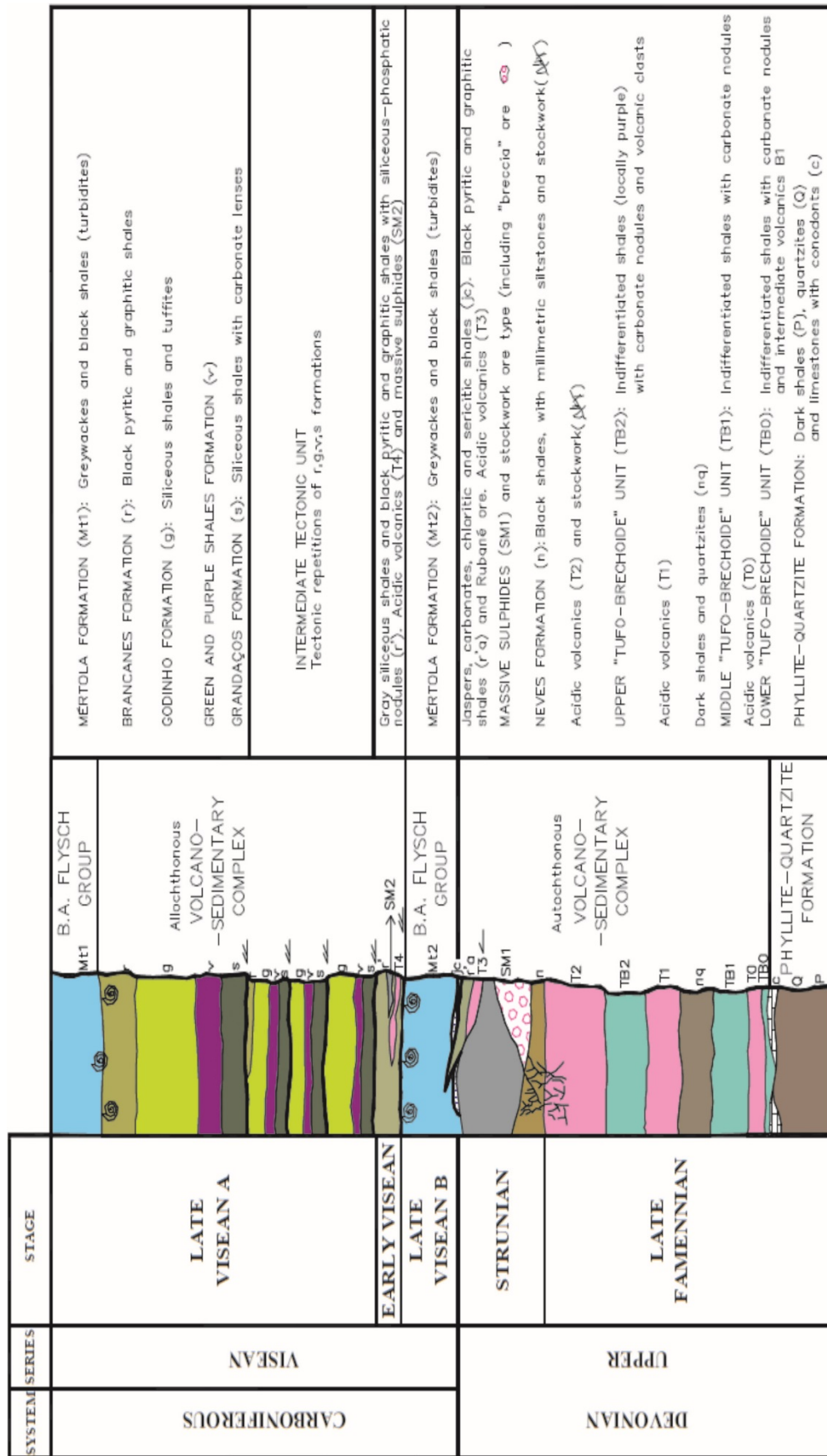


Figure 3.4 Tectono-stratigraphic sequence of the Neves Corvo mine area (Barriga et al. 1997; Meyer and Owen 2013).

3.2 Elastic property measurements

Ultrasonic pulse-transmission testing has been utilized for decades to propagate high frequency sound waves through materials to measure their elastic properties. In this project, ultrasonic pulse-transmission and specific gravity measurements were carried out to investigate the elastic properties of a large number of core samples supplied by Lundin Mining Corporation. A comprehensive database of elastic properties for the main lithological units was created with the main aim to define the seismic signature of the massive sulfide and stockworks.

The study involved 397 core samples logged in 13 different drillholes located throughout Neves Corvo and were carefully selected to represent the major lithological units. The drillhole collar logs and the downhole survey logs, which include the depth, azimuth and dip information were provided in order to be used in elastic property measurements. The lithological logs and the bulk density logs for the mineralised interval were also provided by Lundin Mining Corporation and played an important role in both the elastic property measurements and the drillhole data calibration. The lithological logs included colour, texture, alteration, structures and mineralisation of the samples. The bulk density logs were calculated through the standard water displacement technique, which uses the displaced water volume in the calculation of the density of the sample. All samples were generally in good condition with the exception of a few samples that required the ends to be squared off with a dry saw prior to measurements.

The ultrasonic pulse-transmission tests were conducted on dry samples at atmospheric pressure using an ultrasonic pulse-receiver (5077PR, Olympus Ltd.) with 1.0 MHz P and S-wave piezoelectric transducers. The arrival time of the P-wave and S-wave were analysed on a 2 GHz digital oscilloscope (Tektronix DPO 2024, Olympus Ltd.) and the resulting waveforms were digitally recorded for cross-referencing. All seismic velocity measurements were conducted on dry core samples. In addition to this the length of each sample, its weight in air and weight in water were measured for the apparent specific gravity calculation. This calculation uses the ratio of the weight of the core sample to the weight of water. The set-up for ultrasonic velocity measurements at atmospheric pressure is shown in Figure 3.5. All of these parameters allowed for physical (P-wave velocity, S-wave velocity, V_p/V_s

ratio, density, acoustic impedance and elastic impedance) and geo-mechanical properties (Poisson's ratio, Young's modulus, bulk modulus, P-wave modulus and shear modulus) to be calculated.

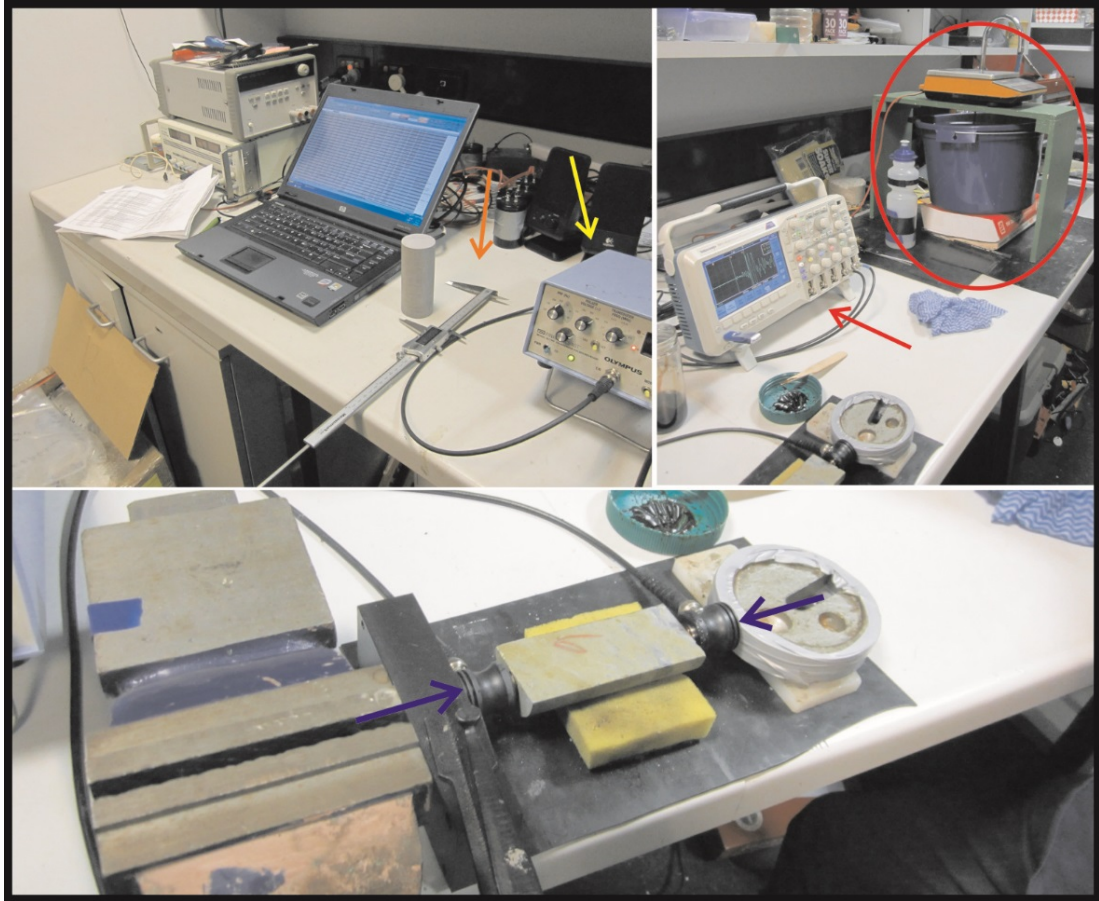


Figure 3.5 The set-up for ultrasonic velocity measurements at atmospheric pressure. Arrows point out the equipment that are used in the measurements, such as a caliper (orange), the ultrasonic pulser-receiver (yellow), the digital oscilloscope (red) and S-wave transducers (blue). The density measurements set-up is indicated with a red ellipse.

Transmission measurements were mostly taken along the axial direction of the samples. Cracks, fractures, voids, pore space and abrupt lithological changes have strong control over the P and S-wave arrivals. In order to deal with the ambiguous P and S-wave arrivals some measurements were verified with the measurement taken along the radial direction. The massive sulfides, stockworks and rhyolite core samples are illustrated with their physical properties in Figure 3.6.

As discussed in Malehmir *et al.* (2013), due to significant deformation and metamorphism crystalline rocks have very low porosity values, which make them

less pressure and frequency dependant. Therefore, the properties obtained from the laboratory measurements could be considered as representative of *in situ* properties. All these obtained parameters and the various logs were then combined into a comprehensive database and used in the next sections and the chapters. Along with the standard P-wave velocity versus density (Figure 3.7) and acoustic versus elastic impedance (Figure 3.8) cross-plots, the obtained properties were also collocated by drillhole, lithology and depth and were then investigated to identify the separation between massive sulfides, stockworks and rhyolites. The crossplot in Figure 3.7 show that massive sulfides, due to its high density and velocity values, were plotted as an end member and were clearly separated from host rocks as well as stockwork units. Not surprisingly, the crossplot between acoustic and elastic impedances in Figure 3.8 shows massive sulphides significantly separated from all other rock types. The stockworks separation was smaller but still clearly distinguishable.

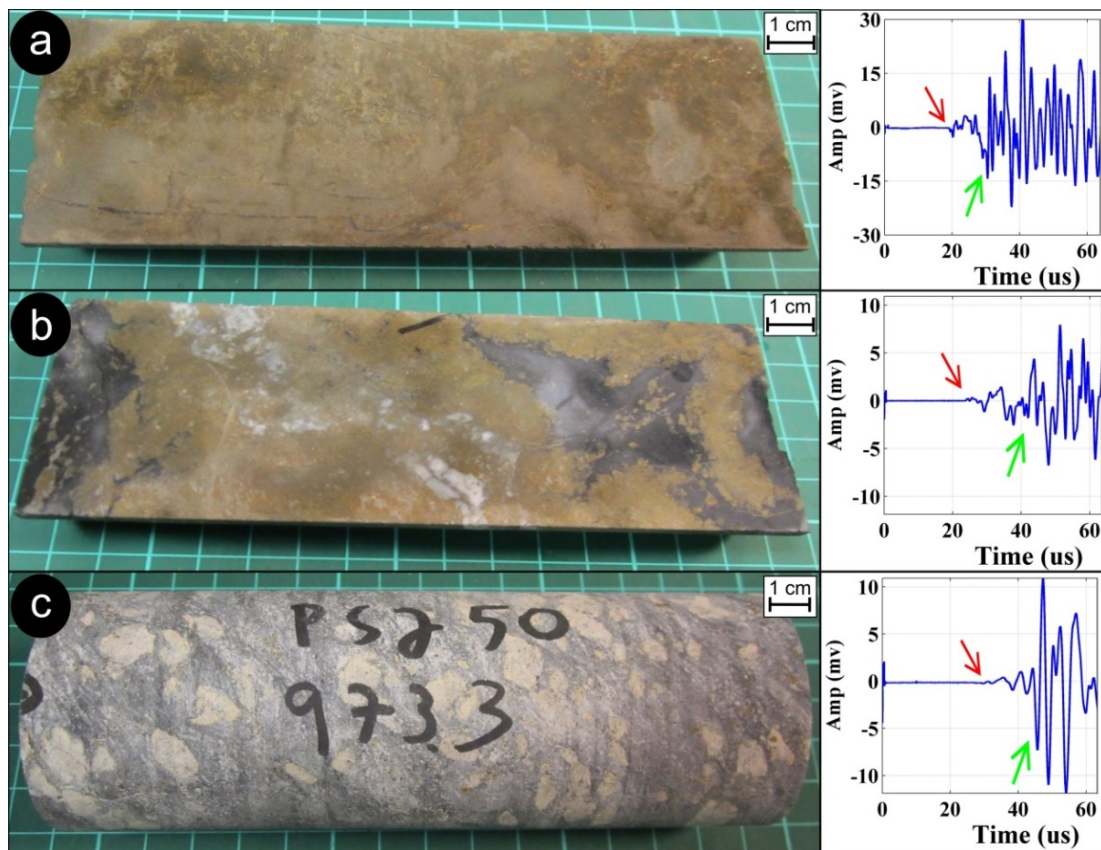


Figure 3.6 The NQ size samples of PSJ50, including **a)** massive sulfide, **b)** stockworks and **c)** rhyolite samples and their digital waveforms (on the right). Red arrows point out the P-wave arrivals and green arrows point out the S-wave arrivals that were used in the velocity calculations. **a)** The dark yellow massive pyrite sample with 133.59 mm length and 889.5 m depth. The physical properties of this sample are 7182 m/s P-wave velocity, 4498 m/s S-wave velocity, 4.784 g/cc density, 34360

m/s.g/cc acoustic impedance and 21518 m/s.g/cc elastic impedance. It has 0.37% Cu, 0.47% Pb, 6.5% Zn, 36% Fe and 10% S content. **b)** A sample containing 70% copper pyritic stockwork veins as well as dark-grey shales and 5% quartz. It has a length of 147.78 mm and was taken from a depth of 924 m. The physical properties of this sample are 6262 m/s P-wave velocity, 3527 m/s S-wave velocity, 3.661 g/cc density, 22924 m/s.g/cc acoustic impedance and 12912 m/s.g/cc elastic impedance. **c)** A sample containing pale greyish rhyolite with 30% carbonate nodules. It has a length of 136.75 mm and was taken from a depth of 973.3 m. The physical properties of this sample are 4699 m/s P-wave velocity, 3080 m/s S-wave velocity, 2.791 g/cc density, 13118 m/s.g/cc acoustic impedance and 8597 m/s.g/cc elastic impedance.

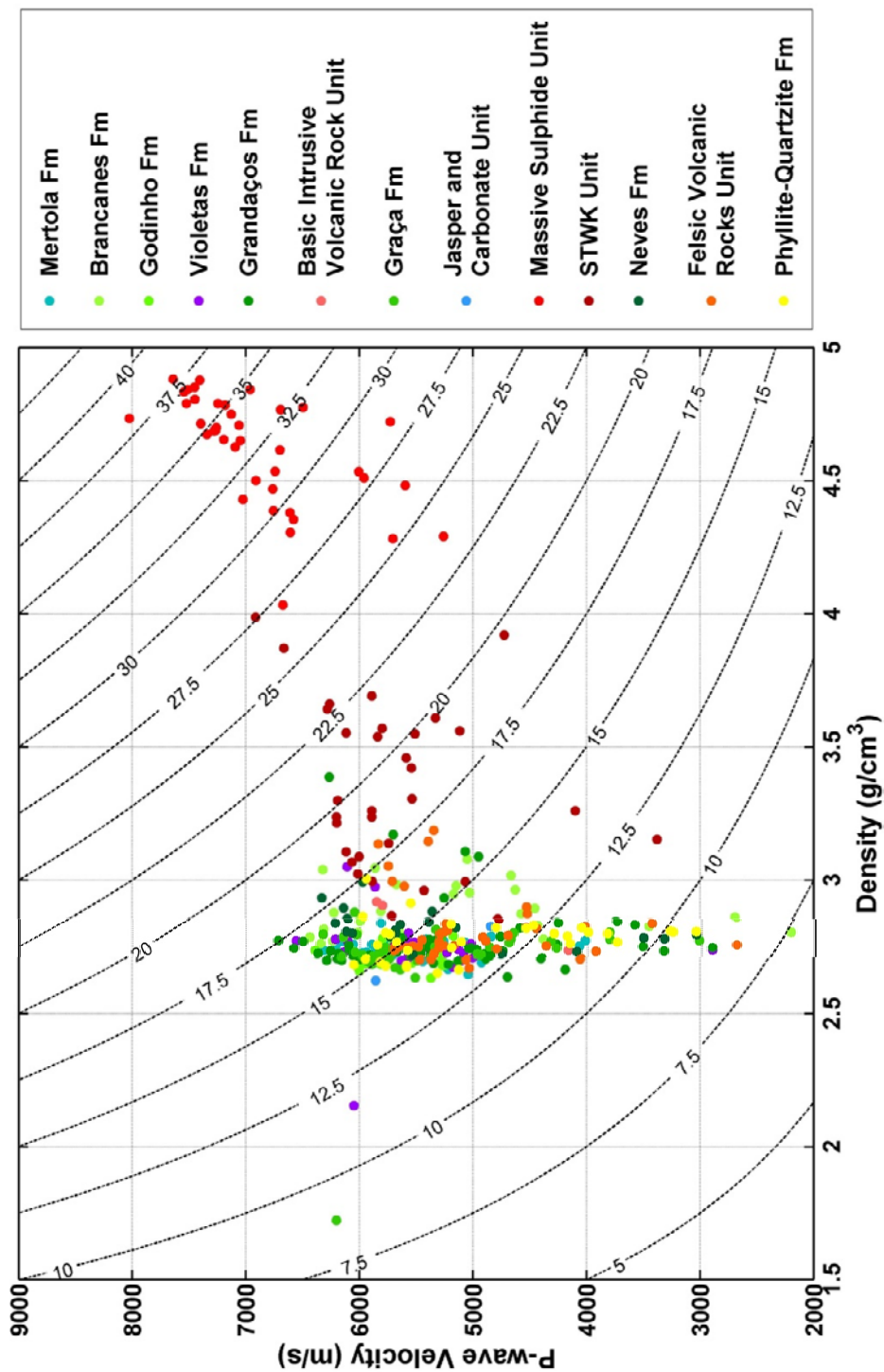


Figure 3.7 A P-wave velocity and density cross-plot collated by the main lithological units displayed with constant acoustic impedance iso-contours (dashed-lines). The samples were from 13 drillholes covering the study area. The maximum velocities are associated with clustering of massive sulfide and stockwork units, which also show higher acoustic impedance values when compared with the rest of the lithological units.

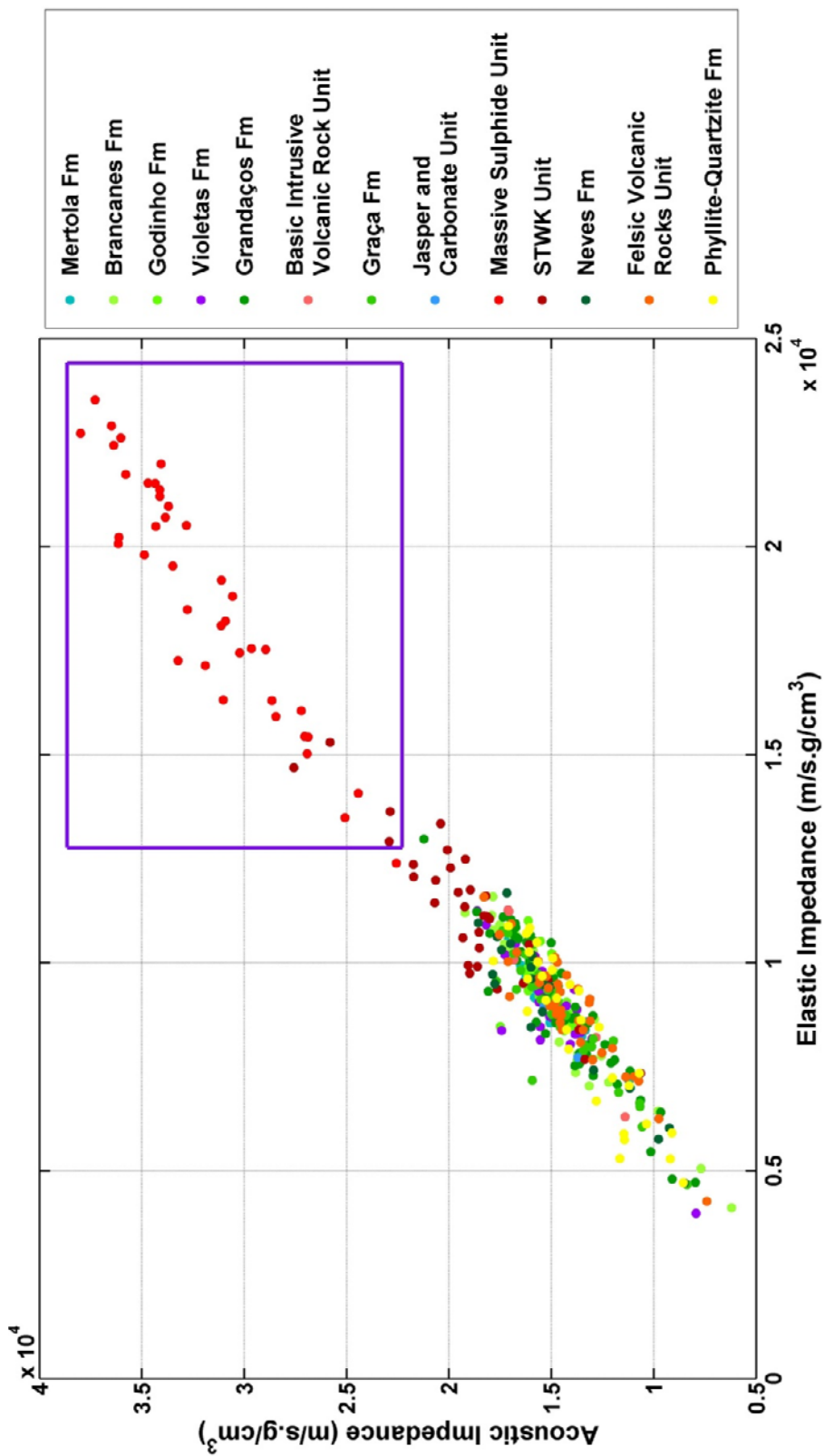


Figure 3.8 Acoustic and elastic impedance cross-plot, collated by main lithological units which displays an almost unique separation of VMS.

3.3 Drillhole Data Calibration

In order to associate the geology with the physical rock properties over the Semblana orebody, the elastic property measurement results and the various logs were analysed in a comprehensive database and calibrated with drillhole data. This study was mainly aimed at getting the synthetic response of major lithological units in order to understand the potential benefits of PRA processing in discriminating between massive sulfides, stockworks and rhyolite. Since the cost and effectiveness of routine FWS logging could be an issue in mining exploration, an additional and very important objective was to test the applicability of pseudo logs in performing drillhole-to-seismic ties instead of the FWS logs.

Drillhole data calibration began by collating all the information related to drillholes PSJ50, PSK50, SZ24A, PSO44 PSN42 and PSK48 (Figure 1.2). Elastic property measurements existed for all these drillholes except for PSN42 as well as three FWS logs for PSJ50, SZ24A and PSN42. All measured drillhole samples were specifically selected from the top and bottom of major lithological units within the sampled interval. Additionally, the geological logs were integrated into the analysis to identify and crosscheck the position of these major lithological units. This allowed us to create the representative pseudo logs by simply embedding the physical property values into the log at the appropriate depth. These pseudo logs were then generated for all drillholes including PSJ50 and SZ24A, which already had FWS measurements.

The crosschecking of pseudo logs created for drillholes that already had FWS logs provided a form of quality control by comparing the values of the pseudo logs with the actual FWS logs. To carry out the quality control and to test the applicability of using pseudo logs as a viable alternative to FWS logging, drillhole PSJ50 was selected due to its good quality FWS log and frequent core measurements. An additional level of control was achieved by displaying and analysing FWS logs together with mineral composition logs for PSJ50 (Figure 3.9a). After extracting a wavelet (60 Hz dominant frequency, zero phase) from the seismic cube, synthetic seismograms were computed for both logs and compared in Figure 3.9a. A good level of agreement between the physical rock properties measured on core and those logged by downhole tools (FWS) suggested that pseudo logs provide a viable

alternative to holes that were not logged by downhole methods and can be utilized for data calibration throughout the volume.

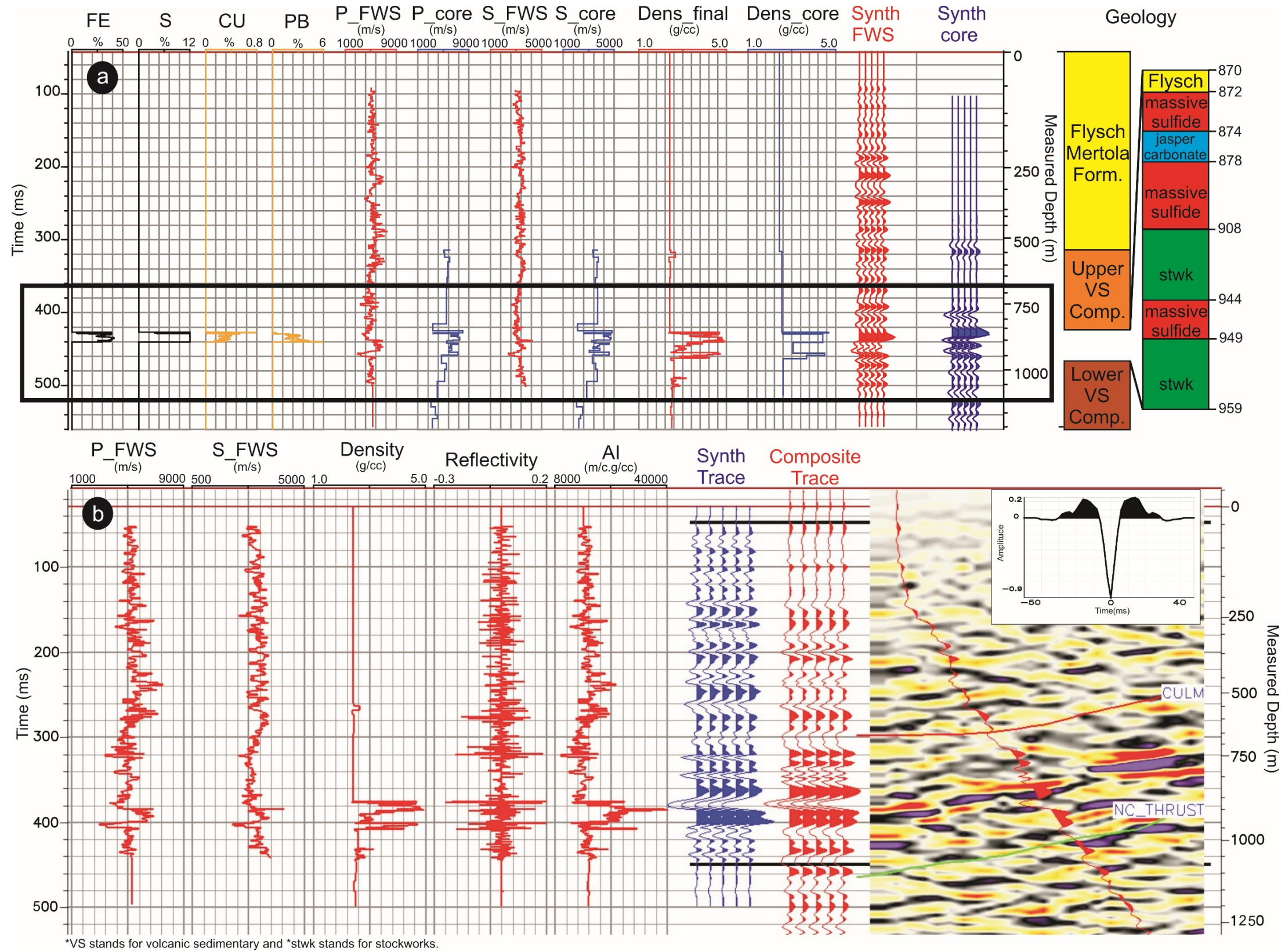


Figure 3.9 Drillhole PSJ50 (a) FWS and pseudo log correlation and (b) drillhole-to-seismic tie. Iron and Sulphur (black), Copper and Lead (yellow), FWS logs (red are P and S-wave velocities), pseudo logs (blue P-wave velocity, S-wave velocity), drillhole density data (red), pseudo log density data (blue), computed reflectivity with FWS (red) and computed reflectivity with pseudo logs (blue) are displayed respectively. The level of correlation was analysed in the window indicated by the black rectangle. The successful matching of FWS and pseudo logs in (a) provided the confidence to use pseudo logs for the future calibration of seismic-log data. The extracted wavelet is shown in the right upper corner and a PRA section is on the right with the deviated drillhole trajectory composite trace shown. A log-core match of 73% was achieved for a data window length in between the black lines. The colour scale of the PRA section is the same as Figure 3.10.

To strengthen this argument we needed to first establish that FWS logs could be used to calibrate seismic data with drillhole lithological logs to a good level of correlation. This was established through the process of drillhole-to-seismic ties. A composite seismic trace was extracted from the data cube along the drillhole trajectory and used in the correlation with the synthetic seismogram derived from the logs. It should be noted that FWS in hard rock environments is prone to errors due to the typically weak signal and highly deviated drillhole paths used to intersect steeply dipping geology, which can change gradually or abruptly over a short depth or lateral distance. The correlation of such logs with seismic - that is in its own right prone to imaging errors - is difficult (White and Simm 2003). Consequently, correlation coefficients above 0.7 are considered good or more often very good (Behrens *et al.* 1998; Duchesne and Gaillot 2011; Harrison 2009; Harrison and Urosevic 2012). For our case in PSJ50 the correlation coefficient for the data window length was 0.73 (Figure 3.9b). This impressive drillhole tie coupled with the good agreement between pseudo and real logs of PSJ50 suggested that we could use pseudo logs for seismic calibration throughout the cube. This was important to establish as we did not have FWS logs for the drillholes that penetrated massive ore.

Hence, pseudo logs were used to analyse both the zero and offset based reflectivity of the massive ore. This is shown in Figure 3.10, where very high reflectivity was recorded from massive ore in PSK50. Consequently, we had a very high level of correlation (0.87) between seismic and synthetics derived from the pseudo logs for PSK50 (Figure 3.10a). The high correlation in PSK50 was also related to the relatively simplified reflectivity function derived from core tests. This encouraging result stimulated further core tests in this area.

An additional yet very important exercise was to compare the seismic response over massive ore with the seismic response over rhyolites, as this would pave the way for the application of amplitude based targeting. Drillhole SZ24A, which exists outside of the reprocessed sub-dataset, was used to conduct the modelling of the expected seismic response of rhyolites as it was the only hole that had both FWS recorded and penetrated rhyolite without the influence of mineralisation (Figure 3.10b). To achieve this, the same methodology as before was implemented in order to correlate the synthetic seismogram with a subsequent independently reprocessed PRA version of the full seismic dataset that encompasses the location of SZ24A. The PRA

reprocessing of the full seismic dataset used the same processing sequence as this study, as it was partly prompted by its results. After correlation, an apparent reflectivity response was recorded coinciding with rhyolite. But this reflectivity was only in a relative sense, where the case consisted of massive ore not being in the vicinity. In an absolute sense, we found that massive ore produces much higher reflectivity compared to that of rhyolites. However, in an AGC-scaled section the difference between the two could diminish and amplitude based targeting might be prone to errors. It was therefore of paramount importance to process the seismic data with relative amplitude preservation in order to improve the targeting of mineralisation from seismic data in this region.

After investigating the different seismic responses associated with that of massive sulfides and rhyolites using drillholes PSJ50, PSK50 and SZ24A, zero and offset based modelling of the reflectivity of massive ore were additionally analysed with the rest of the pseudo logs for drillholes PSK48 and PSO44 (Figure 3.11). A very high level of correlation (0.83) was achieved during the drillhole-to-seismic tie of PSO44 (Figure 3.11b). PSK48 exhibited a correlation of 0.78 (Figure 3.11a). The high correlation values for these two drillholes were achieved due to the high reflectivity of massive ore and relatively simplified reflectivity function computed from the pseudo logs, similar to PSK50.

The FWS log associated with drillhole PSN42 only recorded 470 m of data and did not include a density log. Coupled with the fact that it did not penetrate mineralization, the correlation coefficient of the attempted drillhole-to-seismic tie was very low and it was therefore not calibrated with seismic data. However, it was retained as a control drillhole and the P and S-wave logs were used during the crosschecking of further interpretations and inversions in section 4.3 and chapter 5.

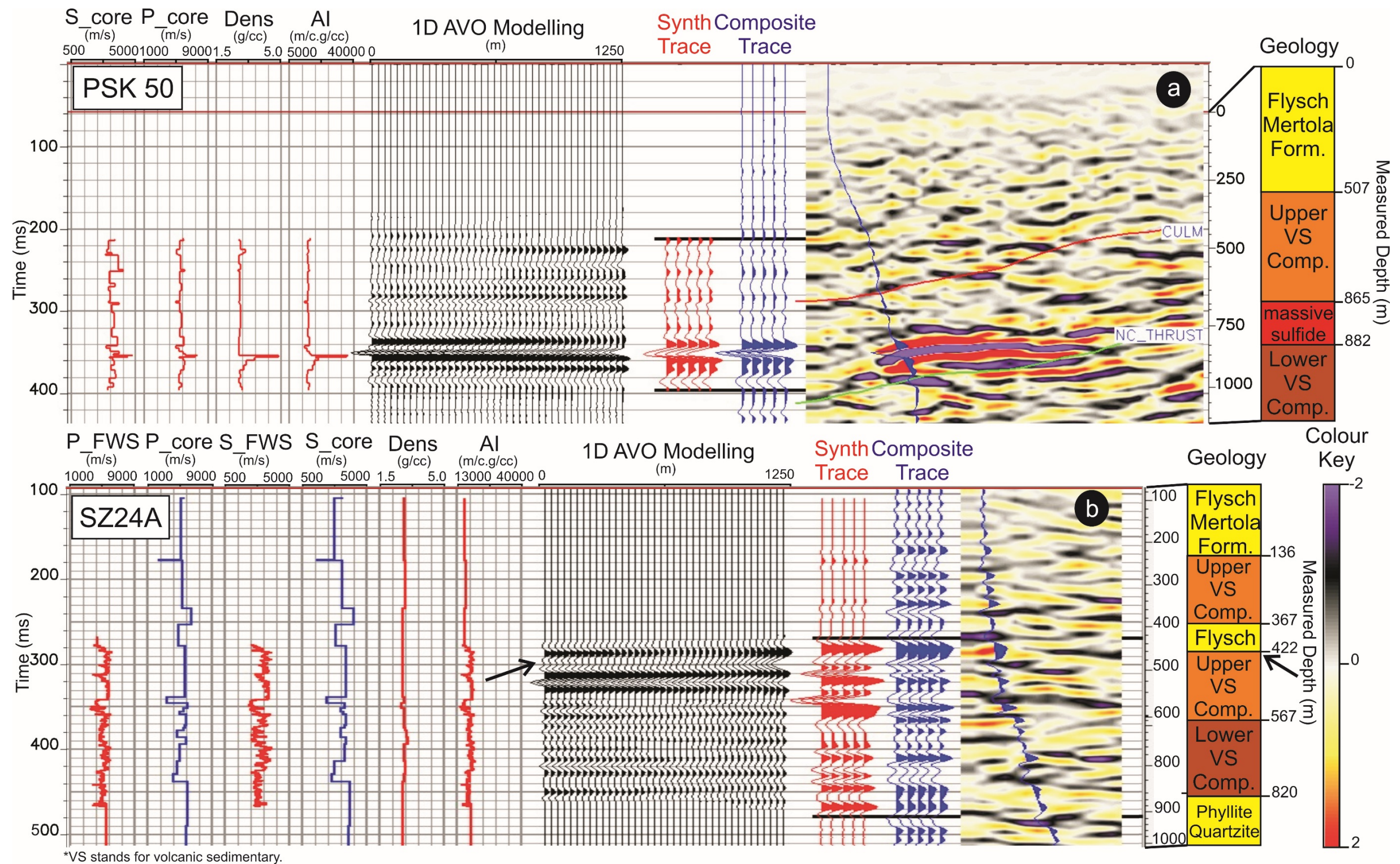


Figure 3.10 Drillhole-to-seismic tie of: (a) PSK50 and (b) SZ24A. The logs for drillhole PSK50 were derived from core sample measurements and are shown, left to right as S-wave, P-wave, density and impedance logs respectively. A synthetic seismogram was subsequently computed by convolving the reflectivity function with the wavelet extracted from the seismic cube around the drillhole. A composite seismic trace (blue) was extracted from the data cube along the drillhole trajectory and correlated to the synthetic seismogram (red) for the data window length (in between the black lines). A high correlation value (0.87) was achieved for pseudo log PSK50 as shown in (a), particularly for massive sulfides. It was clear from this that the strong reflectivity of massive ore is fully confirmed. The same correlation process was repeated for drillhole SZ24A in (b) for the data window length (in between the black lines). FWS logs are shown in red while pseudo logs derived from core sample measurements are shown in blue. The agreement was reasonably good (0.60) for a correlation carried out using FWS data. Overall, the magnitude of reflectivity for this drillhole was lower than drillhole PSK50, which penetrated through a massive ore zone. Hence, the correlation values are lower as the signal-to-noise ratio was lower for drillhole SZ24A. It was clear that the massive sulfide unit stands out with a high impedance value on the logs and a bright reflection on both synthetic and real data. The rhyolite unit (dark arrows) shows good relative (local) reflectivity but in absolute terms was much lower than massive ore.

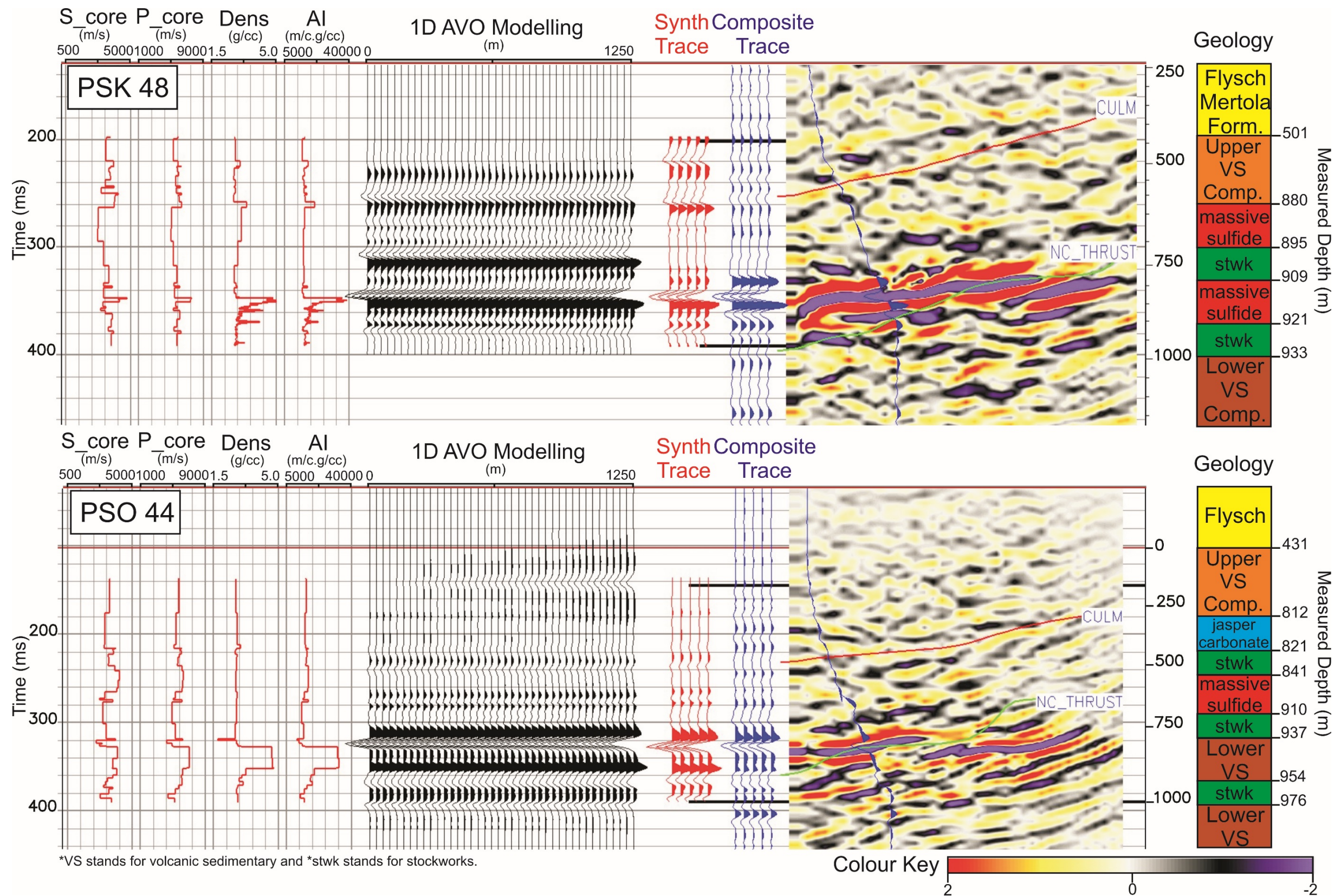


Figure 3.11 Drillhole-to-seismic tie of: (a) PSK48 and (b) PSO44. The logs for drillhole PSK48 and PSO44 were derived from core sample measurements and are shown, left to right as S-wave, P-wave, density and impedance logs respectively. Synthetic seismograms were subsequently computed by convolving the reflectivity function with the wavelet extracted (same as Figure 3.10) from the seismic cube around the drillholes. The composite seismic traces (blue) were extracted from the data cubes along the drillhole trajectories and correlated to the synthetic seismograms (red) for the data window length (in between the black lines). High correlation values were achieved for both drillholes and the strong reflectivity of massive ore is verified.

3.4 Summary

In order to successfully image the Semblana orebody in detail, as well as to delineate other major geological structures, a sound geological understanding of the Iberian Pyrite Belt, Neves Corvo mine and Semblana orebody itself was required. Key stratigraphic and geological structures, such as the Phyllite-Quartzite group, volcanic sedimentary complex, Flysch and Neves Corvo thrust were specifically highlighted as they are essential elements to be seismically modelled.

Following this geological understanding, elastic property measurements were used to characterize the geology in terms of rock physics and entered into a comprehensive database. The physical properties of major geological units and different types of mineralization were then analysed through various crossplots. Despite the complexity of the geological setting and mineralization geometry it was decided that PRA processing for the Semblana sub-dataset would provide valuable information due to the unique separation of massive sulfides and stockworks from the non-mineralized units.

As it was stated in section 1.1, certain high priority seismic reflectors that were identified from the conventionally processed dataset were subsequently drilled and found to be rhyolites. The anomalously high amplitude response of rhyolite in a relative sense was further investigated through a detailed drillhole calibration study. The synthetic seismic response of major lithological units was modelled in order to discriminate the mineralization from the rhyolites. It was proven that massive sulfides had by far the most dominant reflectivity within the seismic data while rhyolites produced a considerably weaker response. This result once more verified the potential benefits of PRA processing.

Additionally, a careful core sample selection process including adequate sampling down the hole and correlating with lithological logs helped demonstrate that pseudo logs could act as a proxy for FWS logs as demonstrated by a high correlation between the two. This confirmed that the pseudo logs could represent *in situ* properties in hard rock seismic and as such verified the applicability of pseudo logs in performing drillhole-to-seismic ties in the place of FWS logs. Hence they can be utilised in the process of acoustic and elastic inversion.

Chapter 4

Preserved Relative Amplitude Processing

In seismic exploration, PRA processing is used to preserve the broadest signal and relative amplitudes inherent in the input data (Yilmaz 2001) because any undesired distortion in the amplitude of seismic reflections could be significantly misleading (O'Doherty and Anstey 1971; Taner and Koehler 1981). Since hard rock seismic processing often suffers from an intrinsically low signal-to-noise ratio, attenuation and scattering due to piece-like complex geology with complex intrusions, faulting and lateral variations (Salisbury *et al.* 2000; Urosevic *et al.* 2012), successful imaging is directly related to the recovery of the relative amplitudes of patchy and poor reflections.

Conventional hard rock seismic data processing does not commonly utilise PRA techniques, but rather a robust automatic gain control (AGC) is applied instead to enhance weak signals at the expense of relative amplitude variation. Such processing is considered beneficial for structural interpretation but it can be very harmful for rock characterisation and the targeting of ore shoots. This study, however, shows that successful imaging can be accomplished in hard rock environments with the careful application of PRA processing.

In 2011, a standard hard rock seismic processing flow involving AGC was carried out on the data acquired at Neves Corvo, which clearly imaged the Semblana orebody. However, after integrating the results of drilling, seismic imaging, elastic property measurements and modelling it was clear that the impedance contrast between mineralised zones and the host rock is much higher than it appeared on the AGC processed data. Hence, it was worth testing if PRA processing could improve the image quality and particularly the seismic expression of the Semblana mineralised complex. It was hoped this approach would better resolve the unique seismic response of VMS within this particular complexly deformed geological environment and greatly improve the potential success of direct targeting through seismic imaging. Additionally, a PRA data set would enable proper drillhole ties and the application of seismic inversion. This in turn will produce an appropriate input for the application of a detailed volumetric interpretation. In this project, a 4.5 km² sub-dataset encompassing the Semblana orebody was reprocessed with PRA processing.

This chapter includes excerpts from the paper “Yavuz S., Kinkela J., Dzunic A., Penney M., Araujo V., Neto R., Ziramov S., Pevzner R. and Urosevic M., 2015. Physical Property Analysis and Preserved Relative Amplitude Processed Seismic Imaging of Volcanogenic Massive Sulfides – A Case Study from Neves Corvo, Portugal. *Geophysical Prospecting - Hard Rock Seismic Imaging Special Issue 63* (4), 798-812.” that was published by the EAGE in July 2015 (Copyright 2015 by the European Association of Geoscientists & Engineers). This reference is no longer cited in the following.

4.1 Seismic Data Acquisition

Between February and June 2011, HiSeis Pty Ltd carried out the acquisition of seismic data over the Neves Corvo mine using a Seistronix EX-6 seismic acquisition system (Kinkela 2011a). This system was used to record the data over a patch of 10 Hz single point geophones from two alternating (flip-flop) vibroseis seismic source trucks (Mertz M22-601) (Kinkela 2011a). Coordinate surveying began prior to acquisition and continued through during acquisition by a sub-contracting company (GeoIng Ltd.). This surveying consisted of land reconnaissance, source/receiver point staking and later source vehicle spotting tasks.

Seismic data acquisition covered an approximate area of 24 km² with 23 patches. The Semblana sub-dataset that is the focus of this study includes 4 receiver and 4 sources patches arranged in a cross-pattern, covering an approximate area of 4.5 km². Each receiver patch consisted of 11 geophone lines. Both receiver and shot patches are overlapped by 50% throughout the acquisition area to achieve high and uniform fold. The acquisition parameters for this sub-dataset are listed in Table 4.1.

Table 4.1 Acquisition parameters for PRA processing of the Semblana sub-dataset.

Parameter	Value
Total Acquisition Area	4.556 km ²
Number of Patches	4
Number of Receiver Lines	22
Maximum Nr. of Live Receiver Lines/Patch	6
Maximum Number of Live Channels/Patch	648
Number of Live Channels/Receiver Line	108
Receiver Interval	15 m
Receiver Line Interval	90 m
Number of Shots	2652
Number of Source Lines	19
Source Interval	45 m
Source Line Interval	90 m
Maximum Offset	1757 m
CDP Bin Size	22.5m x 15m
Maximum Fold	211
Total Number of CDPs	13736
Inline/Number	136
Crossline/Number	101
Geophones	10 Hz single
Record Length	3 s
Sampling Rate	2 ms
Source	2x30k lb Vibroseis (10-120 Hz)

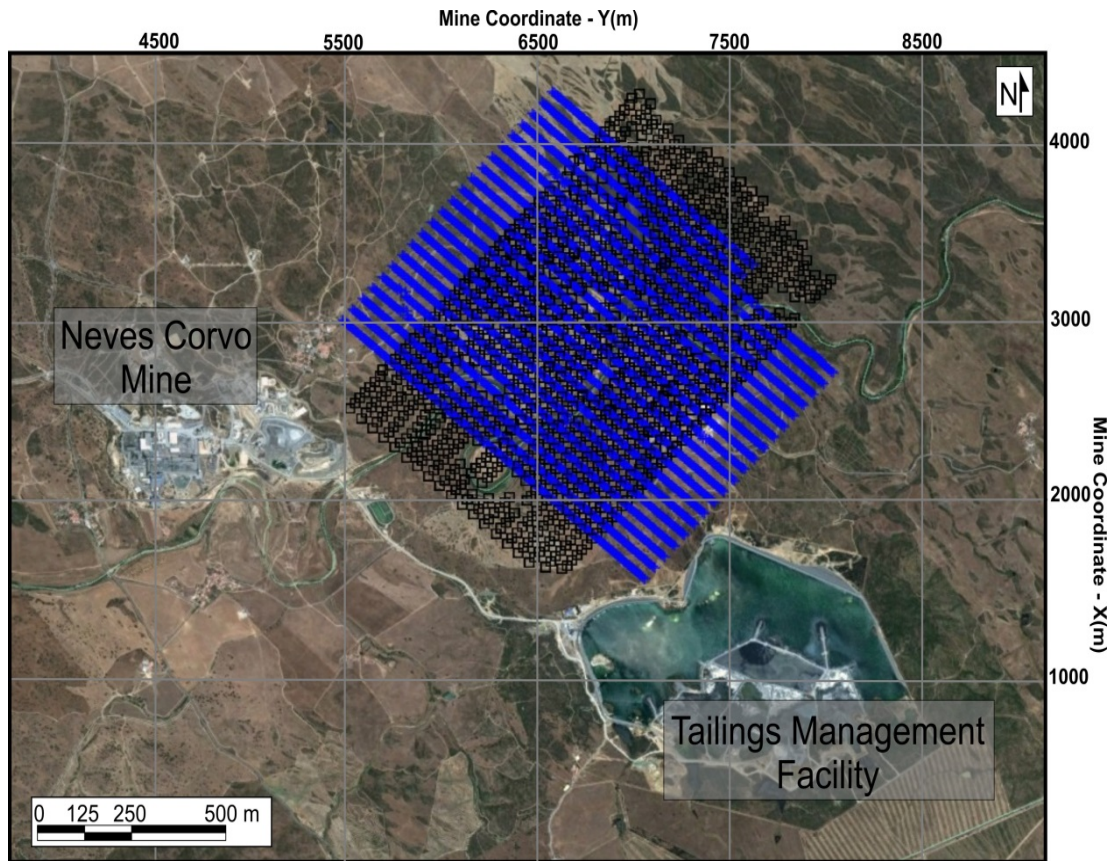


Figure 4.1 Plan view of the seismic data acquisition area. Black squares and blue crosses point out the source and receiver locations used in the Semblana seismic dataset acquisition respectively.

The plan view of the seismic data acquisition area is displayed in Figure 4.1. The Semblana sub-dataset covers an area located to the east of the main Neves Corvo mine facility and northwest of the tailings management facility. This survey area had up to 100 m in topography change with almost no obstacles around. The survey design was able to cover this area with a CDP fold of up to 211, which provided a high S/R ratio and allowed for PRA processing. The Semblana sub-dataset CDP fold coverage and the source and receiver elevations are illustrated in Figure 4.2.

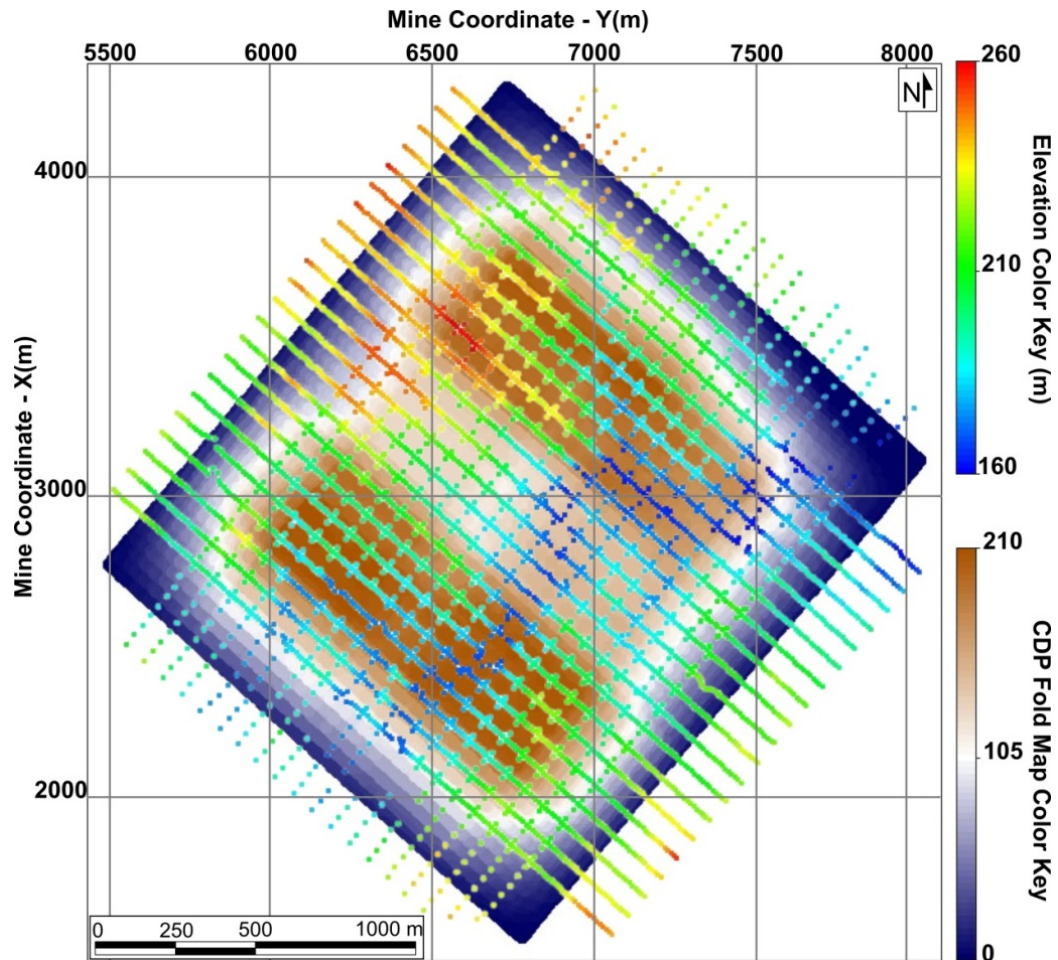


Figure 4.2 Semblana sub-data set CDP fold map overlapped with the source and receiver lines coloured by elevation.

4.2 Conventional Data Processing and Interpretation

Mineral exploration at Neves Corvo revolved primarily around drilling and utilising the existing geological understanding since the first discovery in 1977. Geophysical techniques have played a role in exploration at Neves Corvo mainly through the use of gravity, magnetics and TEM methods. In addition to these, 2D seismic reflection profiling was trialled in 1996. The data quality was poor but a subtle amplitude anomaly present in this data agreed with the known position of the Lombador orebody. No anomalies were seen over the Semblana ore body. In 2011, a 3D high resolution seismic reflection survey was performed over the Neves-Corvo prospects by HiSeis Pty Ltd on behalf of Lundin Mining Corporation. The main objectives of this survey were to image the known deep massive sulfide deposits (Lombador and Semblana) and to discover new targets within the Neves Corvo district.

The conventional amplitude non-preserving processing stream involved the application of an AGC operator at least once during the processing. Conventional hard rock seismic processing utilised the simple but robust processing flow shown in Table 4.2. The key steps were the application of refraction statics, constant velocity stack analysis (CVS), residual surface consistent reflection statics, DMO correction and post-stack migration.

This simple approach was effective in delineating major structures and producing a robust but not very precise image. This can be assigned to the inherent limitations of DMO and post-stack migration algorithms related to their low sensitivity to velocity errors and their general utilisation of simplified imaging conditions and assumptions. Hard rock seismic is known to consist of lateral as well as drastic vertical velocity variations, which cause relatively small normal move-out in the common midpoint domain (Malehmir *et al.* 2012b). Additionally, the sizes of the orebodies are generally not big enough to create coherent reflections over a significant distance, which affects the accuracy of the DMO operator. The popularity of the application of DMO-based imaging algorithms for hard rock seismic data processing lies in its low sensitivity to velocity errors. Even an erroneous velocity field will tend to produce a coherent DMO stack. Consequently, conventional hard rock seismic processing, such as that given in Table 4.2, is considered as reliable and robust and typically provides acceptable results in complex structural settings (Pretorius *et al.* 2000). The imaging errors are often subtle, unless one attempts to use seismic for the targeting of deep and complex mineral resources.

After the AGC processing, Lundin Mining Corporation and HiSeis Pty Ltd collaboratively carried out the seismic interpretation with the objective of identifying drilling targets for future massive sulfide exploration (Kinkela 2011c). It was observed that the Semblana and Lombador orebodies were clearly imaged, as well as important lithological contacts and geological structures that defined the prospective zone. Copper sulfide extensions south of Semblana were discovered by drilling high-priority targets, which were chosen based on the high amplitude responses (Lundin Mining Corporation 2013). However, other high-priority targets were also drilled and found to be non-mineralised rhyolites.

Table 4.2 AGC processing flow (Kinkela 2011b).

-
1. Binning (22.5 m x 15 m)
 2. Refraction static computation (Delay time and diminishing residual matrix) and second edit of first break picks
 3. Quality control (QC) of the refraction static solution (on shot records, every 20th shot)
 4. Application of refraction statics
 5. Window design for amplitude compensation and deconvolution
 6. Tests for: amplitude compensation, band-pass filter, Multi-channel filtering (F-K/ τ -p), autocorrelation and deconvolution
 7. Application of ensemble equalization gain,
 8. Spherical divergence correction,
 9. band-pass filter and deconvolution
 10. CVS,
 11. NMO application,
 12. Brute stack
 13. Computation of surface-consistent residual reflection statics (QC check)
 14. Application of residual statics
 15. Residual stack,
 16. Second pass CVS,
 17. Residual stack II
 18. DMO stack with F-X deconvolution
 19. NMO removal and final velocity analysis after DMO
 20. Final DMO stack with F-XY deconvolution
 21. Post stack migration (time/depth)
 22. time/depth conversion (VSP obtained from PSJ-50)
-

4.3 Preserved Relative Amplitude Processing

As previously discussed, it is common practice in conventional hard rock seismic data processing to use a quick and robust automatic gain control (AGC) rather than to implement full PRA processing. This is primarily due to PRA processing followed by the application of pre-stack imaging (usually pre-stack time migration) requiring high signal-to-noise ratios, more rigorous noisy trace editing and accurate velocity field and static corrections. Despite recent improvements in acquisition and processing, the application of a fully preserved relative amplitude processing stream on a 3D hard rock dataset has never been documented before. Hence, in this study it was hoped that by utilising a PRA seismic data processing approach followed by pre-stack time migration, its value for the direct targeting of mineralised ore bodies from seismic data could be demonstrated.

In the previous chapter, the elastic property measurements followed by drillhole data calibration clearly indicated that mineralized zones should be identifiable based on seismic amplitudes. However, successfully identifying amplitude anomalies is dependent on the preservation of relative amplitudes. This provides the basis for the application of PRA seismic data processing. An additional benefit of PRA processing was to provide the basis for the application of AVO analysis and seismic acoustic and elastic inversions that would in turn enable the improved characterisation of the Semblana orebody.

PRA processing of the Semblana sub-dataset involved several key steps designed to avoid any distortion of the seismic amplitudes potentially caused by processing algorithms. The full processing flow for the PRA processing stream is outlined in Table 4.3.

Table 4.3. PRA processing flow

1.	Geometry Specification / Binning (22.5 m x 15 m)
2.	Trace Edit / Reverse / Mute
3.	Refraction Static Corrections: Datum 270 m, replacement velocity 6000 m/s
4.	Air-blast Mute
5.	Signal/Noise Analysis
6.	Second pass Trace Edit / Reverse / Mute
7.	Shot Domain Ensemble Balancing using data window
8.	Time Power Amplitude Adjustment
9.	Surface wave noise attenuation for the computation of surface-consistent amplitude recovery scalars on shot, receiver and offset domains
10.	Interactive Radon / τ -P Analysis
11.	Application of AGC over the data window length
12.	Radon Filter: Number of P-values: 200, P value interest 0-2500 ms, white noise 0.03%
13.	AGC removal
14.	SCA Recovery – Application on shot, receiver and offset domains
15.	Surface-consistent deconvolution – spiking 60 ms gap, 0.1% white noise operator
16.	Brute stack with a 55% stretch mute and CVS-derived velocity field.
17.	Surface-consistent residual reflection statics corrections (iterative)
18.	Interactive Velocity analysis (iterative): using the CVS-derived velocities as a guide function: on CDP supergathers created with five inlines and crosslines for every tenth inline and crossline
19.	Pre-stack Kirchhoff 3D Time Migration: maximum dip 40 degrees, absolute offset of first bin centre 10 m, bin size 20 m, maximum offset 1750
20.	Normal move-out corrections (NMO) and Band-pass filter: 10 – 15 – 120 – 160 Hz Ormsby
21.	Stack and F XY deconvolution
22.	Time-to-depth conversion with smoothed VSP velocities (drillhole PSJ50)

4.3.1 Data Conditioning

Hard rock seismic commonly suffers from thick and irregular weathered layers (regolith) and heterogeneous near surface effects. Hence, the success of the seismic processing is highly dependent on accurate refraction static corrections that require accurate first break picks. AGC processing - including geometry loading and first break picking - were already accomplished in 2011. This allowed me to have a quick start in the reprocessing of the data by moving straight to the application of refraction static corrections rather than having to calculate them from the start.

Compared to the AGC processing, PRA processing is much more sensitive to noise. Therefore, trace killing, editing and muting was revised through several runs using different signal-to-noise ratio analysis techniques to ensure that only traces with a signal-to-noise ratio above a certain threshold passed through for further processing. Firstly, the air-blast was manually muted in the data. Then, first runs of trace killing and editing was carried out automatically utilizing the signal-to-noise ratio analyses. During the signal-to-noise ratio analysis, RMS values of the amplitudes were calculated for different data window lengths by considering the different offset ranges that they occupied. This allowed me to eliminate the majority of the extremely noisy traces. However, eliminating noisy traces in near offset data was deferred to the application of a radon filter to attenuate the destructive ground roll and guided waves. An example of a signal-to-noise analysis diagram that was used during the automatic trace killing phase is displayed in Figure 4.3. A mild manual trace killing was then performed followed by a revised refraction static correction applied on the improved signal-to-noise ratio data.

PRA processing then required the computation of scalars for each shot, which are calculated for all the traces within an operator window the length of the seismic trace. This facilitated the relative balancing of amplitudes based on the calculated scalars. In order to compensate for energy losses such as those due to the geometrical spreading of the seismic wave, a time - power amplitude adjustment was also applied. The results of the data conditioning can be seen in Figure 4.5.

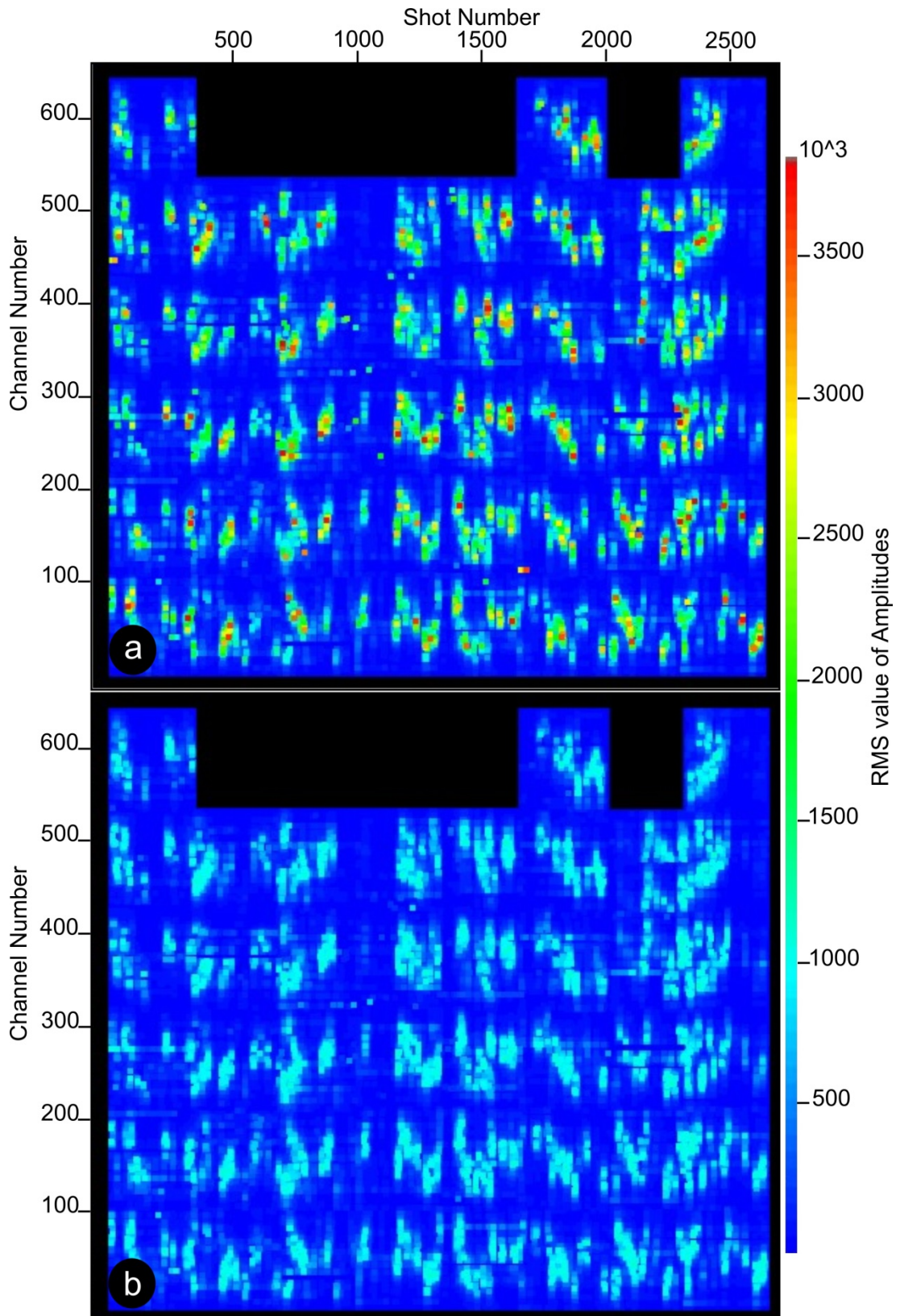


Figure 4.3 Signal-to-noise ratio analysis diagrams displaying the RMS values of amplitudes **a)** before and **b)** after the automatic trace killing. The threshold for the trace killing was selected as 1100×10^3 for offsets bigger than 450 m.

4.3.2 Surface-Consistent Amplitude and Deconvolution

The conventional data processing used Automatic Gain Control (AGC) in pre-processing due to its ability to handle and reduce anomalous noise spikes along the recorded trace at the expense of maintaining the relative amplitude distribution of signal associated with seismic events. Additionally, different types of deconvolution are included in conventional pre-processing to address the near-surface effects on the wavelet as well as those caused by the source and the acquisition system itself. Since hard rock seismic imaging suffer from near surface effects more, the application of a surface-consistent amplitude correction followed by a surface-consistent deconvolution were essential in the PRA processing of hard rock seismic data.

After data conditioning, surface-consistent amplitude scalars were calculated for each trace in the shot, receiver and offset domains in an iterative manner. The first several iterations of the scalars were calculated with respect to a single shallow horizon that was picked on a possible reflector. However, in order to achieve the right corrections for the offset component, we had to consider the noise in the near offsets created by ground roll and guided waves. To address this, temporary surface wave noise attenuation was applied to obtain the final offset domain scalar before being applied to the data.

For land data, surface-consistent deconvolution filters can be derived if the seismic trace can be broken down into its source, receiver, offset, and CDP components (Taner *et al.* 1974). Unlike surface-consistent amplitude corrections, in surface-consistent deconvolution only the shot and receiver components are applied. Following the surface-consistent amplitude corrections, a surface-consistent spiking deconvolution was calculated in source, receiver, offset, and CDP domains and accordingly applied to the dataset for all components.

These amplitude-preserved pre-processing steps allowed us to observe a significant improvement in the signal-to-noise ratio of the data (Figure 4.5).

4.3.3 Radon Filter

The most challenging step in the PRA processing of this particular 3D hard rock seismic dataset was the removal of ground roll and guided waves while still preserving amplitudes. The Radon transform is a mathematical technique that has been commonly used in off-shore seismic data processing to attenuate multiples. It transforms offset-time data into τ (zero-offset travel time) and P (ray parameter $p = \frac{\sin\theta}{v}$, θ emergence angle, V-medium velocity or simply the slope of the arriving event) domain which is naturally suited for attenuation of linear events (Tatham *et al.* 1983). Since theoretical parabolic and hyperbolic Radon transforms are prone to more errors in shallower events, the application of a linear Radon filter (slant stack) was found to be most suitable for the PRA processing in order to attenuate ground roll and other linear events that mask target reflections.

Firstly, a new header entry was created with respect to azimuth, source number and receiver line number to sort the data into a specific order for the application of a linear Radon filter. In this new order, the negative and positive offsets were separated while considering the azimuthal information. The data was then sorted primarily for the new header entry, secondarily for the absolute offsets and finally for the shot number.

An interactive linear Radon (τ -P) analysis was then carried out for all the data. An AGC operator for the length of the data window was additionally applied and later removed after the application of the radon filter. This temporary application of AGC was used to improve the performance of multichannel filters. A mild top mute was also picked in a few gathers to further improve the analysis. The interactive radon analysis for shot number 1776 displaying the top mute in the residual move-out domain (Figure 4.4b) is illustrated in Figure 4.4. After the Radon filter application, a final iteration of surface-consistent amplitude recovery and surface-consistent spike deconvolution followed by a wide band-pass filter concluded the pre-processing of the Semblana sub-dataset. The results of the pre-processing and Radon filter application are displayed in the shot domain in Figure 4.5. The effectiveness of this approach is illustrated in Figure 4.6 where in-line 61 and PSTM gathers is used to demonstrate data before and after the application of a Radon filter are shown.

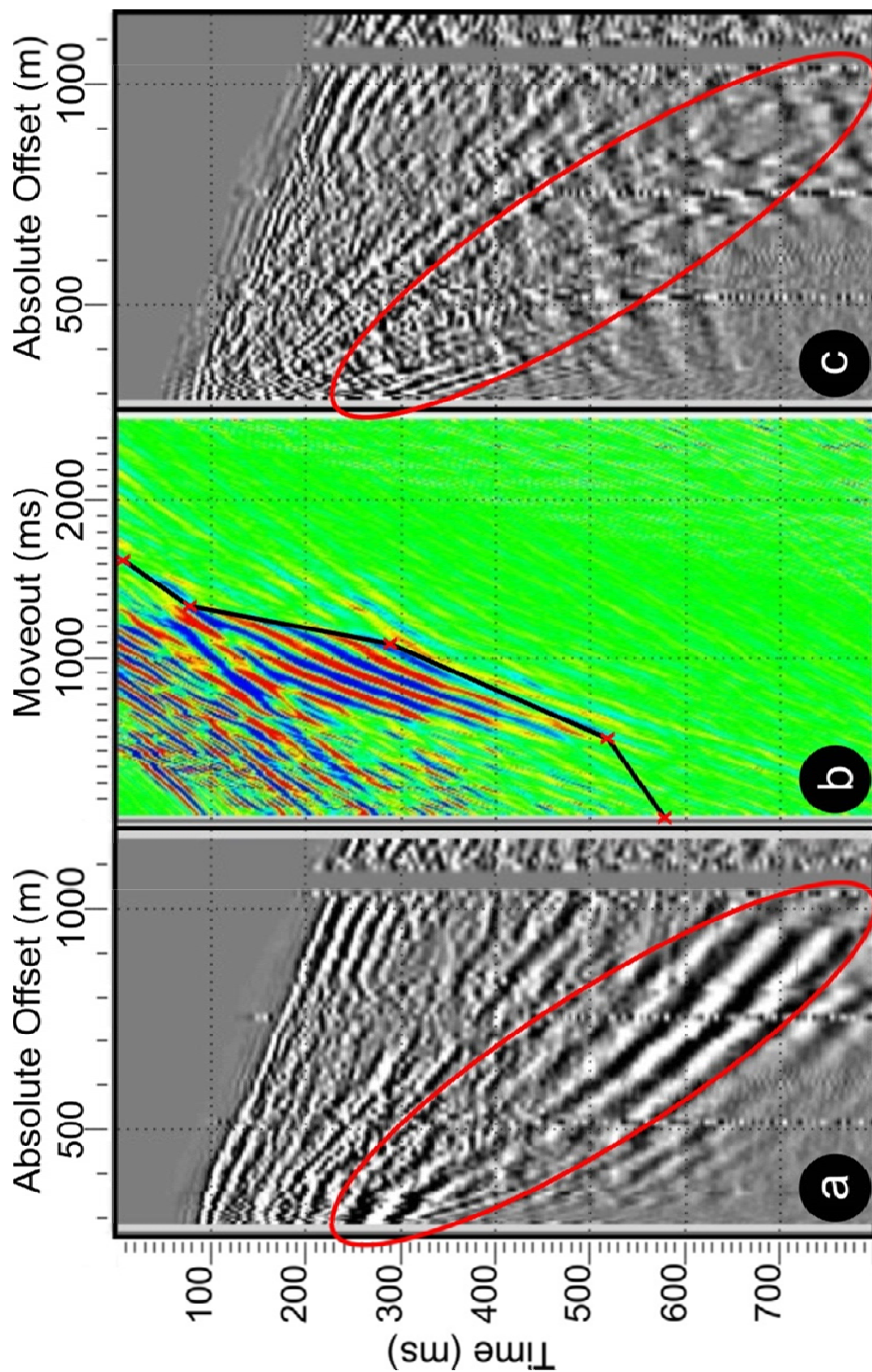


Figure 4.4 The interactive radon (τ -P) analysis for shot number 1776. **a)** The data before Radon filter **b)** residual moveout **c)** filtered data. The Radon top mute gate is highlighted by a black line in between the picks (red crosses). The ground roll and guided wave removal is indicated with a red ellipse.

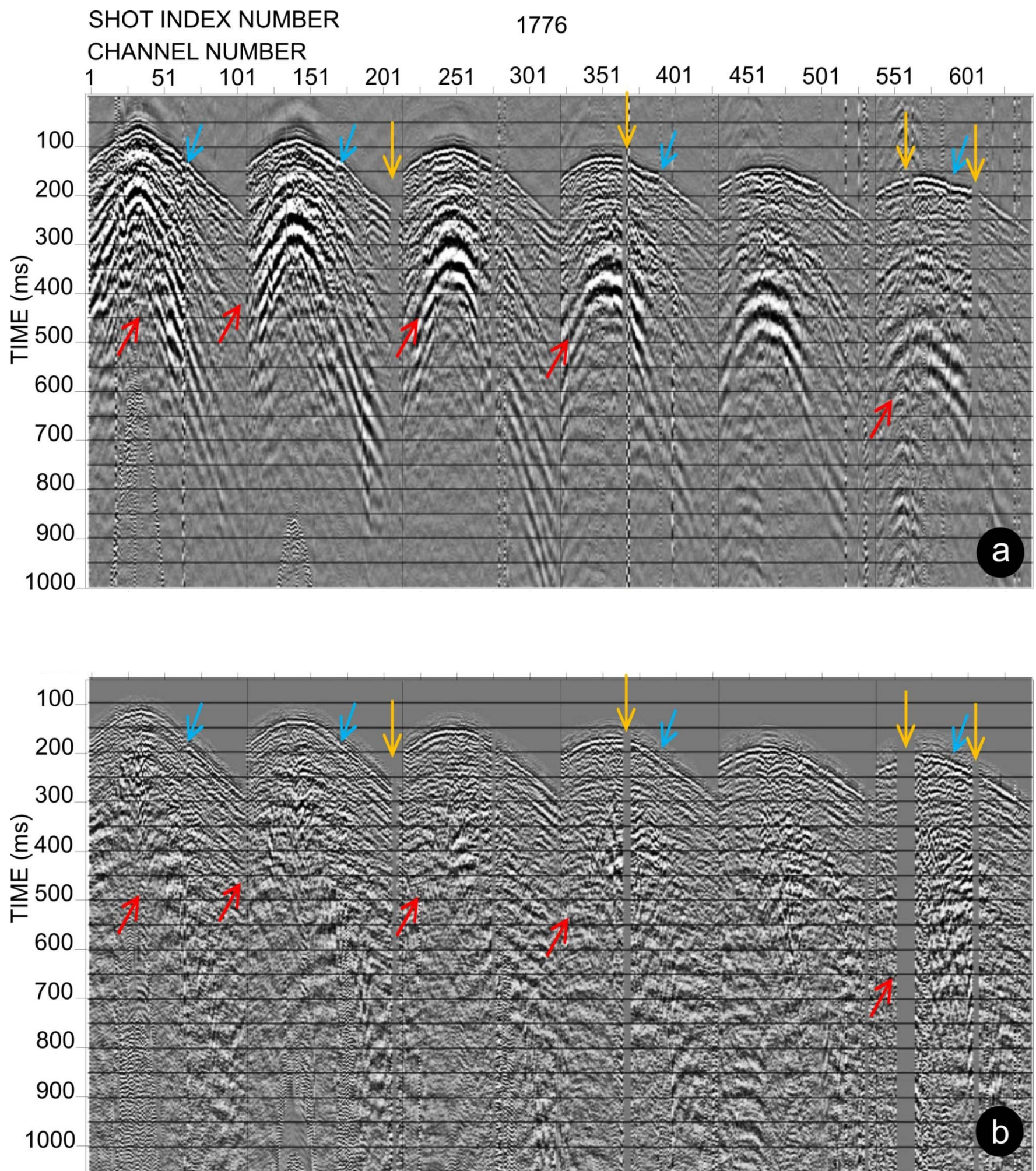


Figure 4.5 (a) A raw 3D shot gather and (b) the same gather after pre-processing. Killed traces (yellow), refraction static corrections (blue) and the removal of ground roll and guided waves with a Radon filter (red) are highlighted with arrows.

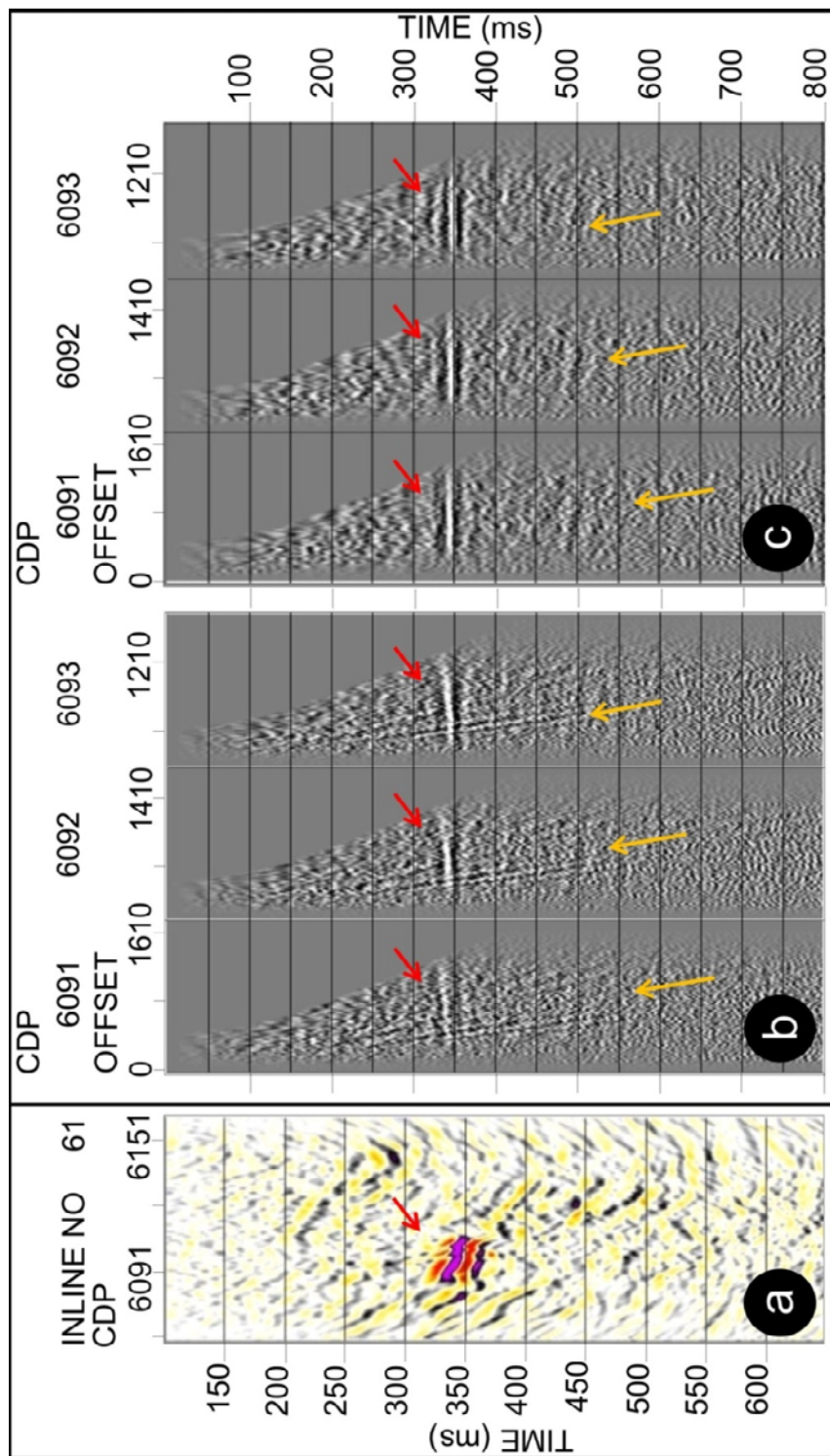


Figure 4.6 In-line 61 after the application of a Radon filter for the attenuation of ground roll and guided wave in the CDP domain. (a) A migrated stacked section over Semblana, (b) NMO-corrected CDP gathers with surface-consistent residual reflection static corrections applied before the removal of ground roll and (c) the same gathers after ground roll removal. Red arrows mark the position of Semblana. Yellow arrows mark the position of the noise of ground roll and guided waves. Signal-to-noise ratio was improved significantly after removal of coherent noise.

4.3.4 Surface-Consistent Residual Static Corrections

The application of static corrections is one of the most important steps of seismic data processing to avoid the travel-time distortions caused by topography and the near surface weathered layer. The application of the refraction static correction that was utilized in PRA processing in section 4.3.1 was specifically designed to estimate and apply the necessary corrections to be able to handle these factors.

However, residual static corrections are necessary for successful imaging as they manage the short wavelength static shifts not handled by the refraction static solution. Static time corrections (constant time shifts) on reflections times associated with deeper reflectors are routinely done by taking the surface locations of shots and receivers down to a datum below the weathered layer in a surface-consistent manner (Taner *et al.* 1974). Since hard rock seismic imaging has to deal with all these factors that in a piece-like and complex geological environment, it is extremely crucial to have an adequate residual static correction solution.

During the PRA reprocessing of the Semblana data set, surface-consistent residual reflection static corrections were calculated in an iterative manner with a revised horizon that was specifically picked for the Semblana reflector. The software algorithm that was used in the calculation of the static time corrections uses the method modified by Ronen and Claerbout (1985) (section 2.3) that estimates the surface-consistent statics by maximization of the sum of the squares (power) of the stacked section.

After the application of surface-consistent residual static corrections, the PRA stacks were compared to the AGC stacks to ensure that improvement in the data quality was being achieved. As illustrated in Figure 4.6c and Figure 4.7, the continuity and strength of the Semblana reflector improved following the application of both a Radon filter and surface-consistent residual static corrections.

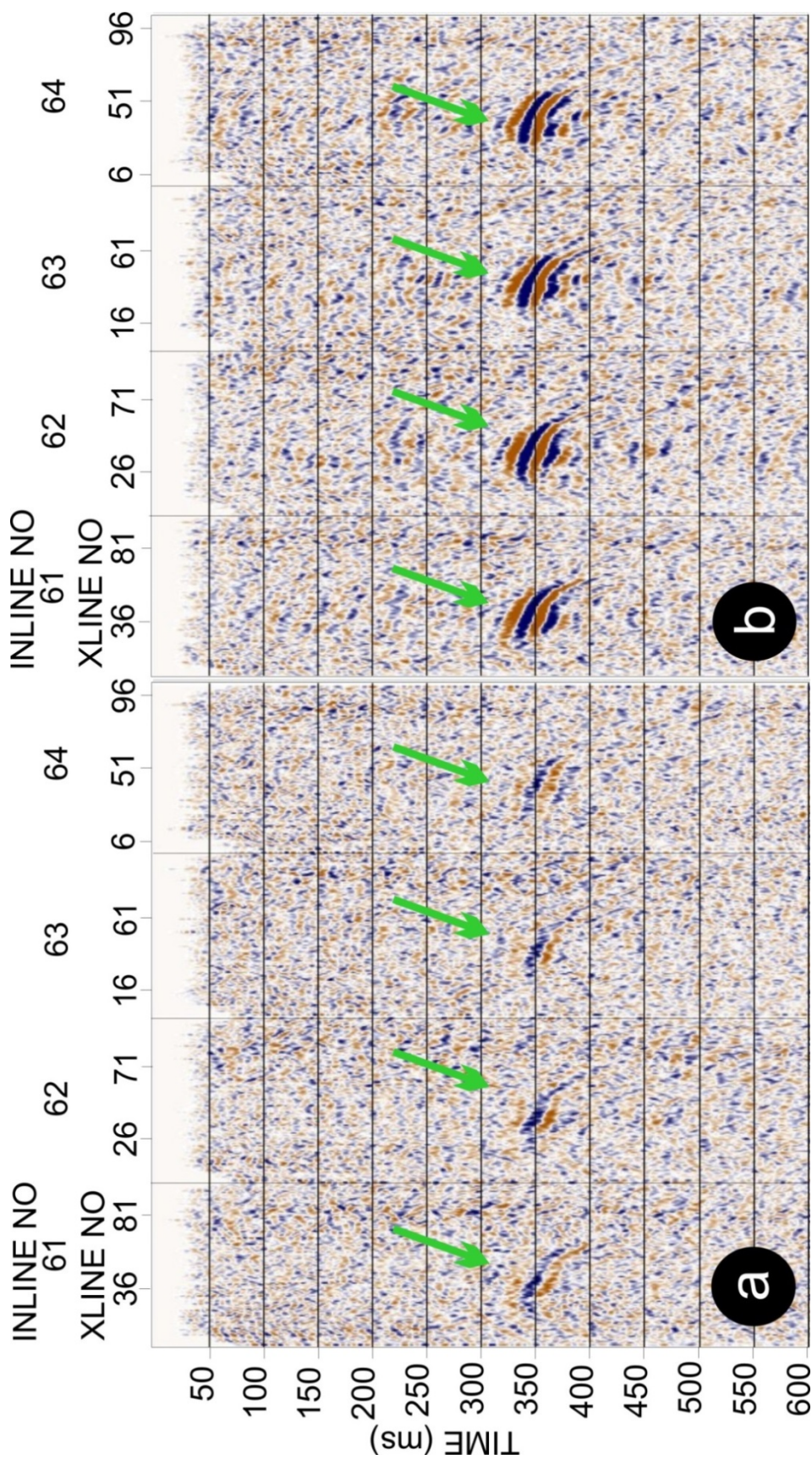


Figure 4.7 Surface-consistent residual static correction comparison. Selected inlines over Semblana: (a) brute stack and (b) residual stack. Significant improvement in reflection continuity and strength was achieved after the application of Radon filter and residual reflection statics correction.

4.3.5 Interactive Velocity Analysis

In seismic processing, velocities are routinely estimated through several methods to flatten the reflection hyperbolae for non-zero offsets in preparation for stacking the data. This is known as the normal move-out (NMO) correction. Constant velocity stacks (CVS) are one of the oldest velocity analysis methods (Sherwood and Poe 1972) that has been somewhat forgotten for many years in the oil industry but forms an essential velocity analysis tool for mineral seismic. The CVS technique is based on stacking the data with constant velocities and displaying them in panels in order to pick the most appropriate velocities for stacking the data. In 2011, the AGC processing flow utilised CVS analysis to derive the velocity field to stack the data for the final AGC cube. In the PRA reprocessing, a brute stack was obtained with these CVS-derived velocities and is displayed in Figure 4.7b.

Another common velocity analysis technique introduced by Taner and Koehler (1969) computes the signal coherency on the CMP gather with respect to offsets and displays the variation associated with different velocities versus two-way zero-offset time on a graph. From this graph, the most coherent stacking velocity can be observed from the velocity spectra and picked accordingly (Yilmaz 2001). In this method, the most accurate velocity picks show the highest coherency based on the correlation of corresponding hyperbolic travel-time trajectories that are superimposed on the CMP gather of significant reflections. In hard rock seismic processing this method can only be applied after initial velocity models has been inferred through CVS analysis (Urosevic *et al.* 1995).

To achieve a more accurate velocity field during the PRA processing an interactive velocity analysis was carried out in the second iteration of velocity analysis. However, high quality velocity picking using the relatively precise semblance analysis technique requires an adequate signal-to-noise ratio to be effective. A way of enhancing the signal-to-noise ratio is to create supergathers by collecting traces from adjacent CMPs and stacking the traces with similar offset or angle range. CMP supergathers were first created for the Semblana sub-dataset by combining five inlines and crosslines for every tenth inline and crossline position. Following this, an iterative interactive velocity analysis was carried out on CMP supergathers using the CVS velocity field as a guide function. Figure 4.8 shows the velocity spectrum with

the velocity picks associated with primary reflections. A manual NMO top mute was additionally picked and applied to mute the wavelet distortion that occurs particularly for shallow events at large offsets.

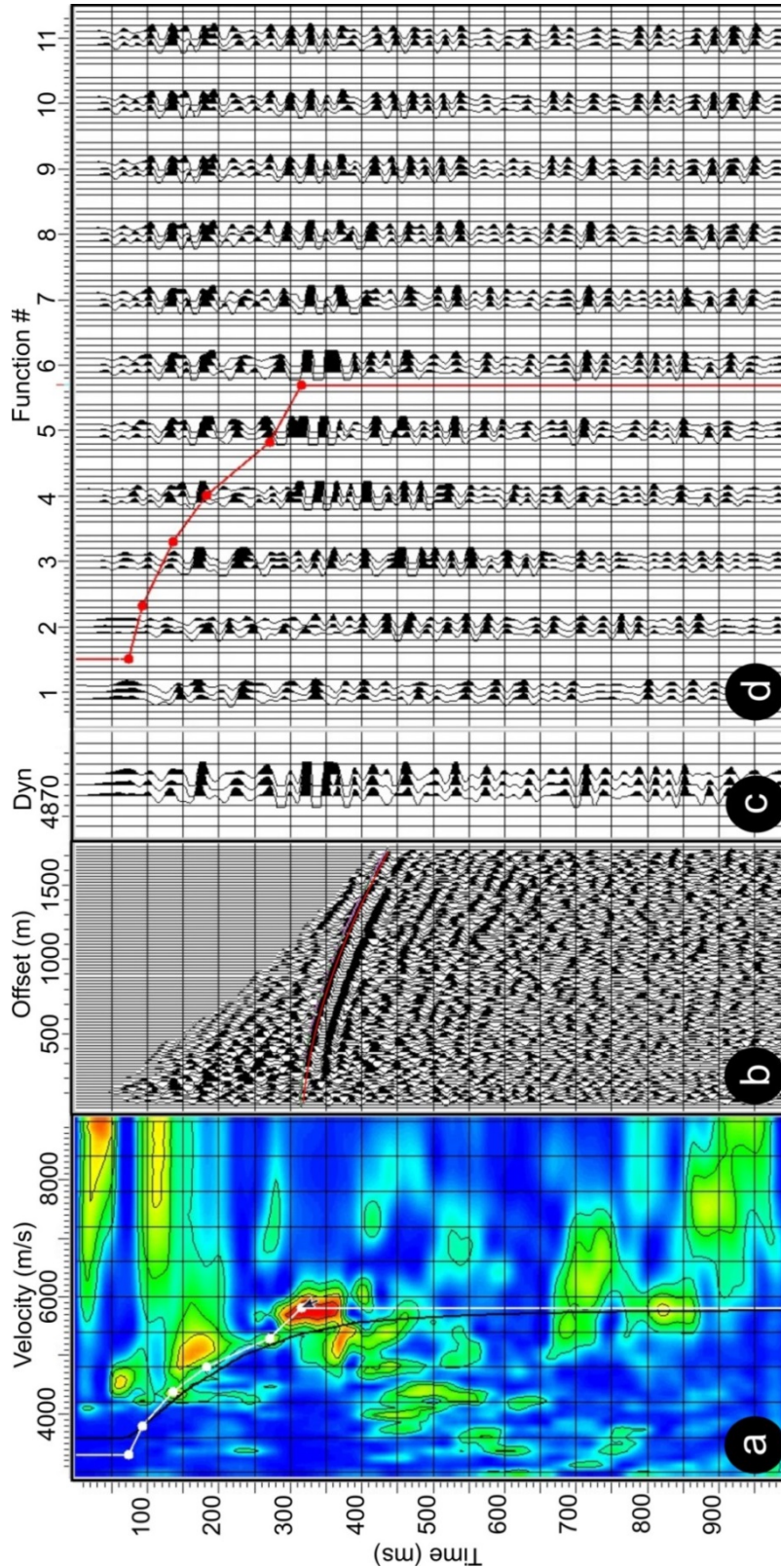


Figure 4.8 Interactive velocity analysis. **a)** A velocity spectrum (semblance panel) is plotted with warm colours indicating greater signal coherence. The CVS velocity guide function (black curve) and the picked stacking velocity function (white curve) are also displayed over the velocity spectrum. **b)** A CMP gather with the superimposed hyperbolic travel time trajectory (red curve) overlain on the Semblance reflection. **c)** Dynamic stack panel and **d)** constant velocity stack panels are also used as a quality control of the picked function. The red points connected with a red line indicate the picked velocity function and correspond to the white points connected with a white line on panel **a**.

4.3.6 Pre-stack Kirchhoff 3D Time Migration

Seismic migration is one of the most important steps in seismic processing. It aims to geometrically reposition a seismic event from the location it was recorded from to their true location in the subsurface (Sheriff and Geldart 1995). As such any migration as the inverse process naturally leads to depth images. However our generally poor control of the velocities makes depth imaging less desirable particularly for hard rock seismic. Hence it is usually performed in time domain as the time domain imaging is far more robust than depth imaging. The images obtained by PSTM are not necessary exact but are continuous and much more precise than images produced by a conventional DMO plus post-stack migration. PSTM algorithm has the ability to migrate steeply dipping reflectors to their true or very close to the true subsurface position and to collapse diffractions (Yilmaz 2001).

A combination of DMO and post-stack migration is one of the most robust methods commonly used in seismic imaging. However, carefully executed pre-stack time migration will in general better focus events and place them in their true “time” domain position. In this study, a pre-stack Kirchhoff 3D time migration was executed using the parameters defined in Table 4.3 in order to test the value of it in seismically characterizing VMS deposits.

The first and the most important step in the PSTM application was to produce and analyse impulse response in order to determine optimum migration parameters such as aperture, maximum offset and layer dip. . For this purpose, CDPs from 6091 to 6093 (Figure 4.6) were chosen to test these two parameters as the Semblana reflection was most obvious here. The a priori knowledge of depth and dip information about the Semblana orebody was also included in the analysis of the impulse response. A maximum of a 1000 m aperture limit and 40° of dipping angle was determined through these tests as seen in Figure 4.9.

F-XY deconvolution is a multi-dimensional frequency domain deconvolution that is used to filter the traces and reduce random noise. It works by applying a Fourier Transform in order to improve reflection character consistency and to reduce the unwanted attenuation of steeply dipping events such as fault plane reflections (Chase 1992). After the application of PSTM, a post-stack F-XY deconvolution was applied

to the data. The final PRA seismic cube was converted to the depth domain using the vertical seismic profiling (VSP) velocities obtained from drillhole PSJ-50 (Figure 3.9), with velocities ranging from 3500 to 6000 m/s.

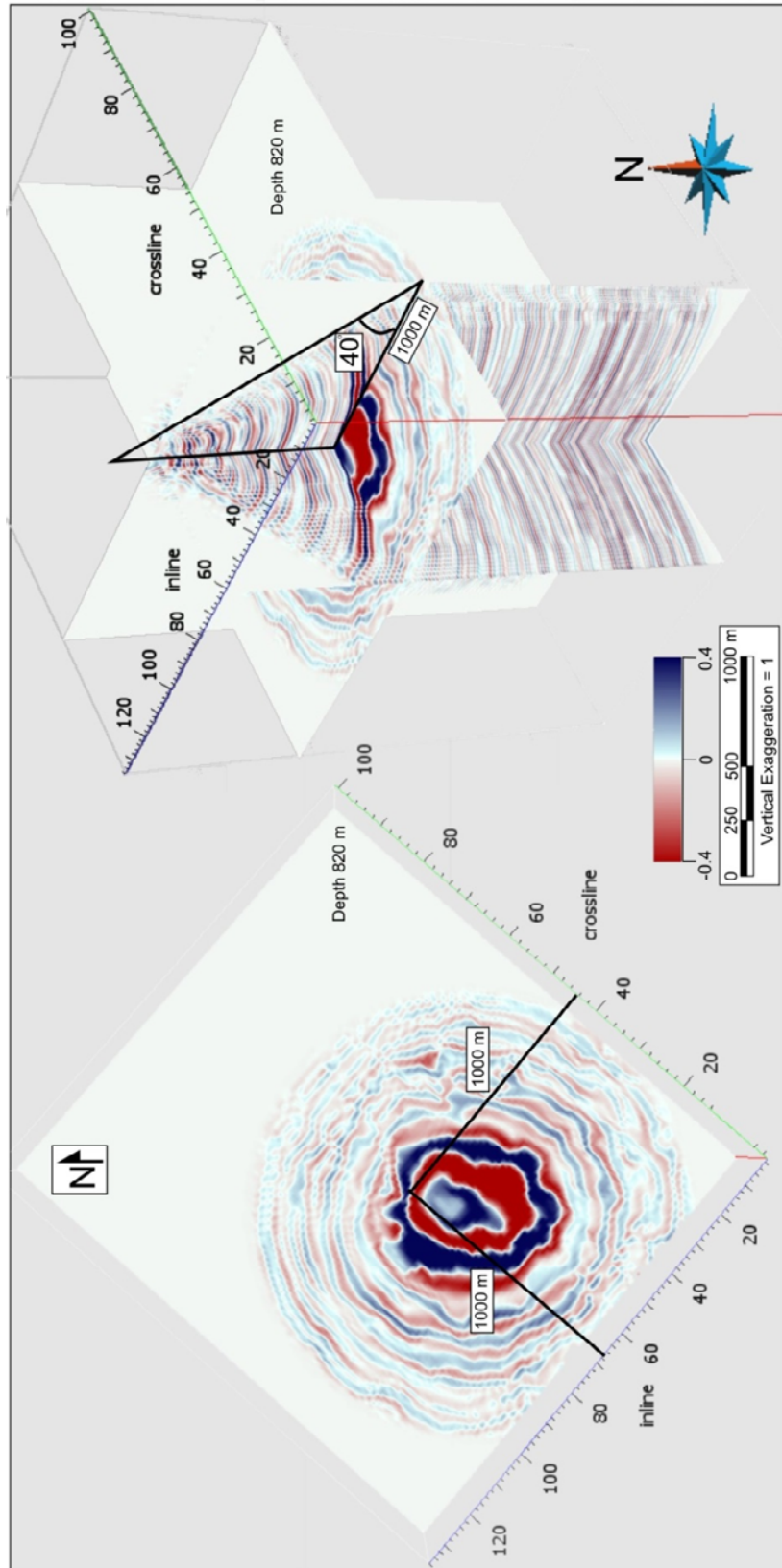


Figure 4.9 Impulse response test for the determination of migration aperture and dip angle (right). The depth slice for the Semblana orebody is displayed on the left. The maximum migration aperture required was found to be 1000 m with a maximum dipping angle of 40° .

4.4 Volumetric Interpretation

After the application of the fully preserved relative amplitude processing followed by PSTM, the results were investigated in cross-section and time slice domains. Several inline and crossline sections and depth slices are selected to assess the results as illustrated in Figure 4.10 and Figure 4.11. A significant improvement in the quality of the Semblana reflector was observed on the selected sections and depth slices.

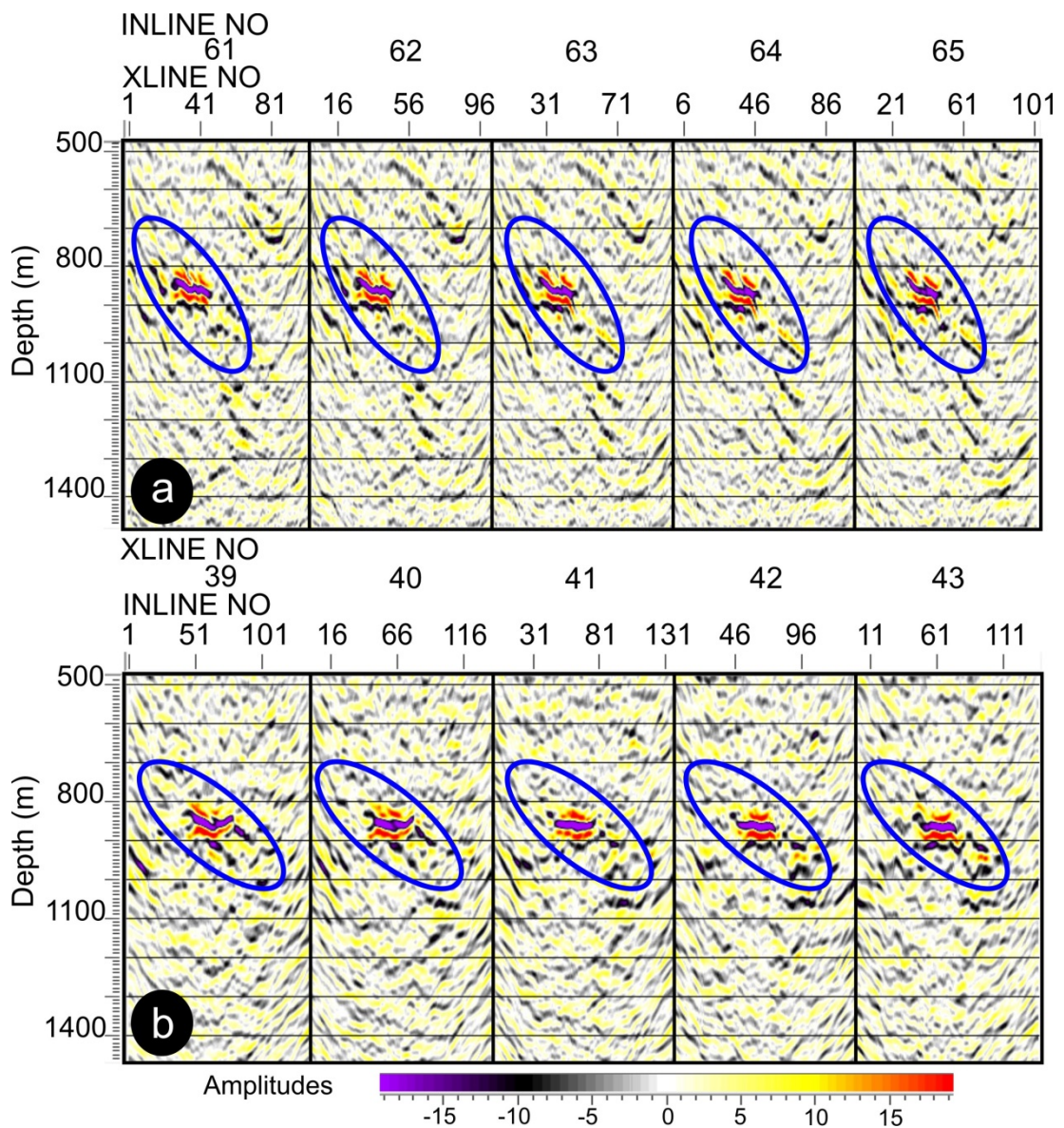


Figure 4.10 PRA processed Semblana sub-dataset with selected a) inlines and b) crosslines displayed. The Semblana orebody is indicated with a blue ellipse.

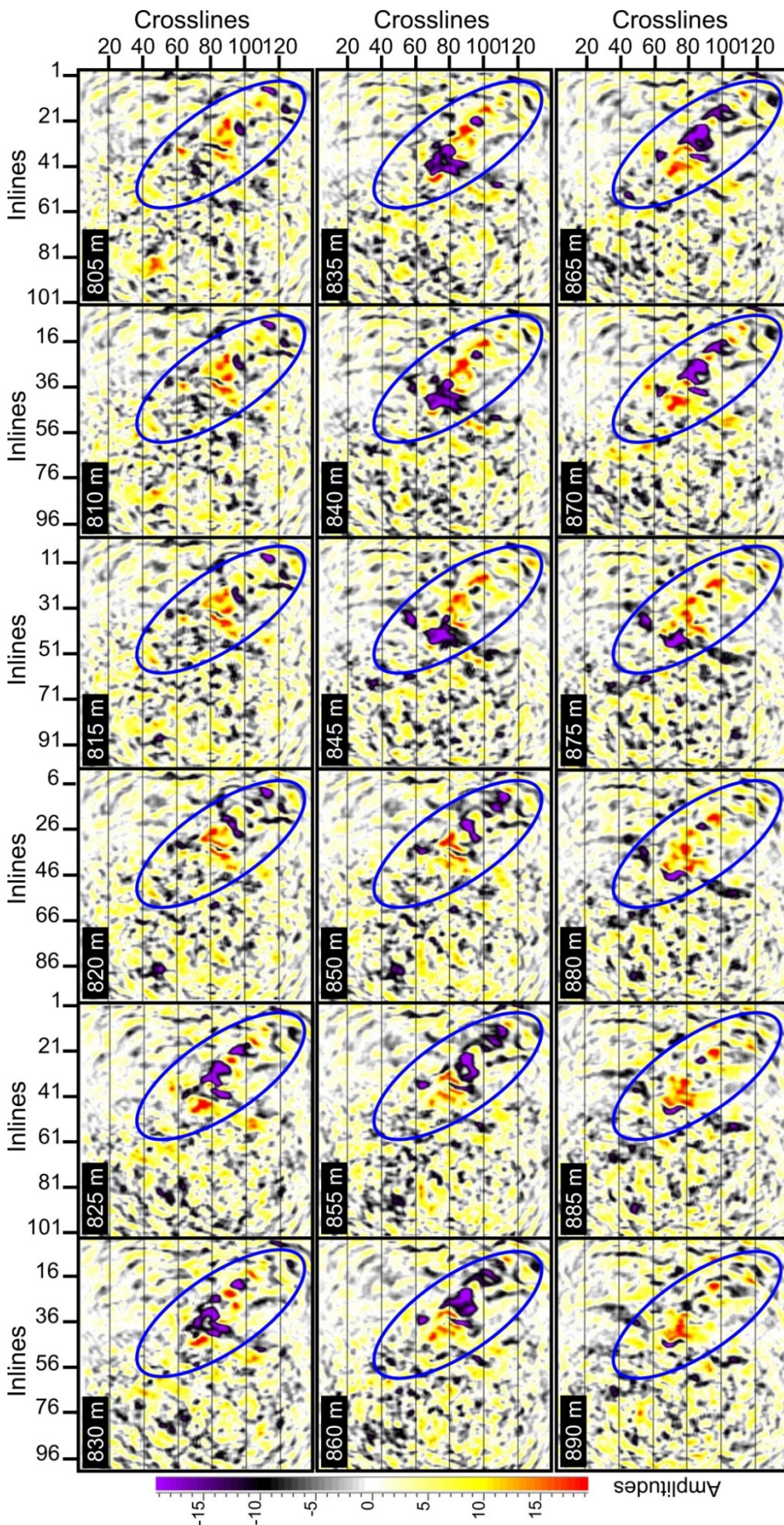


Figure 4.11 PRA processed Semblana sub-dataset with depth slices from 800 to 895m displayed. The Semblana orebody is indicated with a blue ellipse.

Following this, the new Semblana cube as well as the AGC cube was imported into GOCAD to compare the PRA and AGC processing results (Figure 4.12) and to carry out a volumetric style of interpretation. This also included existing geological information such as marker horizons, the mineralization wireframe and selected drillholes. As expected, the strongest reflection in the PRA seismic cube coincided exactly with the Semblana orebody and it matched the mineralization wireframe without any error. This wireframe was provided by Lundin Mining Corporation and was created based on drilling intersections. Additionally, a good match between the CULM and Neves Corvo Thrust wireframes provided by Lundin Mining Corporation with continuous seismic reflectors was also observed in Figure 4.12.

Original high priority target wireframes that were previously interpreted based on the 2011 AGC cube and were subsequently drilled and found to be rhyolites were imported into the volumetric interpretation database. As mentioned in section 3.4, elastic property measurements followed by drillhole data calibration proved that these mis-targeted rhyolites should not provide a high amplitude response (Figure 3.10b). When these targets were reviewed against the PRA cube in GOCAD, the previously observed high amplitudes from the AGC dataset was found to no longer be the case in the PRA dataset. This review clearly showed that they would not have passed the targeting criteria had the PRA processing flow been adapted in the original processing based on their low reflectivity (Figure 4.13).

In order to inspect the PRA cube as well as these targets in detail, amplitude-based geobodies (iso-shells) were produced using the envelopes of the normalized amplitudes both for the AGC cube and the PRA cube within a threshold (Figure 4.14). This facilitated a qualitative comparison of high amplitude anomalies between the two cubes. In order to achieve the most reliable outcome, the elastic property variations of massive sulfide, stockworks and the other main lithological units (Figure 3.7 and 3.8) were considered. The amplitude envelope histograms were analysed in conjunction with Figure 3.7 to determine the optimum threshold for iso-shell generation and are shown in the bottom left corner of each cube in Figure 4.14. The iso-shell generation was based on a high-pass cut-off calculated for each cube separately (0.35 - 1 for the AGC cube and 0.25 - 1 for the PRA cube). It was noted that zero values were observed in the amplitude histogram for the AGC cube (Figure 4.14), which belong to empty traces that were assigned to fill gaps in acquisition that

did not exist in the reprocessed subset and these values were discarded in the iso-shell generation. The improved zonation of the targeting using the PRA data was verified through the generation of iso-shells.

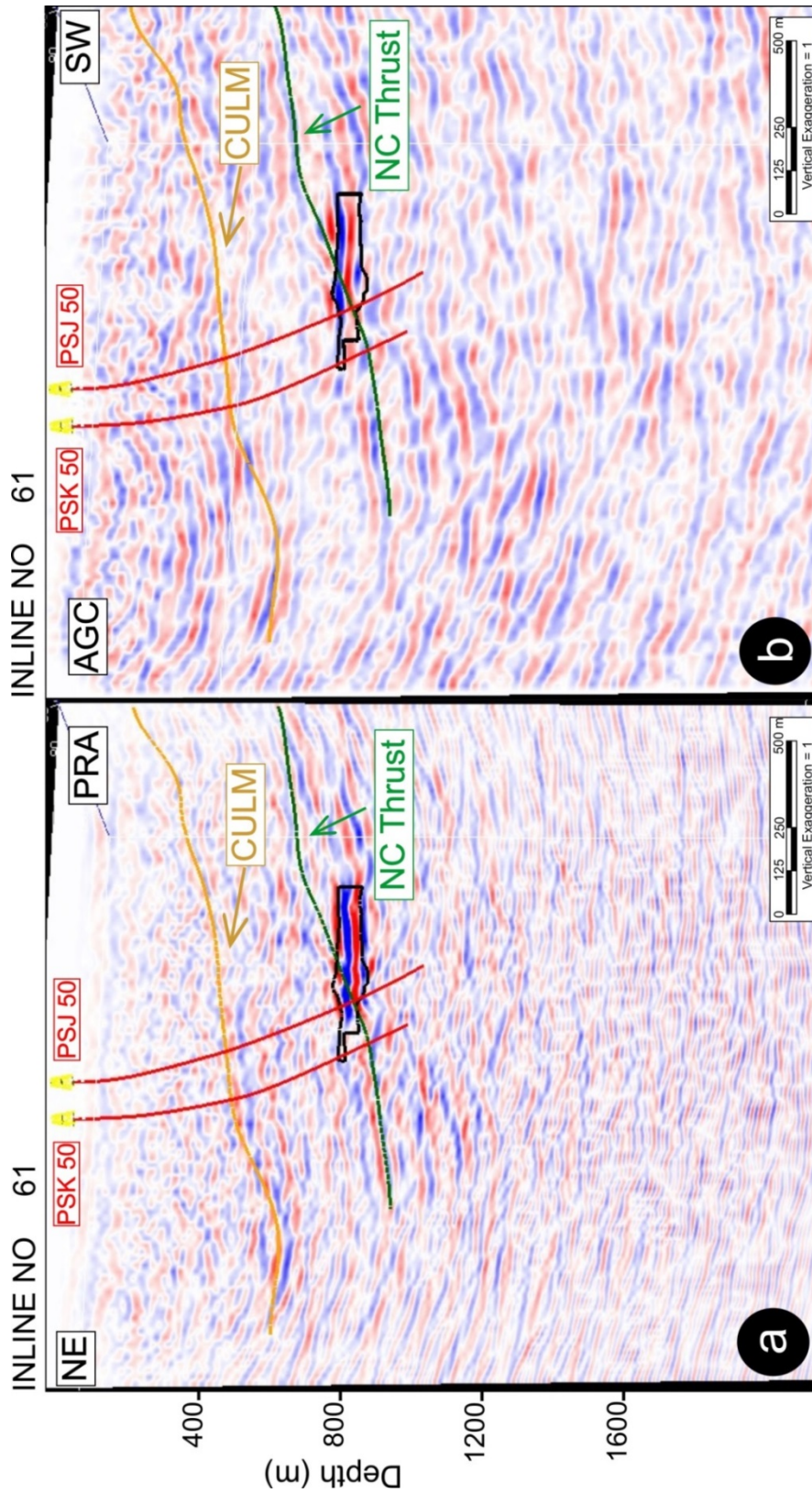


Figure 4.12 Comparison of **a)** PRA and **b)** AGC processing results on selected inlines. PSJ50 and PSK50 are overlain together with the wireframes for the Semblana copper sulfide mineralization (black outline), Neves Corvo Thrust (green) and CULM (yellow).

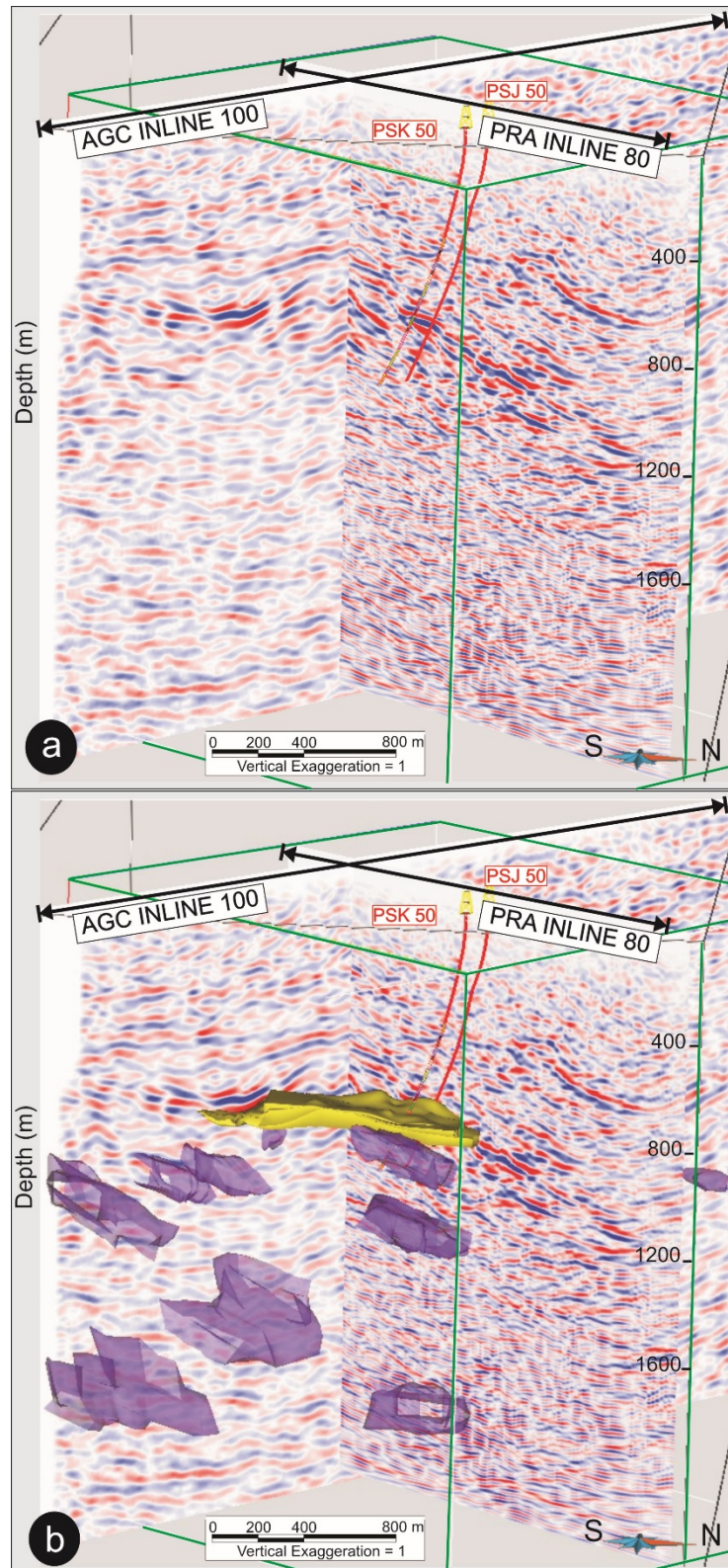


Figure 4.13 a) 3D view of the intersection of orthogonal sections of the PRA (SE – NW) and AGC (SW-NE) processed cubes and b) with superimposed wireframes. The PRA cube borders (green), PSJ50 and PSK50 trajectories (red) and the Semblana wireframe (yellow) are displayed. Anomalous amplitude zones (purple) identified from the AGC data were scrutinized and to a great extent rejected after cross checking against the PRA data.

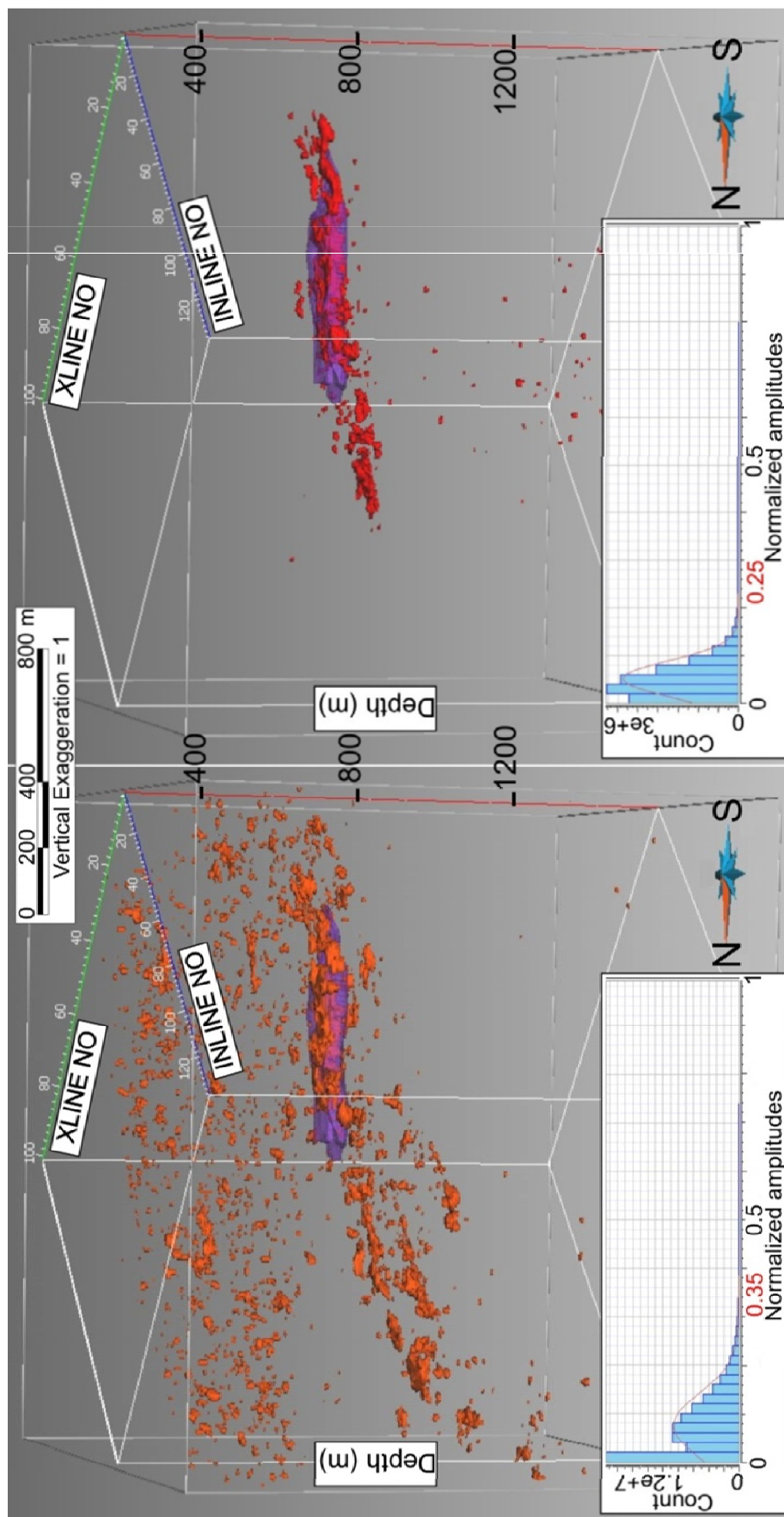


Figure 4.14 Comparison of AGC and PRA approaches through the generation of iso-shells. The iso-shells for the AGC cube (colored orange on the left) and PRA cube (colored red on the right) are overlain on the Semblana wireframe (purple). The amplitude envelope histograms are shown in the bottom left corner of each cube. The optimum threshold values for iso-shell generation (red) are also shown on each graph.

4.5 Discussions and Conclusions

In order better characterise Semblana orebody, Semblana sub-dataset was reprocessed using a PRA approach including the surface consistency principle and imaged with PSTM. High quality image obtained enables precise orebody oriented interpretation.

Signal-to-noise ratio analyses were the first important step in PRA processing since this approach is significantly more sensitive to noise. As more precise data conditioning was required through an iterative editing, killing and muting cycle, this could be less time effective in a commercial environment. Hence, the automatic noise analyses helped considerably data conditioning stage.

The next significant step was to recover and compensate the amplitudes of the traces in a surface-consistent manner. This was aided with a temporary surface wave noise attenuation application. Finally, a surface-consistent deconvolution was used to enhance primaries in an unbiased way.

One of the most challenging steps was the removal of ground roll and other coherent noise. The successful application of a Radon filter was not just used to assist the PRA processing by eliminating coherent noise, but also aided the preserved amplitude processing through an improved estimate of the scalars representing source and receiver coupling, respectively.

The next key processing step was the application of a surface-consistent residual static correction. This step considerably improved the strength and continuity of the reflection associated with the Semblana orebody.

CVS velocity analysis provided a realistic velocity field for the initial PRA reprocessing that was subsequently improved by interactive velocity analysis applied on CMP supergathers.

Careful application of Kirchhoff 3D pre-stack time migration was of a great importance for subsequent interpretation. Very good results were obtained after careful analysis of 3D impulse response. This enabled optimal parameterising and subsequent successful run of PSTM.

A comparison of the PRA and AGC cubes against marker horizons, mineralization wireframe and selected drillholes showed unambiguously that the strongest reflection in the PRA seismic cube was associated with the Semblana mineralisation as the seismic amplitude anomaly completely matched the mineralization wireframe.

The reinspection of high priority targets on the PRA cube provided one of the most important results of the PRA processing. The preserved amplitude approach succeeded in providing a resolution to the amplitude non uniqueness enigma of the AGC dataset. The amplitude responses of these original targets were reconsidered based on the reprocessed data. As was demonstrated in section 3.4, the elastic property measurements showed that the amplitude responses of these targets were too weak to be considered as originating from an interface with massive sulphides. This was consistent with subsequent drill testing, which did not intersect any massive sulphide.

A volumetric interpretation of the PRA reprocessed seismic cube was performed with the use of iso-shells, thus improving the zonation of the target. It was shown that only the Semblana orebody generated a bright reflection and that only this event could be considered an economic target.

Another by-product of the PRA reprocessing was the ability to retain the broadest possible frequency spectrum in the data through the carefully selected processing sequence, especially during noise removal. The surface-consistent spike deconvolution followed by a wide-bandpass filter also helped to preserve spectrum signal bandwidth. The resolution of the seismic volume was found to be improved as a result of the application of PRA and PSTM.

The final PRA processed seismic volume is considered superior to the AGC processed volume. This is based on a very good agreement between the known spatial distribution of the Semblana orebody from drilling and the spatial distribution of high amplitude reflections within the PRA dataset. An improved agreement between wireframes based on drilling and the seismically mapped marker horizons (Neves Corvo thrust and CULM) were also achieved in the PRA dataset in comparison to the previously processed AGC cube.

Chapter 5

Seismic Characterization of the Semblana Orebody

This chapter describes the methodologies used for an improved characterisation of the Semblana orebody. This included model based acoustic and elastic inversions as well as AVO analysis. The main reason for the application of these techniques was to discriminate the massive sulfide from the stockwork as well as other rock units. It was also important to evaluate the applicability of the inversion techniques for the direct targeting of massive orebodies.

The first section of this chapter investigates the post-stack acoustic impedance inversion and its value for rock type identification within the recovered impedance cube. AVO analysis was subsequently performed on the pre-stack seismic data to derive the AVO attributes and combine this information with the acoustic impedance cube. An elastic inversion was then performed using the near-offset and far-offset stacks in order to further discriminate massive sulfides from the non-economical rock formations.

5.1 Acoustic Impedance Inversion

Acoustic impedance inversion is commonly used in soft rock seismic exploration. It is based on the convolutional seismic model where a seismic trace results from the

convolution of the reflectivity series with the source wavelet. The reflectivity series itself is related to the difference of the acoustic impedances across various rock contacts. Hence, it is obtained by the differentiation of the “impedance log”, which is the product of velocity and density. The impedance is what the inverse operation aims to recover from the seismic data after deconvolving the wavelet and integration of the resultant reflectivity series. This process is straightforward in sedimentary rocks as long as the initial conditions are met by the log data (correlation of seismic to logs or a so-called well tie). The impedance volume can be used to estimate variations in the rock elasticity or simply the rock properties away from drillhole control. The inversion process improves the resolution and better states the interpretability of seismic data by removing the source wavelet (Russel 1988). In sedimentary or soft rocks the acoustic impedance is directly related to the porosity. As previously discussed in the chapter regarding elastic property measurements, due to significant deformation and metamorphism crystalline rocks have very low porosity values. Therefore, the conventional meaning of acoustic impedance is less obvious in hard rock seismic data. A new reason for looking into the acoustic impedances of hard rocks is to help discriminate different rock types and possibly rock alterations.

However the inversion process is inherently non-unique. This is less pronounced if several calibration points (logs) can be utilised in the process of inversion. In such case the number of possible geological models consistent with the seismic data, which is common for all inversion algorithms is reduced and the process becomes more trustworthy (Oldenburg *et al.* 1983). Of particular interest to this study is the use of the model based acoustic impedance inversion as this process can produce reliable results if calibration points exist and seismic data is of a high quality. The datasets required as input into a model based acoustic inversion consists of a post-stack seismic data volume, drillhole data containing FWS and density logs, check shot logs, collar logs and deviation logs and lithological data containing formation markers and interpreted horizons.

A model based acoustic inversion is carried out in several steps. The first step in acoustic inversion was to create a log database. The next step was to import 3D seismic data (PSTM PRA cube) and establish a drillhole-to-seismic tie that correlated this data to the drillhole derived synthetic seismograms after the source wavelet has

been extracted from the seismic cube. An initial impedance model was then created from the logs and interpreted horizons or in the hard rock case “interfaces”. After scaling the model and the seismic, the inversion could then be performed with the tested parameters. This step is commonly known as inversion analysis. During the inversion analysis, the initial model was constrained with the input data to control how far the final result may deviate from the known values derived from the logs.

5.1.1 Database Creation and Correlation

The first two steps required to carry out a model based acoustic inversion are to gather the necessary inputs into a database and to convert drillhole depths to time. A comprehensive database was already created in section 3.2. The data sets selected from this database to use in the model based acoustic inversion are listed as below;

- From drillhole PSJ50; FWS logs, bulk density log, check shot data (zero-offset VSP), lithological data containing formation markers.
- From drillhole PSK50, PSK48 and PSO 44, pseudo logs containing P-wave, S-wave and density logs, lithological data containing formation markers.
- From drillhole PSN42; FWS logs, check shot data, lithological data containing formation markers.

Drillhole SZ24, which was used in modelling the seismic response of rhyolites, was left out of the inversion since its location was not in the PRA processed cube.

The drillhole-to-seismic ties were already completed in section 3.3 in order to perform the modelling of the seismic response of massive sulfide, stockworks and rhyolites. The correlation coefficients for the drillhole-to-seismic tie from drillhole PSJ50, PSK50, PSK48 and PSO44 were 73%, 87%, 78%, and 83% respectively. Since drillhole PSN42 did not include any density logs, it provided a low correlation coefficient in the calibration that was considered unsatisfactory. Hence, it was only used as a control drillhole with the P and S-wave logs used during the crosschecking of the inversion results.

The work completed in section 3.2 and 3.3 allowed the model based acoustic inversion to enjoy a head start. In order to proceed with the velocity model building, the last step was to include the interpreted horizons. As mentioned in subsection

3.1.4, the CULM provides an excellent marker horizon within the study area to separate the two major stratigraphic packages - the Mertola formation and the volcanic sedimentary complex. The Neves Corvo thrust was the other important marker horizon, which is one of the most important indicators of the prospective zone. These two marker horizons were originally extracted solely from drillhole data and were then imported into the inversion database. Depth-to-time conversion of these two marker horizons was achieved using the velocity derived from zero-offset VSP data measured in drillhole PSJ50. The horizons were then slightly modified and improved in between drillholes by tracing them in the post-stack data volume (Figure 5.2). Figure 5.1 shows a base map and a seismic section overlapping with some drillholes.

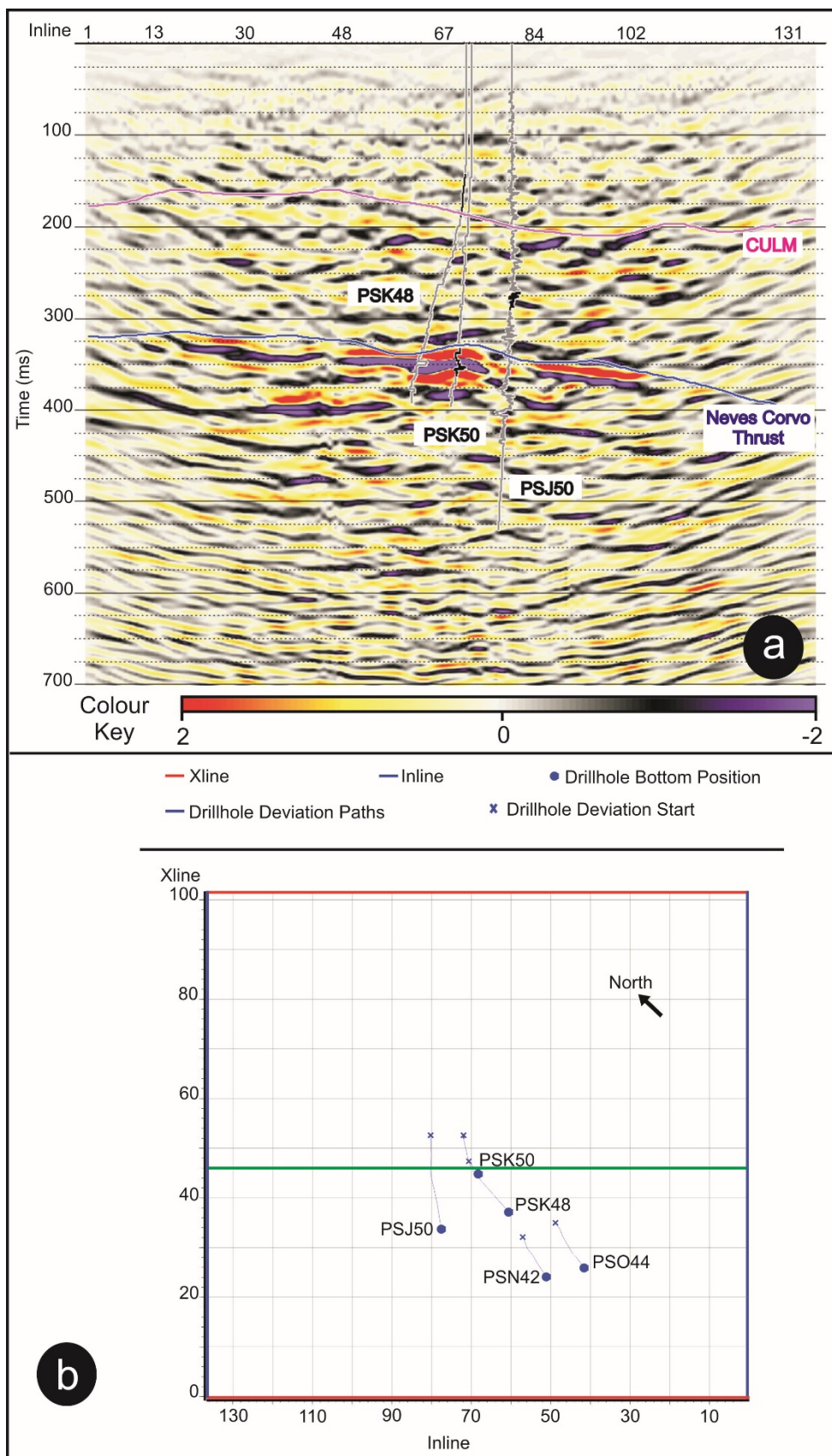


Figure 5.1 a) The seismic section for crossline 46 and b) its location in green on the base map. Some drillholes and the marker horizons are illustrated on the seismic section. All drillholes and their paths are illustrated on the base map.

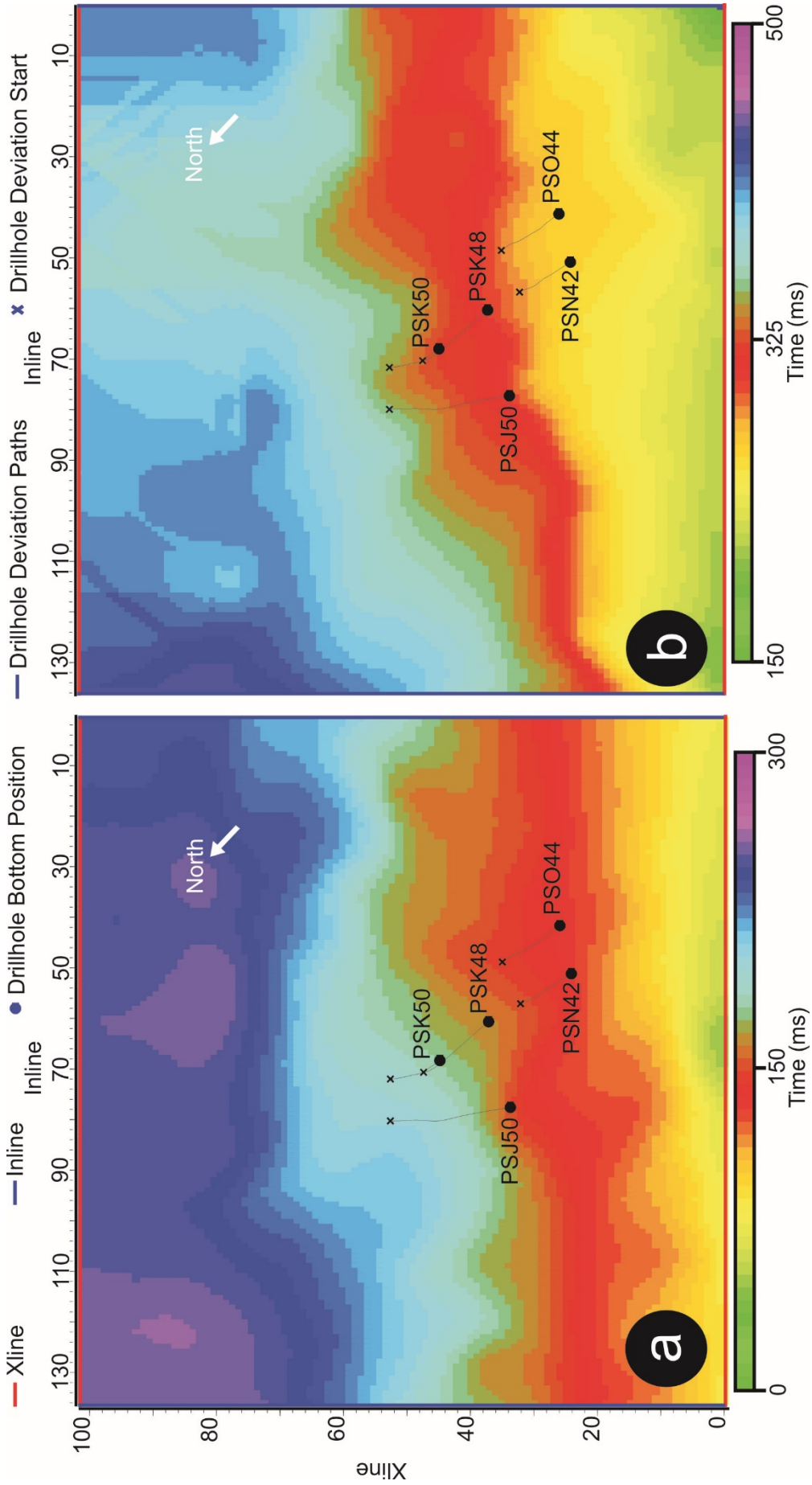


Figure 5.2 The interpolated time slices for the a) CULM and b) Neves Corvo thrust marker horizons.

5.1.2 Model Building

Building an initial model was the next step required for model based acoustic inversion. The seismic data itself does not contain the low frequencies required to recover the absolute impedance values from the inversion (Russel 1988). Therefore, the objective was to build a low frequency velocity model using the drillhole logs and horizons to introduce the lower frequencies that could only be provided by drillhole data. Alternatively stacking velocities can be used for the same purpose.

Four different drillholes were used to build the model and the results were then interpolated using an inverse-distance weighting algorithm. A P-impedance model cube was then obtained through the extrapolation of the drillhole data along the marker horizons, which caused the impedances between the horizons to be stretched and squeezed as required to fit this data. Due to this concept, it should be noted that a model based inversion mostly gives successful results in less complex geologies that consist of horizontal layers with gentle faulting. The Semblana orebody can be considered an irregularly shaped three dimensional geobody. Along with the Neves Corvo thrust and other minor faulting around the Semblana orebody the geology in the study area can be regarded as moderately complex.

Figure 5.3 illustrates the initial P-wave velocity and density model cubes. As expected, the high P-wave velocity and density values assigned to the Semblana orebody were interpolated away from its position as a part of process. The same effect was also seen on the initial P-impedance cube and the synthetic seismic cube that was created through the convolution of the p-impedance cube and the source wavelet (Figure 5.4). To address this, we considered weighting the calculation more towards the seismic data in order to more accurately represent the extents of the orebody. The initial models were constrained to recover data in the 10 to 30 Hz frequency range.

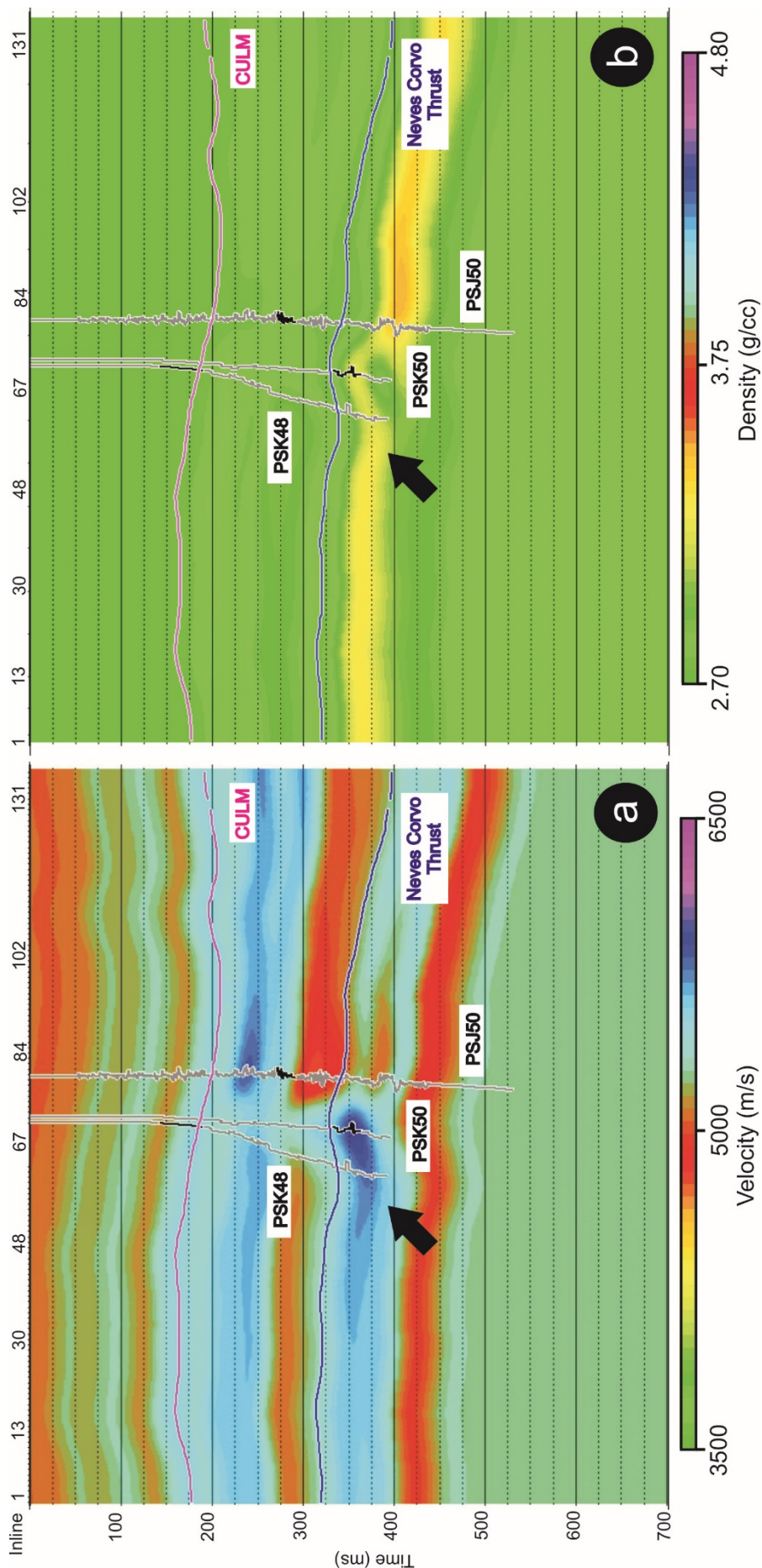


Figure 5.3 a) The initial P-wave velocity and **b)** density model cubes for crossline 46. Pseudo logs of PSK48 and PSK50 and FWS log of PSJ50 were displayed with Neves Corvo thrust and CULM. Black arrows point out the location of the Semblana orebody.

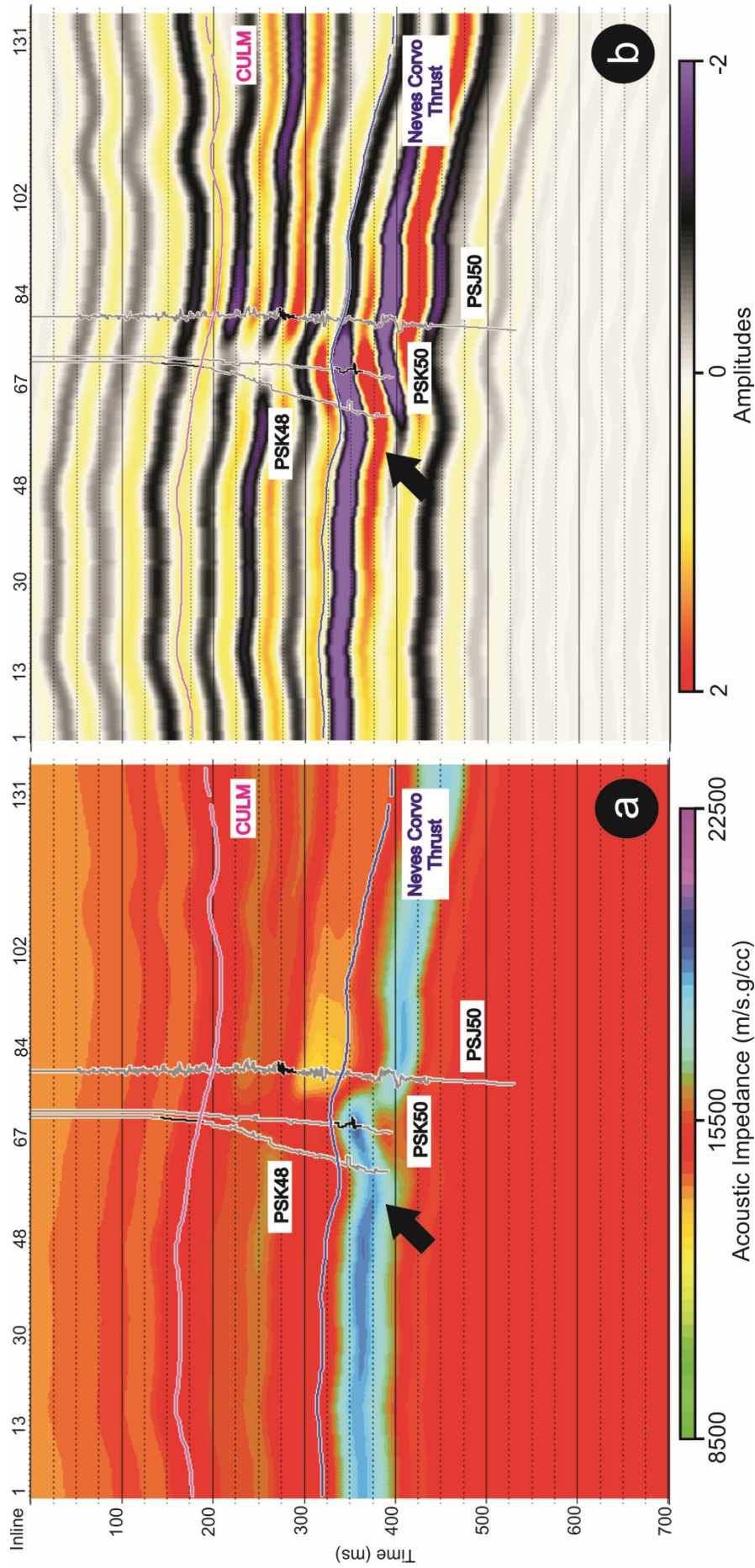


Figure 5.4 a) The initial P-impedance model and **b)** synthetic seismic cubes for crossline 46. Pseudo logs of PSK48 and PSK50 and FWS log of PSJ50 were displayed with the Neves Corvo thrust and CULM. Black arrows point out the location of the Semblana orebody.

5.1.3 Inversion Analysis

Parameter testing, or error analysis, of the input parameters for the inversion was conducted to arrive at the lowest error coefficient. This analysis was performed for each drillhole and was used to constrain the inversion. Correlation coefficients and RMS errors quantitatively represent the quality of the correlation between two traces. The first one is the synthetic seismic trace that was originally created from drillhole logs and previously calibrated with seismic data. The second one is the resultant seismic trace along the corresponding drillhole trajectory that was created using both model and seismic data for the tested parameters. The number of iterations, scaling factor, constraint type and the minimum and maximum acoustic impedance change were the most important parameters that were tested in the inversion analysis. The choice of these parameters was based on obtaining the least amount of error during the correlation process. An example of the error analysis conducted for drillhole PSJ50 is illustrated in Figure 5.5. The correlation coefficients achieved for drillhole's PSJ50, PSK50, PSK48 and PSO44 were 0.963, 0.976, 0.927 and 0.976, respectively.

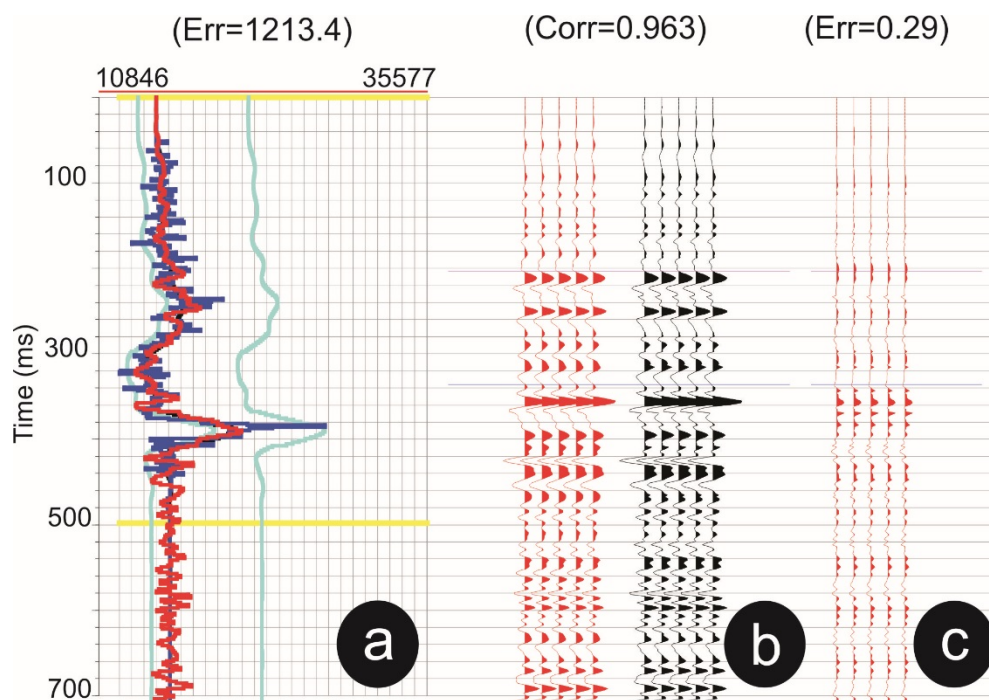


Figure 5.5 The error analysis for drillhole PSJ50. **a)** The seismic trace extracted through the drillhole trajectory (dark blue) and the synthetic seismic trace after inversion (red) are displayed in between the light blue constraints with the window for the error calculation shown in yellow. **b)** The synthetic and seismic traces that were used to calculate the correlation coefficient and **c)** the error represented as traces.

5.1.4 Inversion and Interpretation

After successfully constraining the parameters through an error analysis, a model based acoustic inversion was performed. Due to the complex geology in the study area and the relatively low resolution of the Semblana seismic dataset, it was decided to apply hard constraints in inversion. The decision to apply a ‘hard constraint’ inversion was made to keep the final impedance values within the specified percentage limits which would eventually lower the error that can be caused for this reason. In elastic property measurement the acoustic impedance changes for the main lithologies were already well defined. The highest acoustic impedance change was observed around the Semblana mineralization, providing approximately two times higher acoustic impedances than the host rock. Considering this, the minimum and maximum bounds for the acoustic impedance change were chosen as 10% and 40% which correspond to a maximum reflectivity of 0.3, respectively.

Fifty iterations were run to allow the algorithm to converge towards the most appropriate solution and it was scaled by putting more weight towards the seismic data for reasons discussed in subsection 5.1.2. The seismic energy losses due to transmission and geometric spreading are two important factors that have to be considered during an inversion. To a great extent, these losses were compensated for in the PRA processing. Hence, it is important to note that no additional corrections were made for these factors during the inversion.

The results of the created impedance cube were then analysed. Figure 5.6 shows an inverted inline and crossline extracted from the acoustic cube where the Semblana orebody has resulted in a significant acoustic impedance change as expected. However, due to the framework of inversion, the interpolation of the drillholes along the horizons has produced high acoustic impedance values within the zone around the Semblana orebody as well. This situation was taken into consideration during the investigation of the acoustic impedance cube.

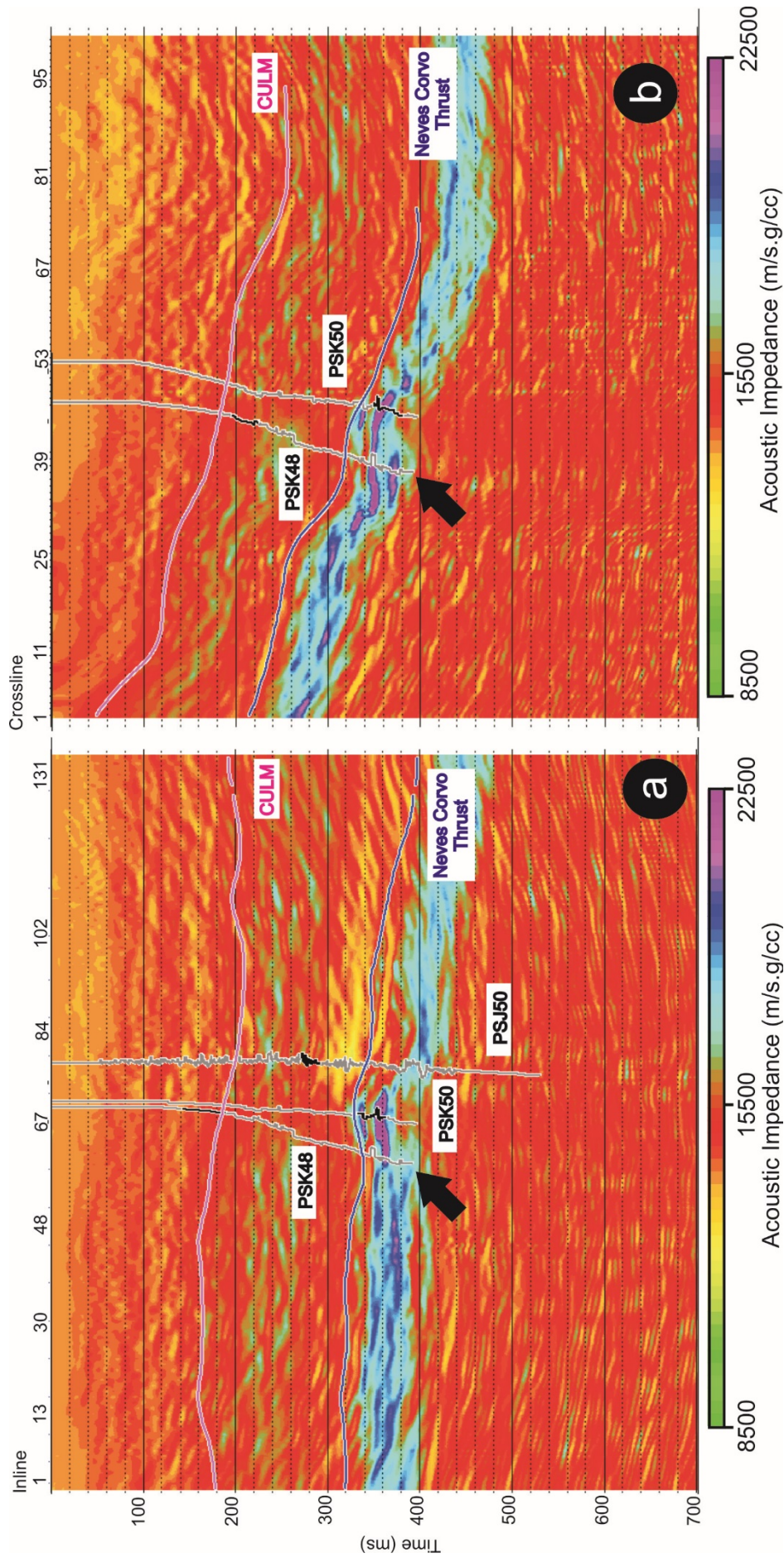


Figure 5.6 The acoustic impedance inversion results on a) crossline 46 and b) inline 69. Pseudo logs of PSK48 and PSK50 and FWS log of PSJ50 were displayed with Neves Corvo thrust and CULM. Black arrows point out the location of the Semblana orebody.

5.2 AVO Analysis

Amplitude versus offset analysis is a technique used to analyse the amplitude dependency on the separation length between the source and receiver (offset) in seismic data. It can provide information on porosity, density and seismic velocity as well as other rock properties. In this study, AVO analysis was performed as a means to distinguish the reflectivity associated with massive sulfides from other rock units in contact that appear to give a similar amplitude.

AVO analysis was performed on the pre-stack data, which had already undergone preserved relative amplitude processing. The seismic data was acquired in the shot (source) and receiver domain. However, the majority of the seismic data processing was mostly done in the CDP domain and the final seismic cube was produced in what is referred to as the inline-crossline domain. Inline and crossline sections were constructed with CDPs, which consist of traces with similar mid points but varying offset being stacked together. AVO analysis utilizes the pre-stack CDP gathers.

The AVO analysis process was started by modifying the acoustic impedance inversion database. To begin with, the PRA 3D gathers were imported into this database. The first step of the analysis was to create CDP super gathers. CDP super gathers are the sum of adjacent CDP gathers, which are created to improve the signal-to-noise ratio and more importantly the continuity of the main reflector to analyse. The number of CDPs to sum into a super gather was decided based on the limitation of lateral resolution. The Fresnel zone defines the lateral resolution and tends to decrease approximately to the dominant wavelength after migration (Stolt and Benson 1986). The dominant frequency of the PRA data was found to be approximately 40 Hz and was used to calculate a lateral resolution width of 125 m for the depth of the Semblana mineralization zone.

The seismic cube consisted of 136 inlines and 101 crosslines constructed from 13736 CDPs. Because the crossline interval was 15 m and the inline interval was 22.5 m (Table 4.3), 7 inlines and 5 crosslines centred on the CDP for analysis were chosen to create a CDP super gather for 40 offsets. The 3D CDP supergather creation parameters are listed in Table 5.1. The creation of a simple 3D CDP super gather is illustrated in Figure 5.7 as an example.

Table 5.1 3D CDP supergather creation parameters.

Parameter	Value
First inline	1
Last inline	136
Inline increment	1
Inline ensemble size	7
First crossline	1
Last crossline	101
Crossline increment	1
Crossline ensemble size	5
Number of traces/Supergather	40
Offset range	10-1750 m

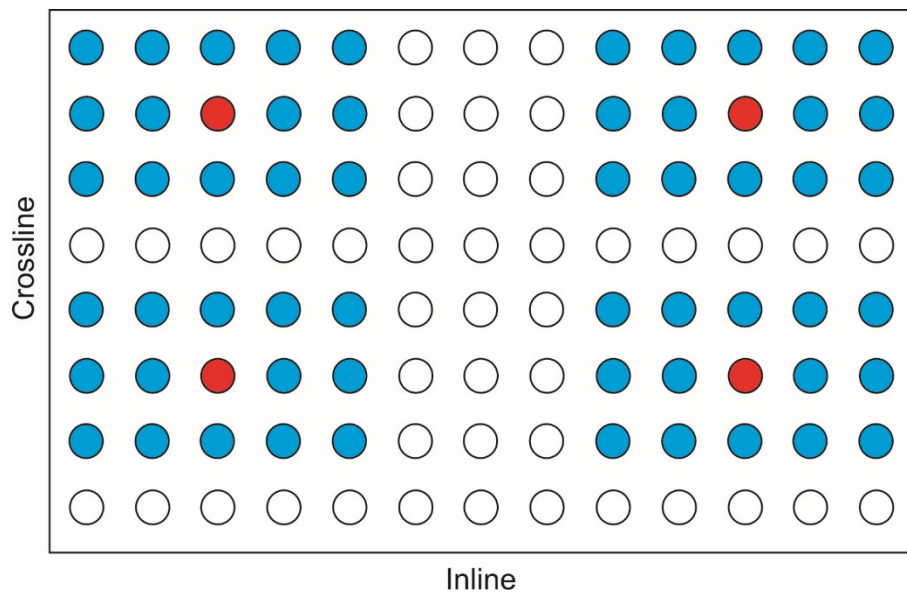


Figure 5.7 An example of how a 3D CDP supergather is created. First inline = 3, last inline = 13, inline increment = 8, inline ensemble size = 5 (blue circles), first crossline = 2, last crossline = 8, crossline increment = 4, crossline ensemble size 3 (blue). The number of 3D supergathers which are created with this design is 4 (red circles).

A zero offset modelling study was already completed in section 3.3 (Figure 3.10 and 3.11) for all drillholes, which provided a synthetic AVO response of the Semblana mineralization. After the creation of 3D CDP super gathers, the Semblana reflection

was investigated in the vicinity of boreholes. An example CDP supergather is shown in Figure 5.8. The offset range for the Semblana reflection was found to be 0-1250 m for this particular super gather. A new horizon was also picked for the Semblana reflection and was interpolated throughout the seismic cube and shown on Figure 5.8.

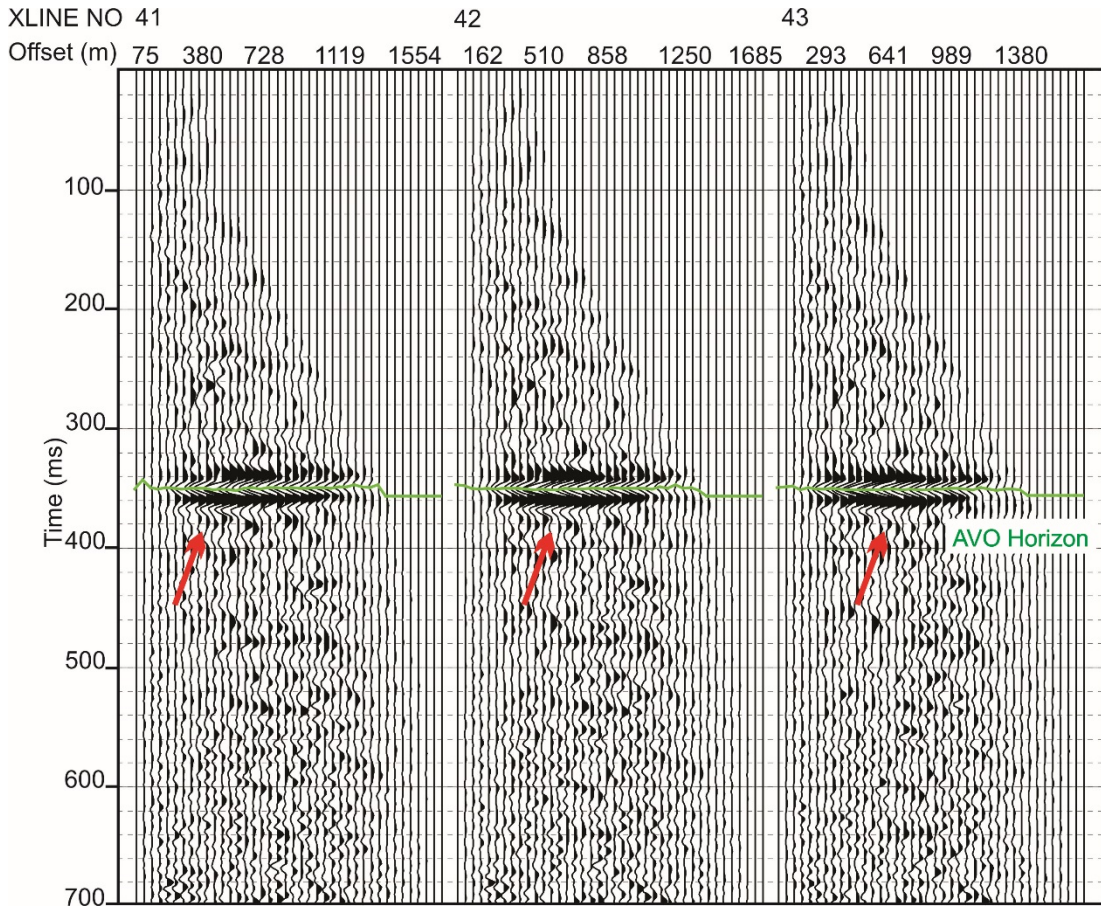


Figure 5.8 A CDP supergather example for inline 62. Semblana reflection is highlighted with red arrows.

The amplitude variation on a time slice from the PRA reprocessed seismic volume (Figure 5.9a) was analysed in order to define the exact limits of the reflectivity in the CDP supergather for the Semblana orebody. Figure 5.9b shows the RMS values of amplitude variation calculated for a 60 ms time window centred on the AVO horizon. This allowed us to see the location and distribution of the Semblana reflection for the interpretation of the following AVO attributes.

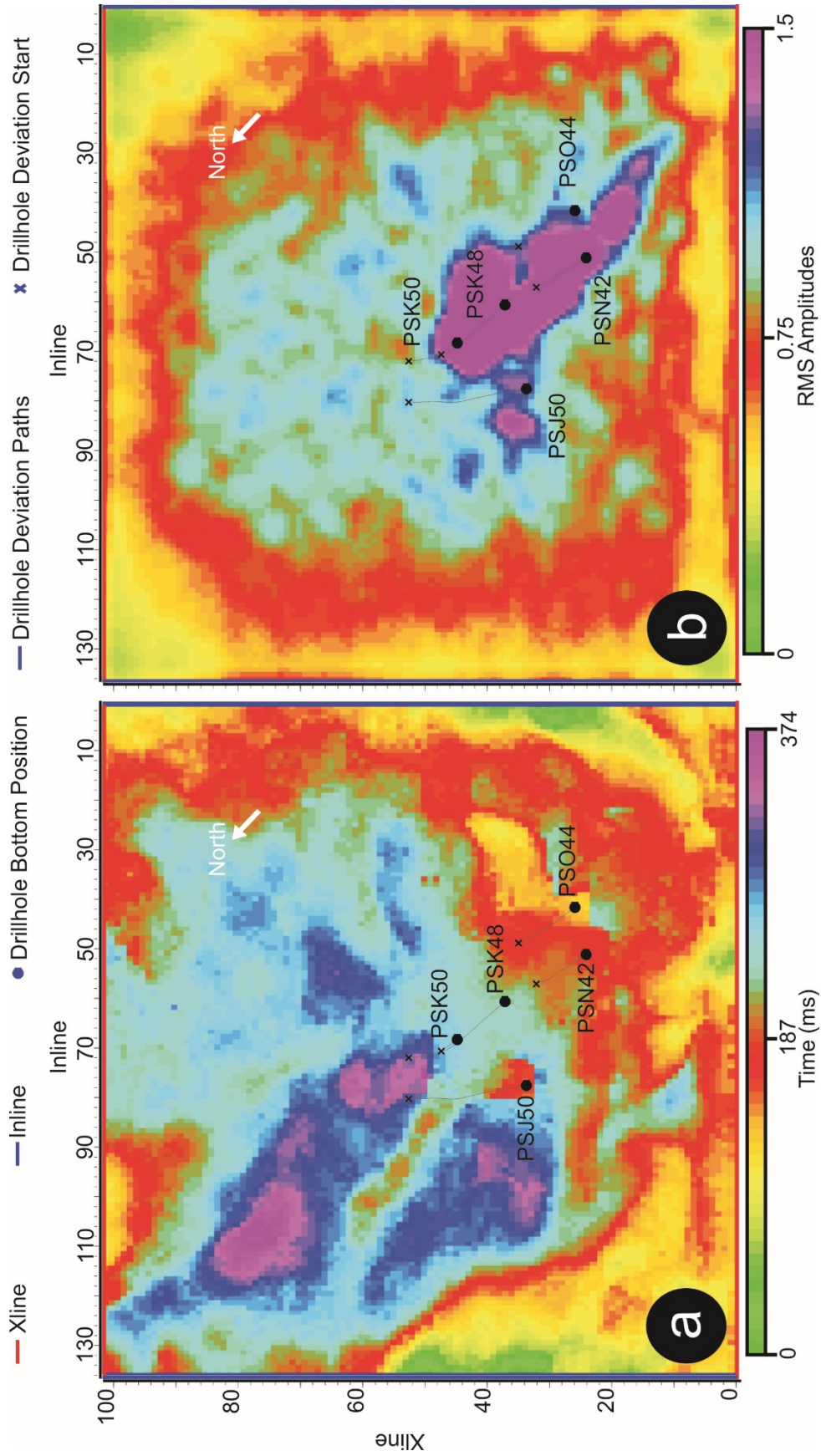


Figure 5.9 a) The interpolated time slice for the horizon corresponding to the Semblana orebody and b) the RMS amplitude variation for the same horizon.

The AVO analysis was performed interactively using the three term Aki-Richards equation on arbitrary CDP supergathers. An example of the AVO analysis for one of the CDP supergathers located on inline 62 and crossline 42 is illustrated in Figure 5.10. It was observed that the near offset data for 0 to 250 m provided a vague amplitude anomaly and created less reliable results due to the low signal-to-noise ratio. The correlation coefficient for the AVO curve used to fit the data for the full offset range was obtained to be 0.62. However, for the offset range 250-1750 m it was calculated to be 0.78. This correlation was considered satisfactory.

The maximum angle corresponding to the reflectivity associated with Semblana was found to be 45 degrees. Due to the rapid V_p , V_s and density increase, a distinctive AVO anomaly was observed from the AVO curve used to fit the Semblana reflectivity after considering the polarity of the source wavelet, which is also displayed in Figure 5.10.

These results were used in the AVO attribute analysis.

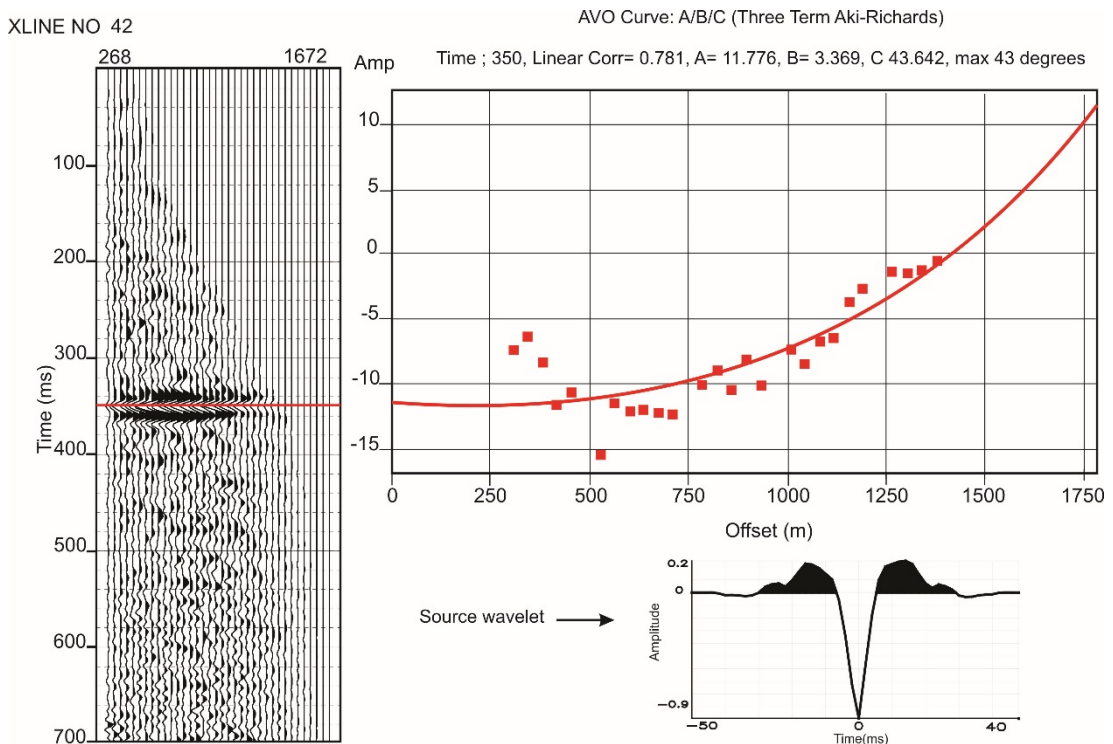


Figure 5.10 An example AVO analysis on CDP supergather (on the left) located in crossline 41. The red line is pointing to the horizon that AVO analysis is performed on the upper right.

Two high priority targets as identified during the interpretation session conducted on the conventionally processed dataset, which can still be observed as possible amplitude anomalies in the PRA reprocessed volume, were selected to perform an interactive AVO analysis on (Figure 5.11). The results showed that they did not provide any distinguishable AVO response. This important observation was demonstrated the unique nature of the Semblana reflector and how an AVO analysis would reject these original targets from further investigation.

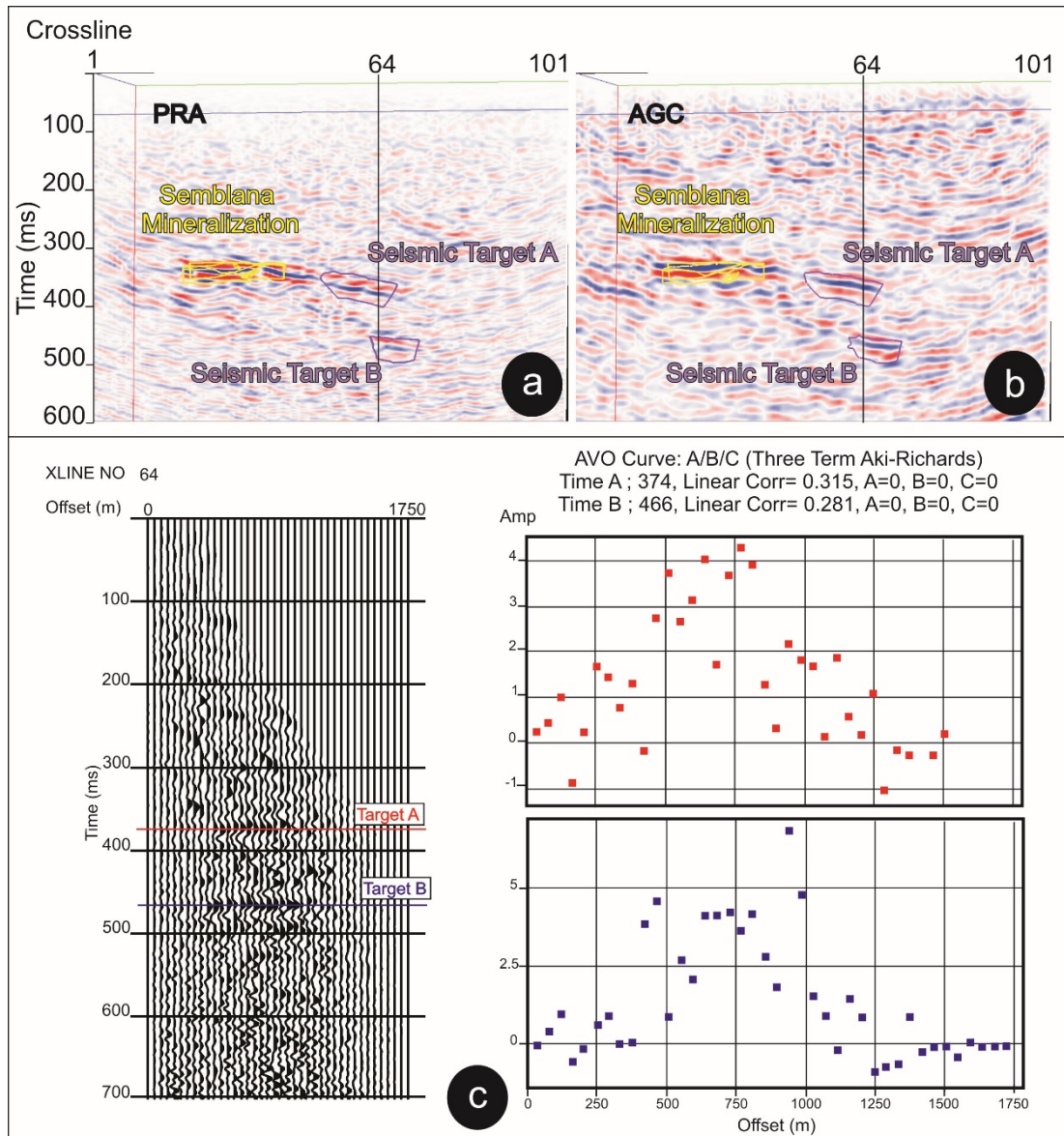


Figure 5.11 Target A & Target B are overlain on a) PRA and b) AGC crossline 51. The CDP supergather which sits on crossline 51 underwent an interactive AVO analysis as shown in c). The red line for Target A and blue line for Target B represent the horizons for which the AVO analysis was performed.

5.2.1 AVO attributes

The elastic rock properties of the reflector can be obtained by solving the AVO equations derived from the Zoeppritz equations. However, the Zoeppritz equations are very complicated. Instead of this complicated set of equations it was more practical to apply the Aki – Richards's approximation to the equations with the Wiggins modification for AVO analysis. According to these equations, we mainly focus on the intercept (A) and the gradient (B) parameters. The intercept parameter represents to the first degree of approximation the zero offset reflectivity as it is a function of Vp and density differences across the interface. On the other hand, the gradient is dominated by the rate of change of Poisson's ratio, which gives us information about the stiffness and the deformation of the medium as a function of Vp and Vs. Since the data included information up to 45 degrees curvature, the (C) term was also analysed. This would allow us to obtain the relative Vp, Vs and density changes separately.

The AVO attribute values for a single CDP supergather are shown in Figure 5.10. The AVO attribute analysis started with the generation of the AVO reconnaissance attributes, such as intercept (A), gradient (B), curvature (C) and the scaled Poisson's ratio changes ($aA+bB$) throughout the AVO horizon for all CDP supergather. These attributes are mapped in Figure 5.12. Relative Vp, Vs and density changes were also calculated for all CDP supergather and are illustrated in Figure 5.13.

In order to perform a 3D AVO attribute analysis, AVO attribute volumes were generated. These attribute volumes are displayed in Figure 5.14 for inline 62. The attribute maps and volumes allowed us to investigate the AVO response for the Semblana reflectivity.

It can easily be observed that the Semblana orebody provided a significant and unique AVO response in the AVO attribute maps (Figure 5.12 and 5.13). The attribute analysis in Figure 5.12 and Figure 5.13 clearly showed anomalous values related to the presence of the Semblana orebody and is in agreement with the results of the elastic property measurements (Section 3.2). However, the increase in density was less than expected from the elastic property table. This was interpreted as an error commonly encountered in the calculation of the curvature (C) term, caused by

the absence of far offsets, which are required for the stable recovery of the curvature factor value.

A more important result was achieved in the AVO attribute volumes. As is illustrated in Figure 5.14, a clear AVO response can only be observed for the Semblana mineralization. After the investigation of all seismic cube, stockworks and rhyolites do not provide any recognisable AVO response. These encouraging results were further investigated through the implementation of the elastic impedance inversion. The main reason for the computation of elastic impedances was to establish a correlation between acoustic impedance and elastic impedance from the core sample tests.

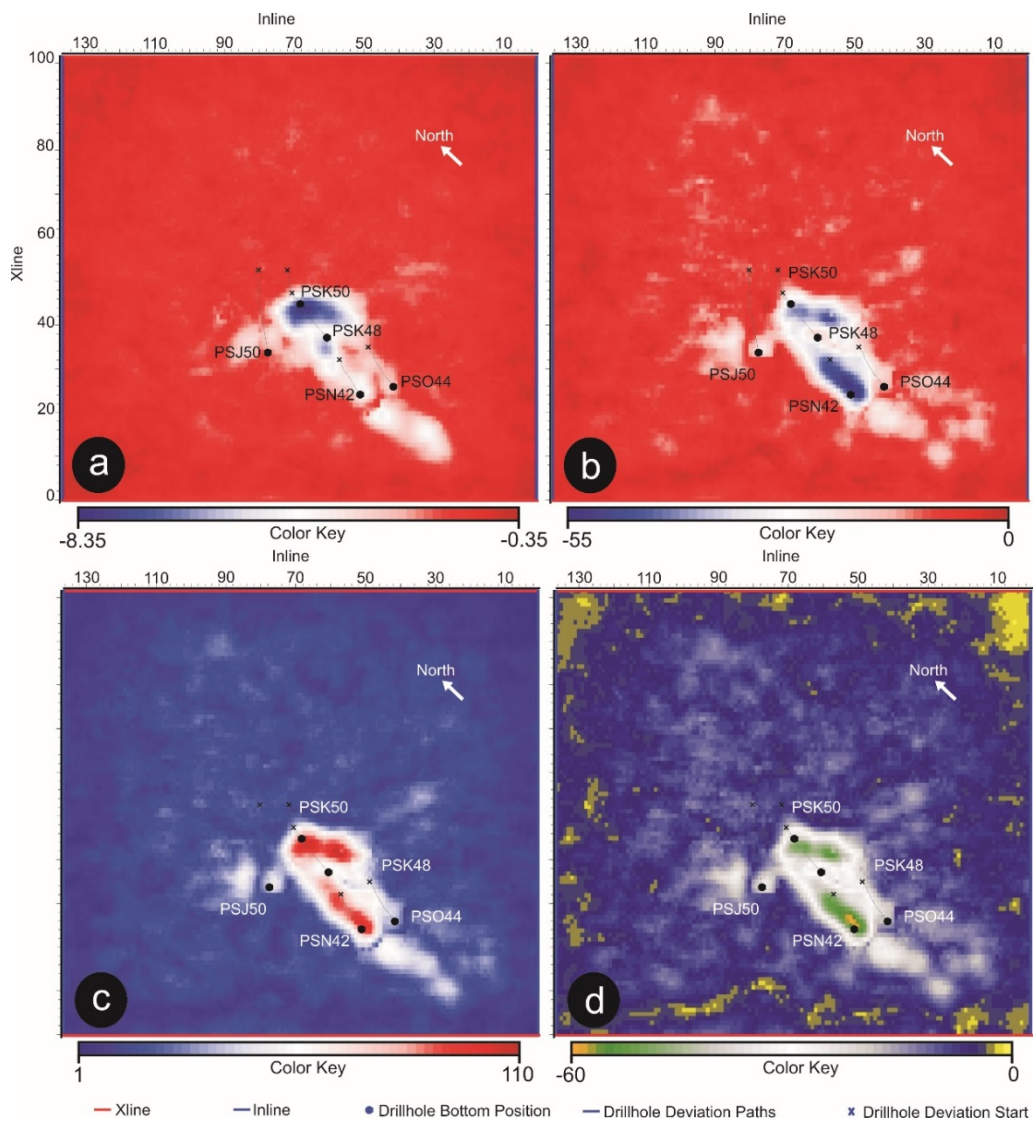


Figure 5.12 The variation of **a)** intercept, **b)** gradient, **c)** curvature and **d)** scaled Poisson's ratio changes over the AVO horizon.

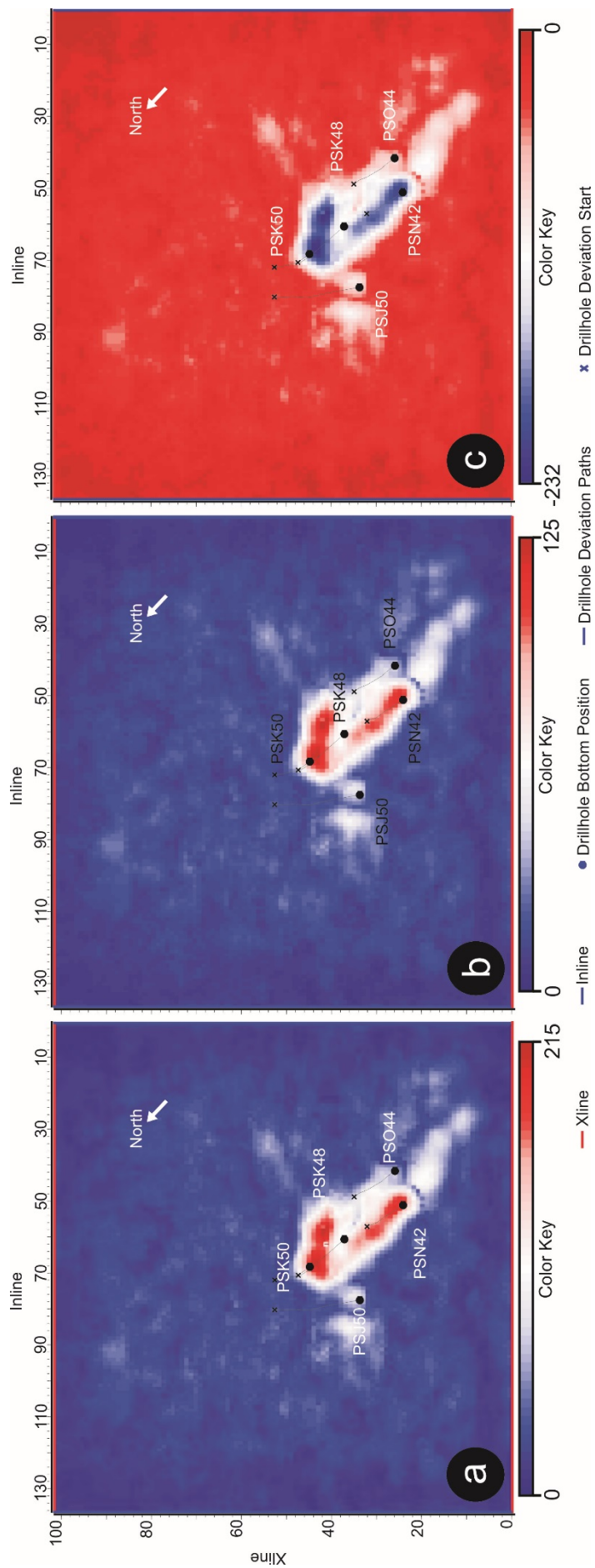


Figure 5.13 The variation of relative a) V_p , b) V_s and c) density changes over the AVO horizon.

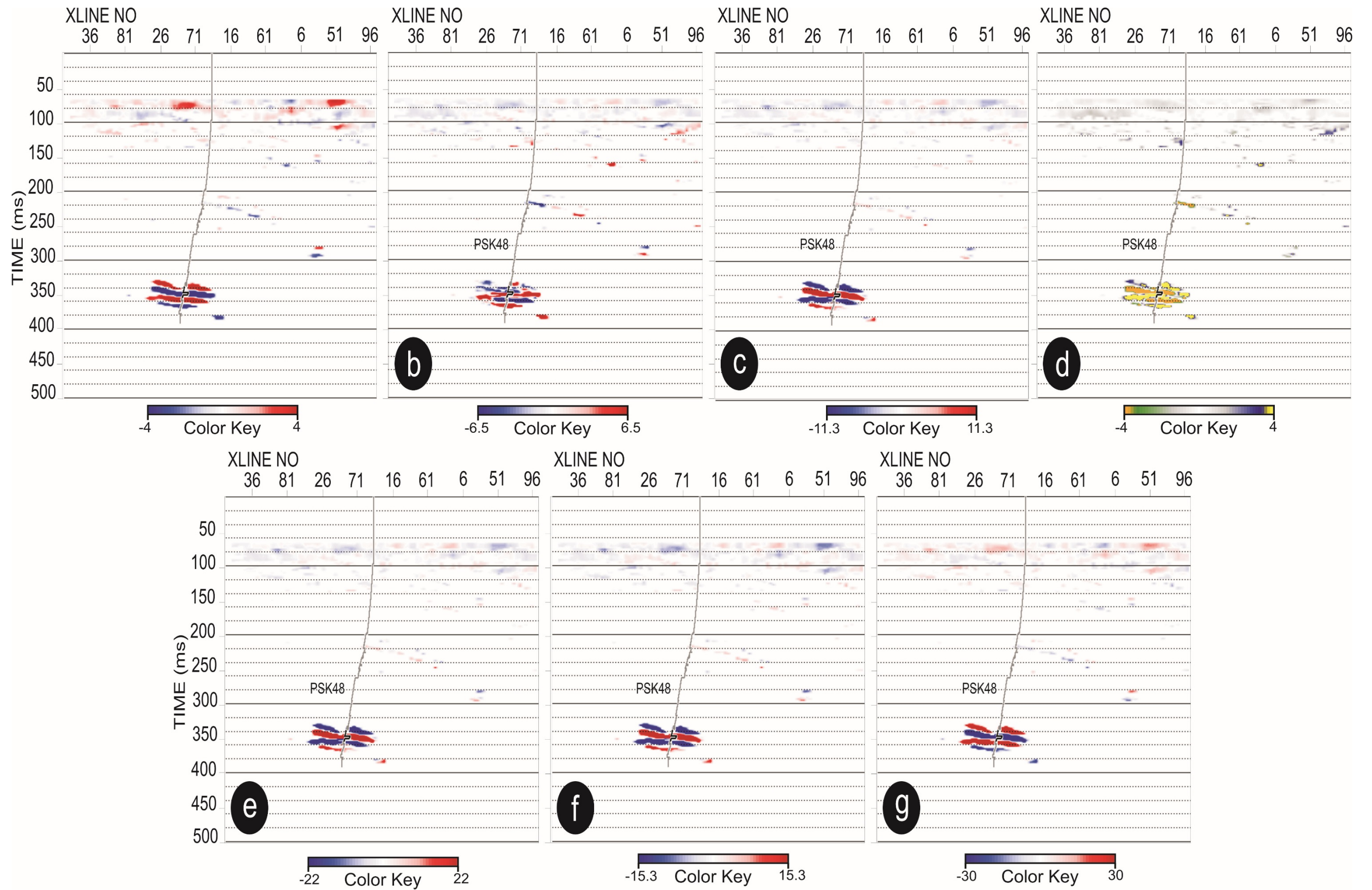


Figure 5.14 Variation of AVO attributes in 3D. **a)** Intercept, **b)** gradient, **c)** curvature, **d)** scaled Poisson's ratio, **e)** relative Vp, **f)** relative Vs and **g)** relative density volumes for inline 62.

5.2.2 Partial Stacking

In seismic data processing, all traces belonging to the same midpoint are simply stacked together over the full source-receiver offset range. However, partial stacking averages only those traces with their offset and azimuth within a given range. Partial stacking is used to observe variations in amplitude for events that display AVO effects.

As it was reported in Connolly (1999), near-offset amplitudes, which correspond to the intercept AVO attribute, can be stacked to observe the changes in acoustic impedance. However, far-offset stacks can provide information about the function of reflectivity dependent on variable incidence angle, also known as elastic impedance or shear wave impedance, equivalent to P-wave or acoustic impedance. Elastic impedance can provide important information on the seismic characterization of the prospective zone and will be discussed more in this study.

In order to analyse the amplitude changes for different offset ranges on post-stack data and to relate these changes to the AVO attributes, the Semblana dataset was partially stacked into the near-offset and far-offset data range. For the Semblana orebody, which is located at a depth of 820 m, an offset range from 0-500 m was decided as the near offset. An offset range of 500-1250 m with a corresponding angle range of higher than 30 degrees was decided as the far offset range during the partial stacking process. The near-offset and far-offset partial stacks are displayed in Figure 5.15.

A brighter seismic response was observed in the far-offset stack as shown in Figure 5.15. This result proved that the seismic response of the Semblana orebody has an angle (offset) dependency. This AVO response shows that by using different offset stacks additional targeting criteria could be created that further differentiate reflectors associated with massive sulphide from non-economic reflectors.

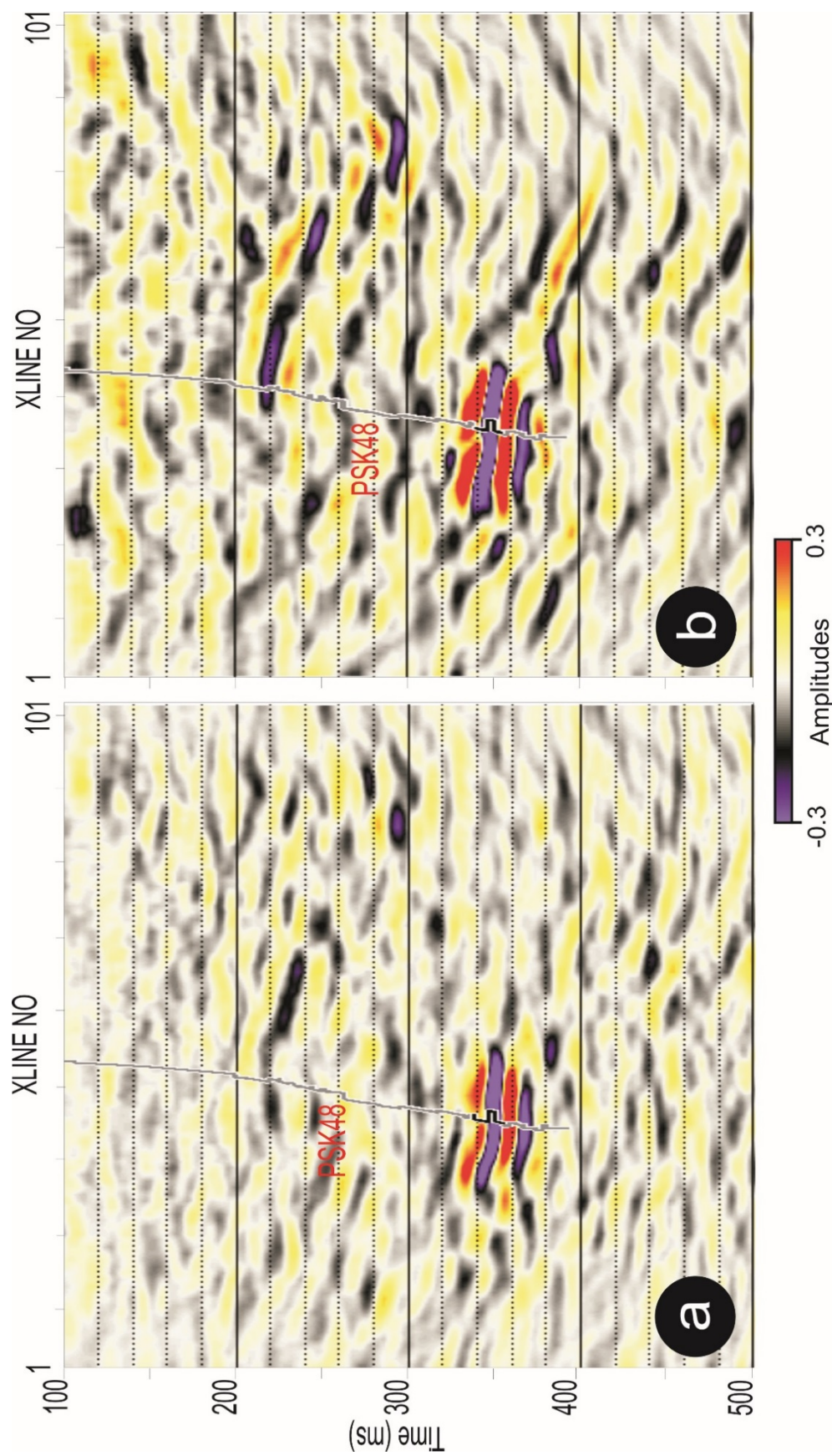


Figure 5.15 a) Near offset (0-500 m) and b) far-offset (500-1750 m) stacks for inline 62.

5.3 Elastic Impedance Inversion

Elastic impedance is a seismic attribute that was developed by Connolly (1998). Elastic impedance inversion provides a robust framework to calibrate and invert non zero-offset seismic data similar to what acoustic impedance inversion does for zero-offset data. As explained in section 2.6, the theoretical derivation of elastic impedance involves a linearization of the Zoeppritz equations.

The first known attempt at a 3D elastic impedance inversion on a hard rock dataset was performed in this study. Unlike acoustic impedance inversion, elastic impedance inversion can be performed on pre-stack data. This can provide information about the seismic properties of the medium as well as incorporating the angle dependency. These inverted seismic properties of the medium could then be directly tied to the elastic property measurement results performed in Subsection 3.2. This could significantly benefit the seismic characterization of the Semblana orebody by extrapolating the known response from drilled core samples to the rest of the 3D volume.

The same database that was used during the acoustic impedance inversion and AVO analysis was also used in the elastic impedance inversion. The intention was to first perform an elastic impedance inversion on the partial stacks created towards the end of the AVO analysis. The first step was to create near-offset and far-offset elastic impedance logs in the modelling window for all drillholes that were actively used in the previous inversion and analysis. P-wave velocity, S-wave velocity and density logs were required in the calculation of the elastic impedance logs for the defined incidence angle or offset value. As was mentioned in subsection 5.2.2, a 0-30 degrees angle of incidence was used to stack the near-offset data. Consequently, a 15 degree angle was used to transform near-offset elastic logs. To transform the far-offset elastic impedance logs, a 38 degree angle of incidence was used for far-offset stacking.

5.3.1 Near-offset and Far-offset Inversion

The elastic logs were used in the model based elastic impedance inversion of both near-offset and far-offset volumes separately. The model based elastic impedance

inversion methodology had the exact same procedure as the model based acoustic impedance inversion. Firstly, a model was built using the drillholes and the AVO horizon. An error analysis was then conducted to achieve the best parameters with the smallest error. Afterwards, a model based inversion was run with these parameters to produce the elastic impedance volumes. Near-offset and far-offset elastic impedance volumes are shown in Figure 5.16 and Figure 5.17 respectively. Reasonably consistent near and far-offset inversion results were achieved considering all the complexities that are encountered in hard rock environments.

The comparison between the elastic impedance inversions presented in Figures 5.16 and 5.17 and the acoustic impedance inversion presented in Figure 5.6 showed that both the acoustic and elastic impedance cubes imaged the sulphides well. However, the elastic impedance inversion mapped the CULM better than the acoustic impedance inversion. This can be related back to the elastic property crossplot (Figure 3.8) showing slightly higher sensitivity of elastic impedance to the presence of massive sulphides in comparison to acoustic impedance.

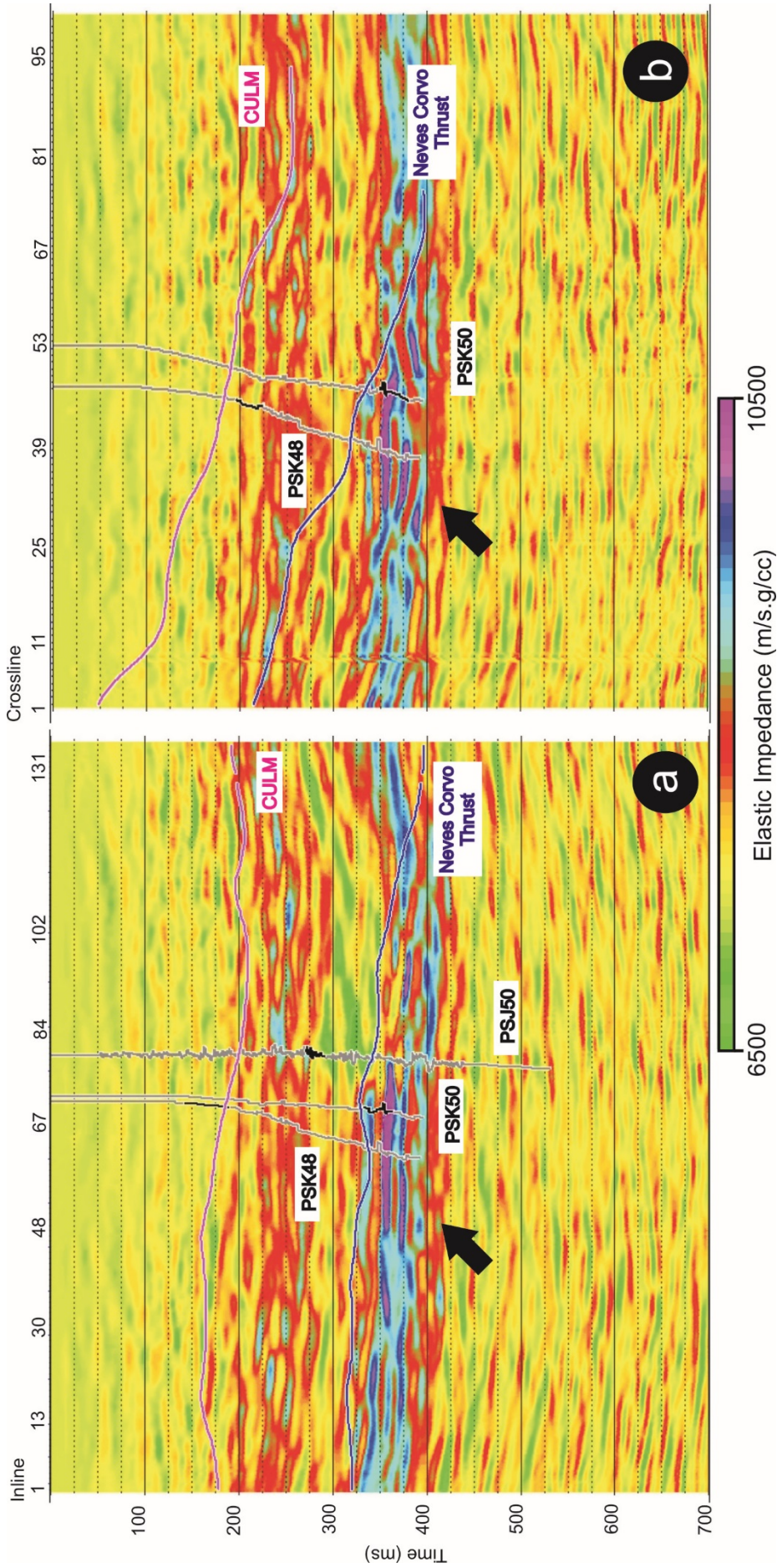


Figure 5.16 Near offset elastic impedance inversion cube. A section from **a**) crossline 46 and **b**) inline 69. Pseudo logs of PSK48 and PSK50 and FWS log of PSJ50 were displayed with the Neves Corvo thrust and CULM. Black arrows point out the location of the Semblana orebody.

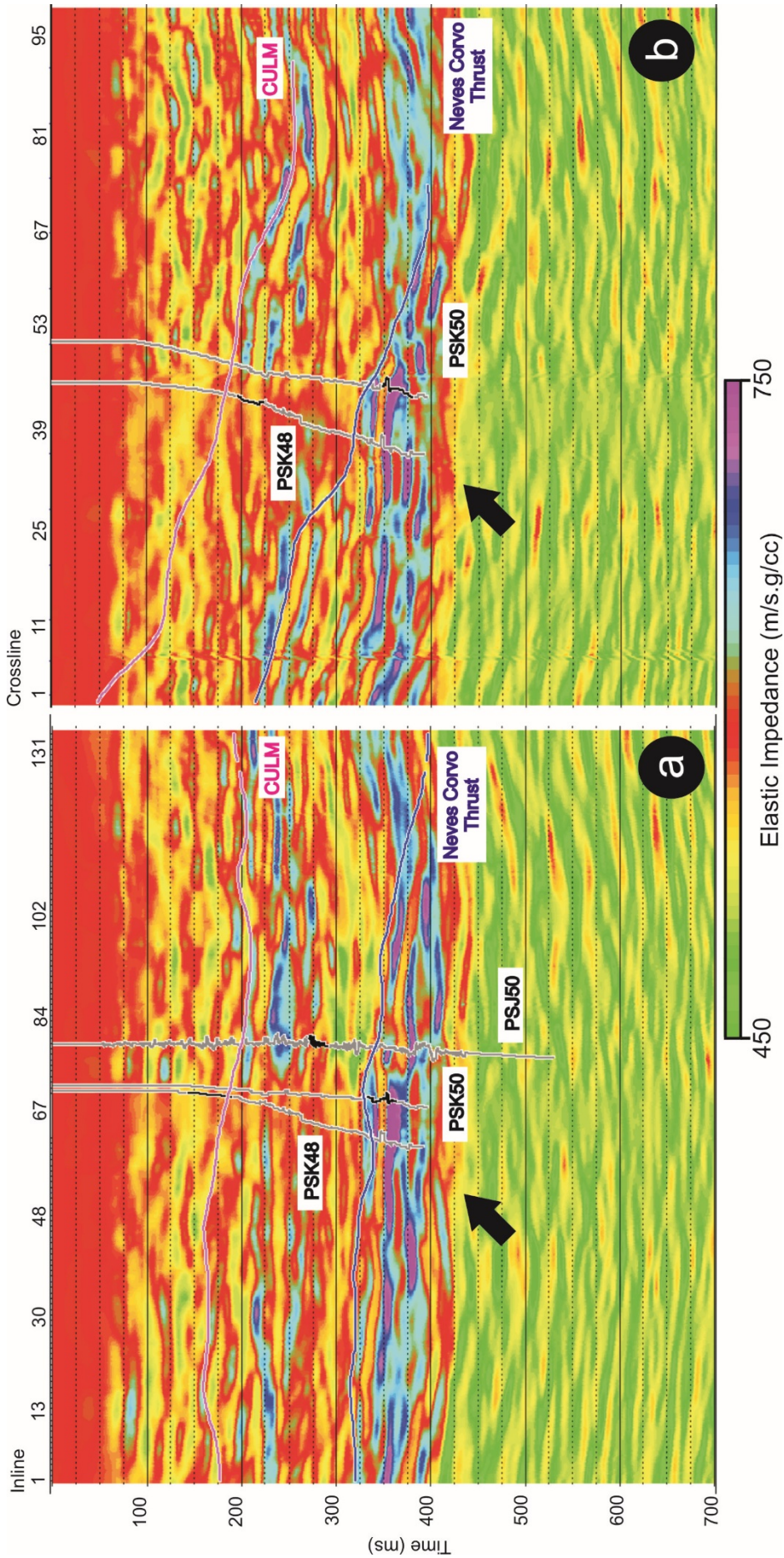


Figure 5.17 Far offset elastic impedance inversion cube. A section from **a**) crossline 46 and **b**) inline 62. Pseudo logs of PSK48 and PSK50 and FWS log of PSJ50 were displayed with the Neves Corvo thrust and CULM. Black arrows point out the location of the Semblana orebody.

5.3.2 Crossplots

The next important step in carrying out an elastic impedance inversion was to investigate the results. While the near-offset inverted results were approximately providing information related to acoustic impedances, the information related to elastic impedance changes could be obtained from the far-offset inverted cube. The acoustic and elastic impedance values of massive sulfides were tested in section 3.2 and results showed that there was a unique separation in between massive sulfide and the other lithologies (Figure 3.8). This was also supported by the AVO attribute maps and volumes as well. In order to further investigate this unique separation crossplots were utilized.

The near-offset and far-offset elastic impedance values for the whole cube within a 150 ms time window centred on the AVO horizon was graphed (Figure 5.18). Considering the elastic property measurement results (Figure 3.8) the anomalously high values are believed to correspond to massive sulfides. These values were encountered within Zone 2 and are related to the presence of massive sulphides (Figure 5.18d). The rest of the values were considered to belong to the background trend and were assigned to Zone 1 (Figure 5.18c). The zones marked in Figure 5.18 were subsequently translated to and highlighted in the inverted cube (Figure 5.18 a and b). An excellent match was observed throughout the cube. This is the first documented study involving the application of 3D acoustic and elastic impedance inversion for hard rock characterisation and has shown very encouraging results. These results also show that especially in the case of high pyrite content, which provides very significant acoustic and elastic impedance variation, the crossplotting technique could be used to better interpret inversion results in order to discriminate the target reflectors.

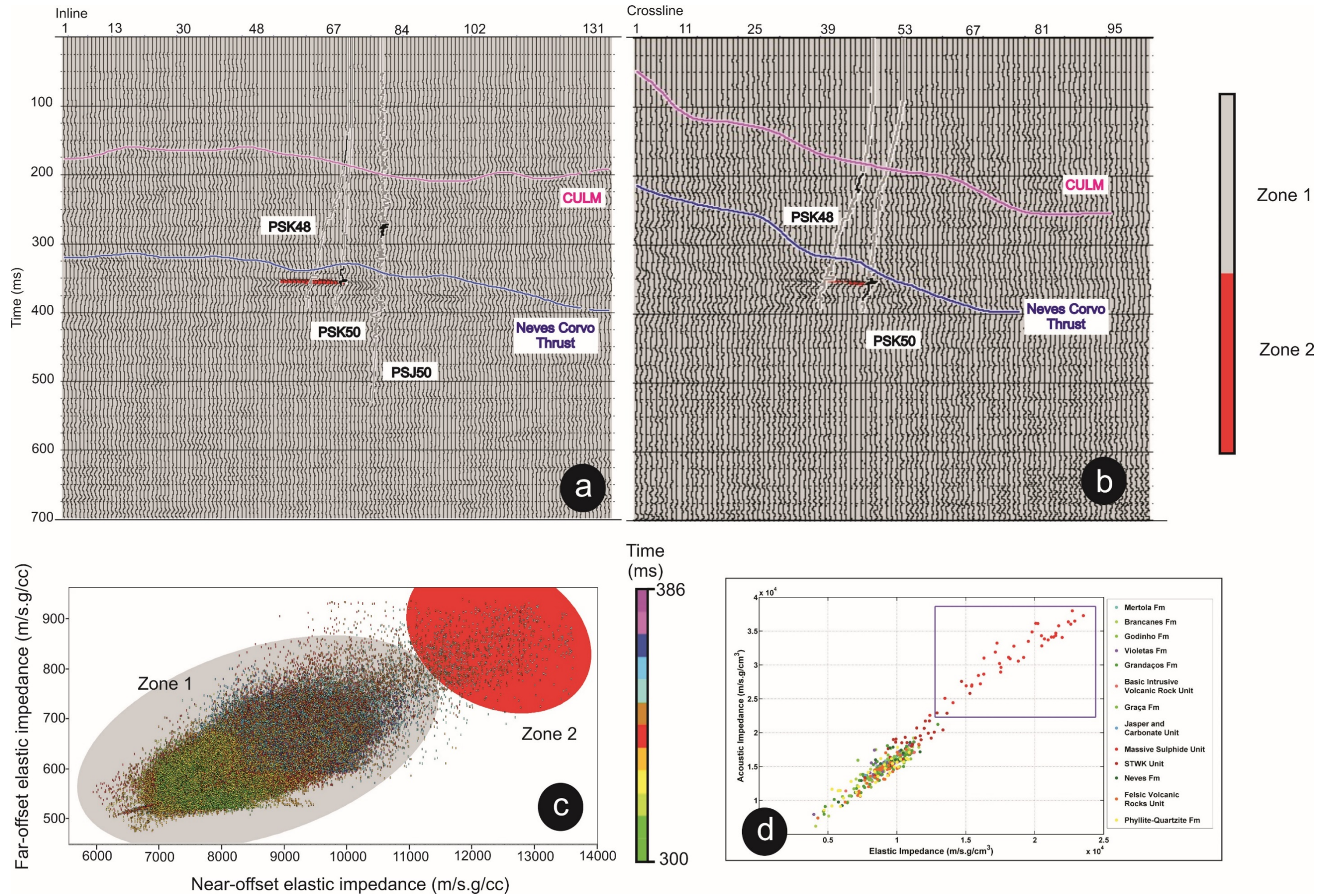


Figure 5.18 Crossplots of the elastic impedance inversion results with seismic sections from **a**) crossline 46, **b**) inline 62, **c**) the crossplots and **d**) Figure 3.8. From Figure 3.8, Zone 1 (grey color) and Zone 2 (red color) were highlighted on the seismic sections in a) and b). Pseudo logs of PSK48 and PSK50 and FWS log of PSJ50 are displayed with the Neves Corvo thrust and CULM.

5.4 Discussion and Conclusions

The results of the model based acoustic impedance inversion were investigated against drillhole data and measured logs. As a result, a distinctively clear acoustic impedance variation correlated extremely well with the Semblana mineralization. This was consistent with the results of the volumetric interpretation conducted on the reprocessed seismic data. However, some acoustic impedance anomalies were also observed nearby Semblana but are not related to the mineralisation.

In AVO analysis, the creation of CDP supergathers provided an increase in signal-to-noise ratio, which made analysing AVO responses and partial stacking easier. A new horizon was picked for the Semblana reflection and interpolated throughout the volume in order to analyse it in 3D and to run an elastic impedance inversion. An RMS amplitude variation in a time slice over this horizon provided detailed information regarding the location and the possible distribution of the AVO response for the Semblana mineralization. Several CDP supergathers were analysed interactively to investigate the AVO response of the Semblana reflection, where the offset range was found to be 0 - 1250 m. High correlation coefficients for the AVO curve fitted to the data provided the confidence to continue with the AVO attribute analysis. The range of angles of incidence was found to be up to 45 degrees for the Semblana mineralisation. The AVO analysis also showed that it might have some role to play in the characterisation of massive ore deposits such as Semblana. A distinctive AVO anomaly was observed in the interactive AVO analyses of several successive CDP supergathers. Moreover, the same AVO analysis performed on two previously interpreted high priority targets that can still be observed as potential amplitude anomalies in the PRA reprocessed volume did not provide any distinguishable AVO response. This demonstrates that even in the case of anomalously high amplitude seismic reflectors interpreted from PRA data not associated with massive sulfide, an AVO analysis would filter them out as potential targets. The elastic property measurements of these lithologies, which were subsequently drilled and found to be rhyolites, show that their elastic properties do not warrant the creation of any considerable amplitude anomaly in this geological setting. Since AVO parameters are derived from elastic parameters, the AVO analysis demonstrated unambiguous and more consistent results with the elastic

parameters compared to interpreting the amplitude section on its own. This observation suggests that AVO will have an important role to play for the direct targeting of massive ore bodies.

AVO attribute analyses were performed in both 2D and 3D. AVO attribute maps were created all along the AVO horizon and provided quite significant results. The AVO attribute maps created with intercept, gradient, curvature and scaled Poisson's ratio changes provided a significant anomaly for the Semblana mineralization, exclusively. The relative V_p , V_s and density changes were all observed on the corresponding AVO attribute maps. A significant increase in relative V_p and V_s values for the Semblana orebody was consistent with the results of elastic property measurements (Section 3.2) made on core samples. However, the expected anomalously high density values were not observed. As mentioned before, this may be related to the errors in the curvature (C) recovery due to insufficiently long offsets for an accurate three term inversion.

In order to investigate these results throughout the volume, AVO attribute volumes were then generated. A distinctive AVO response was observed both on the attribute maps and the attribute volumes. The AVO signature of the Semblana mineralisation was unique and could be easily discriminated from other lithologies such as rhyolites and even stockworks if they not in contact. Afterwards, an interactive AVO analysis was also trialled over two high priority targets originally interpreted from the conventionally processed AGC dataset and that can still be identified as possible amplitude anomalies in the PRA data. The results showed they didn't provide any distinguishable AVO response. This demonstrated the importance of conducting a quantitative interpretation when validating targets identified from the seismic volume.

In order to strengthen this statement, near-offset and far-offset partial stacks were created. Afterwards, model based elastic impedance inversion was performed on these partial stacks to analysis the offset dependent amplitudes in order to further characterise the Semblana orebody. The elastic impedance inversion appears to enhance the different seismic signatures of the lithologies at Neves Corvo as well. The comparison of the acoustic and elastic impedance inversion showed that while massive sulphide were accurately imaged with both techniques, inverted elastic

impedances were able to image the CULM on near offset stacks more accurately. This could be related back to the physical properties, which show anomalously high acoustic and elastic impedance values are characteristic for massive sulphides in the Neves Corvo region.

The unique separation in between massive sulfide and the other lithologies was previously proven through the elastic property measurement results and this result was also supported by the AVO attribute analysis. After the elastic impedance inversion of the partial stack, the crossplots showed a significant match with the massive sulfide zonation.

The pseudo drillhole logs inferred from the core sample measurements provided almost as good a response as the FWS logs in both the acoustic and elastic inversion. As such they can be used for seismic to drillhole calibration when wireline logs are absent.

Chapter 6

Discussions and Conclusions

The main objective of this thesis was to address the amplitude non-uniqueness issue in order to discriminate the seismic response of massive sulfide from the other lithologies and to better delineate the major geological structures in the area. To achieve this it was necessary to introduce certain novelties and new approaches into hard rock seismology. This study began with characterizing the seismic response of key lithologies and geology through elastic property measurements and synthetic modelling. Preserved relative amplitude processing was then utilized and a volumetric interpretation was undertaken to enhance direct mineral targeting. Acoustic impedance inversion, AVO analysis and elastic impedance inversion in order to discriminate massive sulphides from other lithologies were the final steps in the approach. The key outcomes and novelties are stated below:

- Pseudo logs
 - The first important advancement was to demonstrate the applicability of pseudo logs to act as a proxy for wireline logs in conducting drillhole-to-seismic ties in hard rock seismic exploration. Any additional drillhole information can play a critical role in the success of seismic imaging but unfortunately downhole seismic logging is not common practice in mining. However, routine extraction and storing of diamond drillhole core is and it can provide an invaluable dataset to be exploited. This could also allow the

reviving of old drillholes and to create significantly important logs in order to be utilised in hard rock seismic exploration. Having a good grip of geology and particularly comprehensive core sampling could provide huge potential to perform the calibration of larger scientific datasets as well. Therefore, an attempt to create pseudo logs by measuring the P-wave velocity and density of individual core samples was made, which could then be used to perform drillhole-to-seismic ties in the place of FWS logs. A careful core sample selection process, including adequate sampling down the hole and correlation with lithological logs helped to create appropriate pseudo logs. A high level of correlation between the pseudo logs and the FWS logs demonstrated that pseudo logs could act as a proxy for FWS logs and could represent in situ properties in hard rock seismic. These logs also enable the further acoustic and elastic impedance inversions as well as the AVO analysis.

- PRA with PSTM
 - The second advancement was achieved through the preserved relative amplitude processing complete with the application of PSTM. This seismic processing approach is common in soft rocks. However, the intrinsically low signal-to-noise ratios of hard rock geology and generally higher ambient noise environments make PRA processing non-trivial. In such situations it is particularly hard to apply PSTM as this process is very sensitive to noise. To address this, a linear radon transform considerably attenuated the coherent noise and made PSTM result more viable.
- Volumetric Interpretation
 - A qualitative volumetric interpretation applied to the preserved amplitude PSTM cube enabled reliable discrimination of the mineralisation from the host rock and other false amplitude anomalies. The AGC cube also utilized the marker horizons, mineralization wireframes and selected drillholes in order to gauge the effectiveness of the PRA reprocessing as well as to reinspect the high priority targets originally interpreted on the conventionally processed volume. It facilitated the critical observation that the strongest reflection in the PRA seismic cube was unambiguously associated with the Semblana mineralisation and completely matched the mineralization wireframe. The PRA approach was adopted to clearly resolve the amplitude non-uniqueness issue associated with the AGC dataset. The amplitude

responses of the non-mineralised high priority targets were found to be too weak to be considered as potential massive sulfide targets, which was also consistent with subsequent drilling results. These results were also validated with the incorporation of volumetric iso-shells, which demonstrated the improved zonation of the target based on the PRA reprocessing.

- Acoustic inversion, AVO analysis and Elastic inversion
 - Another achievement of great importance to mineral seismic comes from the utilisation of 3D acoustic impedance inversion, AVO analysis and elastic impedance inversion in order to undertake a quantitative interpretation of the Semblana orebody and further discriminate massive sulphides from other lithologies. Acoustic impedance inversion showed that a distinctively clear acoustic impedance variation can be observed for the Semblana orebody. This result was found to be consistent with the results of the volumetric interpretation conducted on the reprocessed seismic data, but the accuracy degrades the further you get from the boundaries of the orebodies.
 - While the 3D acoustic impedance inversion produced a stable output, the AVO analysis showed much more encouraging results. Several interactive AVO analyses were performed on CDP supergathers to investigate the AVO response of the reflection associated with Semblana, where it was found that a high correlation coefficient was achieved while fitting a standard curve to the AVO response. On the other hand, some high priority reflectors which can still be interpreted as a possible target did not provide any AVO response. This demonstrated the importance of validating the direct targeting through a quantitative interpretation.
 - For the first time in hard rock seismic, a 3D elastic impedance inversion was performed utilising partial stacks. The crossplots of near-offset and far offset data showed two distinct and different zones consisting of the massive sulfides and background rock formations based on the elastic property measurements. These zones were superimposed onto the inverted partial stack cube where a significant correlation with the massive sulfide was observed. Proving the unique separation in between massive sulfide and the other lithologies was one of the biggest achievements of this study. This work clearly shows the importance of using a full suite of techniques together in order to delineate complex mineralogies.

6.1 Further work

This study is of importance to the future of seismic surveying not only within the entire Iberian Pyrite Belt, but for VMS exploration worldwide. Encouraging results prove that the surface seismic reflection technique is a viable exploration tool for mineralised terrains but there is still plenty of scope for improvement going into the future.

The seismic method's ability to provide high resolution information at depths greater than almost any other technique has caught the mining industry's attention for a while now. However, the long held view that seismic is too expensive for mining applications is quickly changing. As technology advancements in the area of computing facilities and the mass production of acquisition hardware take hold, the overall price per channel of seismic has decreased at a marked rate in last decade (from over \$2500/channel to below \$600/channel).

In order to utilize cost effective seismic surveys in mineral exploration the use of new technology, smarter survey geometries and specialised small sized seismic crews need to be pursued. Surface and downhole seismic acquisition geometries need to be designed based on the target characteristics, such as its volume and 3D shape. It may then be possible to achieve adequate resolution with alternative, hybrid geometries instead of relatively expensive 3D orthogonal geometries. For example, the acquisition of modified marine swath surveys such as swath-slalom style surveys may be of interest for deposits controlled by shear zones. The use of different types of sources could also contribute to cost reduction.

Another important advancement could be achieved with the use of more advanced downhole seismic surveys. It was proven in this study that drillhole logs are as important as the seismic data in order to achieve good results in mineral exploration. VSP surveys have been underutilized in mineral exploration and the inception of multi-azimuth walkaway VSP, combined with surface receivers could greatly enhance the characterisation of orebodies.

The use of inversion techniques was shown to provide valuable input in orebody characterization. However, all of the software that has the capability to perform these

advanced processing techniques was designed for hydrocarbon exploration. Therefore, their main function is to characterise sedimentary geological processes and are not suited to the highly complex nature of mineralised terrains. The well logs and the interpreted horizon are the most important inputs and have a strong control on the outcome. Most of the inversion algorithms interpolate along and in between horizons and do not have the ability to take into consideration 3D geobodies, such as the orebodies that exist in this study. In order to properly utilize inversion techniques, it is essential that the algorithms are modified to take into account the nature of hard rock geology.

References

- Adam E., Arnold G., Beaudry C., Matthews L., Milkereit B., Perron G. and Pineault R., 1997. Seismic exploration for VMS deposits, Matagami, Quebec: Geophysics and geochemistry at the millenium: proceedings of Exploration 97: fourth decennial international conference on mineral exploration, 433-438.
- Adam E., Milkereit B., Arnold G. and Pineault R., 1996. Seismic response of the Bell Allard orebody, Matagami, Quebec: SEG Technical Program Expanded Abstracts 1996, 634-637.
- Adam E., Milkereit B. and Salmon B., 2004. 3-D seismic exploration in the Val d'Or mining camp, Quebec: SEG Technical Program Expanded Abstracts 2004, 1167-1170.
- Aki K. and Richards P. G., 1980. Quantitative Seismology: Theory and Methods. *Volume I: WH Freeman & Co.*
- Bancroft J. C., 1998. A practical understanding of pre-and poststack migrations: Society of Exploration Geophysicists
- Bancroft J. C., Geiger H. D. and Margrave G. F., 1998. The equivalent offset method of prestack time migration. *Geophysics* **63** (6), 2042-2053.
- Barrie C. T. and Hannington M. D., 1999. Volcanic-associated massive sulfide deposits: processes and examples in modern and ancient settings
- Barriga F. J. A. S., Carvalho D. and Ribeiro A., 1997. Introduction to the Iberian pyrite belt. *Society of Economic Geologists, Guidebook Series* **27**, 1-20.
- Behrens R. A., MacLeod M. K., Tran T. T. and Alimi A. C., 1998. Incorporating Seismic Attribute Maps in 3D Reservoir Models. *Reservoir Evaluation & Engineering* **1** (02), 122-126.
- Bellefleur G., Malehmir A. and Muller C., 2012. Elastic finite-difference modeling of volcanic-hosted massive sulfide deposits: A case study from Half Mile Lake, New Brunswick, Canada. *Geophysics* **77** (5), Wc25-Wc36.
- Bierbaum S. and Greenhalgh S., 1998. A high-frequency downhole sparker sound source for crosswell seismic surveying. *Exploration Geophysics* **29** (3/4), 280-283.

- Bohlen T., Müller C. and Milkereit B., 2003. 5. Elastic Seismic-Wave Scattering from Massive Sulfide Orebodies: On the Role of Composition and Shape, in D. Eaton, B. Milkereit and M. H. Salisbury, eds., *Hardrock Seismic Exploration: SEG, Geophysical Development Series*, 70-89.
- Bona A., Pevzner R., Tertyshnikov K., Greenwood A., Sun B., Yavuz S. and Urosevic M., 2013. Diffraction Imaging in Hard-rock Environments: 75th EAGE Conference & Exhibition incorporating SPE EUROPEC 2013, 5 p.
- Brocher T. M., Hunter W. C. and Langenheim V. E., 1998. Implications of seismic reflection and potential field geophysical data on the structural framework of the Yucca Mountain–Crater Flat region, Nevada. *Geological Society of America Bulletin* **110** (8), 947-971.
- Calvert A. J. and Li Y. X., 1999. Seismic reflection imaging over a massive sulfide deposit at the Matagami mining camp, Quebec. *Geophysics* **64** (1), 24-32.
- Cao S. and Greenhalgh S., 1997. Cross-well seismic tomographic delineation of mineralization in a hard-rock environment. *Geophysical Prospecting* **45** (3), 449-460.
- Carvalho D., Barriga F. and Munhá J., 1999. Bimodal-siliciclastic systems—the case of the Iberian Pyrite Belt, in C. T. Barrie and M. D. Hannington, eds., *Volcanic-associated massive sulfide deposits: processes and examples in modern and ancient settings: Society of Economic Geologists, Reviews in Economic Geology*, 375-408.
- Cary P. W. and Lorentz G. A., 1993. Four-component surface-consistent deconvolution. *Geophysics* **58** (3), 383-392.
- Chase M. K., 1992. Random noise reduction by FXY prediction filtering. *Exploration Geophysics* **23** (1/2), 51-56.
- Chen G., Liang G., Xu D., Zeng Q., Fu S., Wei X., He Z. and Fu G., 2004. Application of a shallow seismic reflection method to the exploration of a gold deposit. *Journal of Geophysics and Engineering* **1** (1), 12-16.
- Clowes R. M., Calvert A. J., Eaton D. W., Hajnal Z., Hall J. and Ross G. M., 1996. LITHOPROBE reflection studies of Archean and Proterozoic crust in Canada. *Tectonophysics* **264** (1–4), 65-88.
- Connolly P., 1998. Calibration and inversion of non-zero offset seismic: 68th SEG meeting, New Orleans, USA, Expanded Abstracts, 182-184.
- Connolly P., 1999. Elastic impedance. *The Leading Edge* **18** (4), 438-452.
- Cosma C., 1983. Determination of rockmass quality by the crosshole seismic method. *Bulletin of the International Association of Engineering Geology* **26-27** (1), 219-225.
- Cox D. P., Lindsey D. A., Singer D. A. and Diggles M. F., 2003. Sediment-hosted copper deposits of the World: deposit models and database.
- Dahle A., Gjøystdal H., Grammeltvedt G. and Hansen T. S., 1985. Application of seismic reflection methods for ore prospecting in crystalline rock. *First Break* **3** (2), 9-16.

- Dehghannejad M., Bauer T. E., Malehmir A., Juhlin C. and Weihed P., 2012. Crustal geometry of the central Skellefte district, northern Sweden – constraints from reflection seismic investigations. *Tectonophysics* **524–525**, 87-99.
- Drummond B., Lyons P., Goleby B. and Jones L., 2006. Constraining models of the tectonic setting of the giant Olympic Dam iron oxide–copper–gold deposit, South Australia, using deep seismic reflection data. *Tectonophysics* **420** (1–2), 91-103.
- Duchesne M. J. and Gaillot P., 2011. Did you smooth your well logs the right way for seismic interpretation? *Journal of Geophysics and Engineering* **8** (4), 514-523.
- Duncan G., Downey M., Leung L. and Harman P., 1989. The development of cross hole seismic techniques and case studies. *Exploration Geophysics* **20** (2), 127-130.
- Duweke W., Trickett J., Tootal K. and Slabbert M., 2002. Three-dimensional reflection seismics as a tool to optimise mine design, planning and development in the Bushveld Igneous Complex: 64th Conference and Exhibition, EAGE. Mining and Best of SAGA, Extended Abstracts, 1-6.
- Eaton D. W., Adam E., Milkereit B., Salisbury M., Roberts B., White D. and Wright J., 2010. Enhancing base-metal exploration with seismic imaging This article is one of a series of papers published in this Special Issue on the theme Lithoprobe — parameters, processes, and the evolution of a continent. *Canadian Journal of Earth Sciences* **47** (5), 741-760.
- Eaton D. W., Milkereit B. and Adam E., 1997. 3-D seismic exploration: Proceedings of Exploration, 65-78.
- Eaton D. W., Milkereit B. and Salisbury M., 2003b. Seismic methods for deep mineral exploration: Mature technologies adapted to new targets. *The Leading Edge* **22** (6), 580-585.
- Eaton D. W., Milkereit B. and Salisbury M. H., 2003a. Hardrock Seismic Exploration: SEG
- Erick A., Gervais P., Grant A., Larry M. and Bernd M., 2003. 15. 3D Seismic Imaging for VMS Deposit Exploration, Matagami, Quebec, *in* D. Eaton, B. Milkereit and M. H. Salisbury, eds., Hardrock Seismic Exploration: SEG, Geophysical Development Series, 229-246.
- Evans B. J., Urosevic M. and Taube A., 2003. 10. Using Surface-Seismic Reflection to Profile a Massive Sulfide Deposit at Mount Morgan, Australia, *in* D. Eaton, B. Milkereit and M. H. Salisbury, eds., Hardrock Seismic Exploration: SEG, Geophysical Development Series, 157-163.
- Finlayson D. M., 2010. A chronicle of deep seismic profiling across the Australian continent and its margins,
- Frappa M. and Molinier C., 1993. Shallow seismic reflection in a mine gallery. *Engineering Geology* **33** (3), 201-208.
- Friedel M. J., Jackson M. J., Scott D. F., Williams T. J. and Olson M. S., 1995. 3-D tomographic imaging of anomalous conditions in a deep silver mine. *Journal of Applied Geophysics* **34** (1), 1-21.

- Friedel M. J., Scott D. F., Jackson M. J., Williams T. J. and Killen S. M., 1996. 3-D tomographic imaging of anomalous stress conditions in a deep US gold mine. *Journal of Applied Geophysics* **36** (1), 1-17.
- Galley A., Hannington M. and Jonasson I., 2007. Volcanogenic massive sulphide deposits. *Mineral Deposits of Canada: A Synthesis of Major Deposit-Types, District Metallogeny, the Evolution of Geological Provinces, and Exploration Methods: Geological Association of Canada, Mineral Deposits Division, Special Publication* **5**, 141-161.
- Gaspar O. and Pinto A., 1991. The Ore Textures of the Neves-Corvo Volcanogenic Massive Sulphides and Their Implications for Ore Beneficiation. *Mineralogical Magazine* **55** (380), 417-422.
- Gaspar O. C., 2002. Mineralogy and sulfide mineral chemistry of the Neves-Corvo ores, Portugal: insight into their genesis. *The Canadian Mineralogist* **40** (2), 611-636.
- Gendzwill D., 1990. High-resolution seismic reflections in an underground mine: 60th Annual International Meeting, SEG, 397-398.
- Gladwin M. T., 1982. Ultrasonic stress monitoring in underground mining. *International Journal of Rock Mechanics and Mining Sciences & Geomechanics Abstracts* **19** (5), 221-228.
- Goleby B. R., Korsch R. J., Fomin T., Bell B., Nicoll M. G., Drummond B. J. and Owen A. J., 2002. Preliminary 3-D geological model of the Kalgoorlie region, Yilgarn Craton, Western Australia, based on deep seismic-reflection and potential-field data. *Australian Journal of Earth Sciences* **49** (6), 917-933.
- Greenhalgh S. and Manukyan E., 2013. Seismic Reflection for Hardrock Mineral Exploration: Lessons from Numerical Modeling. *Journal of Environmental and Engineering Geophysics* **18** (4), 281-296.
- Greenwood A. J., 2013. Application of Vertical Seismic Profiling for the characterisation of hard rock PhD Thesis, Curtin University.
- Gupta R., 1972. Seismic determination of geological discontinuities ahead of rapid excavation. *Semi Annual Report No. 6311, Bendix Research Laboratory* **40**, 90 p.
- Gustafson L. B. and Williams N., 1981. Sediment-hosted stratiform deposits of copper, lead, and zinc. *Economic Geology* **75**, 139-178.
- Gustavsson M., Israelson H., Ivansson S., Moren P. and Pihl J., 1984. An experiment with the seismic crosshole method in an iron mine. *The Leading Edge* **3** (11), 143-145.
- Harrison C. B., 2009. Feasibility of Rock Characterization for Mineral Exploration Using Seismic Data PhD Thesis, Curtin University.
- Harrison C. B. and Urosevic M., 2012. Seismic processing, inversion, and AVO for gold exploration — Case study from Western Australia. *Geophysics* **77** (5), WC235-WC243.
- Harrison C. B., Urosevic M. B., Stoltz E. B. and Tonn R. B., 2007. Processing, Inversion And Multi Attribute Analysis of the Intrepid Seismic Line At the

- St. Ives Gold Camp, Western Australia: 2007 SEG Annual Meeting, SEG, 1928-1932.
- Hawkins L. and Whiteley R., 1980. The seismic signature of the Elura orebody. *Exploration Geophysics* **11** (4), 183-187.
- Hileman J. A., Embree P. and Pflueger J. C., 1968. Automated Static Corrections. *Geophysical Prospecting* **16** (3), 326-358.
- Holliday J. R. and Cooke D. R., 2007. Advances in Geological Models and Exploration Methods for Copper ± Gold Porphyry Deposits, in B. Milkereit, ed., Proceedings of Exploration 07: Fifth Decennial International Conference on Mineral Exploration, 647-665.
- Jones L. E. A., 2008. Prospect And Regional Seismic Reflection Imaging In Australian Gold Provinces, 3604-3606.
- Juhlin C., Knapp J. H., Kashubin S. and Bliznetsov M., 1996. Crustal evolution of the Middle Urals based on seismic reflection and refraction data. *Tectonophysics* **264** (1-4), 21-34.
- Juhlin C., Lindgren J. and Collini B., 1991. Interpretation of seismic reflection and borehole data from Precambrian rocks in the Dala Sandstone area, central Sweden. *First Break* **9** (1), 24-36.
- Juhlin C. and Stephens M. B., 2006. Gently dipping fracture zones in Paleoproterozoic metagranite, Sweden: Evidence from reflection seismic and cored borehole data and implications for the disposal of nuclear waste. *Journal of Geophysical Research: Solid Earth* **111** (B9), B09302.
- Kinkela J., 2011a. Acquisition Report. *High-Resolution 3D Seismic Survey Neves-Corvo, Portugal*, 22 p.
- Kinkela J., 2011b. Final Processing Report. *High-Resolution 3D Seismic Survey Neves-Corvo, Portugal*, 31 p.
- Kinkela J., 2011c. Interpretation Report. *High-Resolution 3D Seismic Survey Neves-Corvo, Portugal*, 13 p.
- Klemm D. D. and Schneider H. J., 1977. Time and Strata Bound Ore Deposits: Springer, xvii, 444 p.
- Knopoff L. and Gangi F. A., 1959. Seismic Reciprocity. *Geophysics* **24** (4), 681-691.
- Korsch R. J. and Kositsin N., 2010. GOMA (Gawler Craton-Officer Basin-Musgrave Province-Amadeus Basin) Seismic and MT Workshop 2010: Extended Abstracts: Geoscience Australia
- Leistel J. M., Marcoux E., Thiéblemont D., Quesada C., Sánchez A., Almodóvar G. R., Pascual E. and Sáez R., 1997. The volcanic-hosted massive sulphide deposits of the Iberian Pyrite Belt Review and preface to the Thematic Issue. *Mineralium Deposita* **33** (1-2), 2-30.
- Li S., Mooney W. D. and Fan J., 2006. Crustal structure of mainland China from deep seismic sounding data. *Tectonophysics* **420** (1-2), 239-252.
- Li T. and Eaton D. W., 2005. Delineating the Tuwu porphyry copper deposit at Xinjiang, China, with seismic-reflection profiling. *Geophysics* **70** (6), B53-B60.

- Lundin Mining Corporation, 2013. Neves-Corvo Summary Report. Accessed September 25, 2014. www.lundinmining.com/i/pdf/Summary-Report-Neves-Corvo-Dec-2013.pdf. **Lundin Mining Corporation**, 1-8.
- Malehmir A., Andersson M., Lebedev M., Urosevic M. and Mikhaltsevitch V., 2013. Experimental estimation of velocities and anisotropy of a series of Swedish crystalline rocks and ores. *Geophysical prospecting* **61** (1), 153-167.
- Malehmir A., Dahlin P., Lundberg E., Juhlin C., Sjöström H. and Högdahl K., 2011. Reflection seismic investigations in the Dannemora area, central Sweden: Insights into the geometry of polyphase deformation zones and magnetite-skarn deposits. *Journal of Geophysical Research: Solid Earth* **116** (B11), B11307.
- Malehmir A., Durrheim R., Bellefleur G., Urosevic M., Juhlin C., White D., Milkereit B. and Campbell G., 2012b. Seismic methods in mineral exploration and mine planning: A general overview of past and present case histories and a look into the future. *Geophysics* **77** (5), WC173-WC190.
- Malehmir A., Juhlin C., Wijns C., Urosevic M., Valasti P. and Koivisto E., 2012a. 3D reflection seismic imaging for open-pit mine planning and deep exploration in the Kevitsa Ni-Cu-PGE deposit, northern Finland. *Geophysics* **77** (5), WC95-WC108.
- Malehmir A., Schmelzbach C., Bongajum E., Bellefleur G., Juhlin C. and Tryggvason A., 2009. 3D constraints on a possible deep > 2,5 km massive sulphide mineralization from 2D crooked-line seismic reflection data in the Kristineberg mining area, northern Sweden. *Tectonophysics* **479** (3-4), 223-240.
- Matthews L., 2002. Base metal exploration: Looking deeper and adding value with seismic data. *CSEG Recorder* **27**, 37-43.
- Maxwell S. C. and Young R. P., 1992. Sequential velocity imaging and microseismic monitoring of mining-induced stress change. *Pure and Applied Geophysics* **139** (3-4), 421-447.
- McMillan W. J. and Panteleyev A., 1988. Porphyry copper deposits. *Geoscience Canada, Reprint Series* **3**, 45-58.
- Meyer L. and Owen M. L., 2013. NI 43-101 Technical Report for Neves-Corvo Mine and Semblana Deposit, Portugal. *Wardell Armstrong International Report Nr: MM779*, 1-224.
- Milkereit B., Berrer E., King A., Watts A., Roberts B., Adam E., Eaton D., Wu J. and Salisbury M., 2000. Development of 3-D seismic exploration technology for deep nickel-copper deposits—A case history from the Sudbury basin, Canada. *Geophysics* **65** (6), 1890-1899.
- Milkereit B., Eaton D., Wu J., Perron G., Salisbury M. H., Berrer E. K. and Morrison G., 1996. Seismic imaging of massive sulfide deposits; Part II, Reflection seismic profiling. *Economic Geology* **91** (5), 829-834.
- Milkereit B., Green A. and Sudbury Working Group, 1992. Deep geometry of the Sudbury structure from seismic reflection profiling. *Geology* **20** (9), 807-811.
- Morgan L. A., 2012. Geophysical Characteristics of Volcanogenic Massive Sulfide Deposits, in W. C. P. Shanks, III and R. Thurston, eds., Volcanogenic

- massive sulfide occurrence model: U.S. Geological Survey Scientific Investigations Report 2010-5070-C: USGS, 113-131.
- Nabighian M. and Asten M., 2002. Metalliferous mining geophysics—State of the art in the last decade of the 20th century and the beginning of the new millennium. *Geophysics* **67** (3), 964-978.
- Neil B., 2008. Resource and Reserve Update Neves-Corvo, Portugal. Lundin Mining Corporation: SEDAR
- Nelson R., 1984. Seismic reflection and mineral prospecting. *Exploration Geophysics* **15** (4), 229-250.
- NERC BGS, 2007. Mineral Profile : Copper: Natural Environmental Research Council - British Geological Survey
- O'Brien N. and West D., 2013. Key Elements for Mineral Exploration Success: an example from Neves-Corvo, Portugal: Lundin Mining Corporation Presented in Toronto Geological Discussion Group, Toronto. 1-33
- O'Doherty R. F. and Anstey N. A., 1971. Reflections on Amplitudes*. *Geophysical Prospecting* **19** (3), 430-458.
- Odgers A. T. R. and du Plessis A., 1993. Interpretation of a regional reflection seismic survey in the north-eastern Bushveld Complex: 3rd SAGA Biennial Conference and Exhibition, 125-129.
- Oldenburg D. W., Scheuer T. and Levy S., 1983. Recovery of the acoustic impedance from reflection seismograms. *Geophysics* **48** (10), 1318-1337.
- Oliveira J. T., Pacheco N., Carvalho P. and Ferreira A., 1997. The Neves Corvo Mine and the Paleozoic geology of Southwest Portugal., in F. Barriga and D. Carvalho, eds., Geology and VMS deposits of the Iberian Pyrite Belt: Society of Economic Geologists, Guide Book., 27, 21–72.
- Oliveira J. T., Pereira Z., Carvalho P., Pacheco N. and Korn D., 2004. Stratigraphy of the tectonically imbricated lithological succession of the Neves Corvo mine area, Iberian Pyrite Belt, Portugal. *Mineralium Deposita* **39** (4), 422-436.
- Oliviera J. T. and Quesada C., 1998. A comparison of stratigraphy, structure and palaeogeography of the south Portuguese zone and south-west England, European Variscides. *The Ussher Society Geoscience in South-west England* **9** (3), 141-150.
- Perron G., Eaton D. W., Elliot B. and Schmitt D., 2003. 13. Application of Downhole Seismic Imaging to Map Near-Vertical Structures: Normetal (Abitibi Greenstone Belt), Quebec, in D. Eaton, B. Milkereit and M. H. Salisbury, eds., Hardrock Seismic Exploration: SEG, Geophysical Development Series, 194-206.
- Pretorius C. C., Muller M. R., Larroque M. and Wilkins C., 2003. 16. A Review of 16 Years of Hardrock Seismics on the Kaapvaal Craton, in D. Eaton, B. Milkereit and M. H. Salisbury, eds., Hardrock Seismic Exploration: SEG, Geophysical Development Series, 247-268.
- Pretorius C. C., Trewick W. F., Fourie A. and Irons C., 2000. Application of 3-D seismics to mine planning at Vaal Reefs gold mine, number 10 shaft, Republic of South Africa. *Geophysics* **65** (6), 1862-1870.

- Prodehl C. and Mooney W. D., 2012. Exploring the Earth's crust: history and results of controlled-source seismology: Geological Society of America
- Read J., 1989. Seismic reflection investigations of the Hellyer orebody and Que-Hellyer volcanics, North West Tasmania. *Exploration Geophysics* **20** (1/2), 159-162.
- Relvas J. M., Barriga F. J., Ferreira A., Noiva P. C., Pacheco N. and Barriga G., 2006a. Hydrothermal alteration and mineralization in the Neves-Corvo volcanic-hosted massive sulfide deposit, Portugal. I. Geology, mineralogy, and geochemistry. *Economic Geology* **101** (4), 753-790.
- Relvas J. M., Barriga F. J. and Longstaffe F. J., 2006b. Hydrothermal alteration and mineralization in the Neves-Corvo volcanic-hosted massive sulfide deposit, Portugal. II. Oxygen, hydrogen, and carbon isotopes. *Economic Geology* **101** (4), 791-804.
- Ronen J. and Claerbout J. F., 1985. Surface-consistent residual statics estimation by stack-power maximization. *Geophysics* **50** (12), 2759-2767.
- Rosa C. J. P., McPhie J., Relvas J. M. R. S., Pereira Z., Oliveira T. and Pacheco N., 2008. Facies analyses and volcanic setting of the giant Neves Corvo massive sulfide deposit, Iberian Pyrite Belt, Portugal. *Mineralium Deposita* **43** (4), 449-466.
- Rosa D., Inverno C., Rosa C. J., Pereira Z., Andersen T., Oliveira J. T. and Matos J. X., 2012. New VMS exploration potential to the SE of Neves-Corvo mine, Iberian Pyrite Belt, Portugal: St. John's 2012 | Geoscience at the edge, GAC-MAC Joint Annual Meeting., GAC - MAC., 2 p.
- Roy B. and Clowes R. M., 2000. Seismic and potential-field imaging of the Guichon Creek batholith, British Columbia, Canada, to delineate structures hosting porphyry copper deposits. *Geophysics* **65** (5), 1418-1434.
- Ruskey F., 1981. High resolution seismic methods for hard rock mining, Premining investigations for hardrock mines: Proceedings: Bureau of Mines Technology Transfer Seminar, 4-28.
- Russel B. H., 1988. Introduction to seismic inversion methods.: SEG
- Rutter H. and Esdale D. J., 1985. The geophysics of the Olympic Dam discovery. *Exploration Geophysics* **16** (2/3), 273-276.
- Sáez R., Almodóvar G. R. and Pascual E., 1996. Geological constraints on massive sulphide genesis in the Iberian Pyrite Belt. *Ore Geology Reviews* **11** (6), 429-451.
- Sáez R., Pascual E., Toscano M. and Almodóvar G. R., 1999. The Iberian type of volcano-sedimentary massive sulphide deposits. *Mineralium Deposita* **34** (5-6), 549-570.
- Salisbury M. and Snyder D., 2007. Application of seismic methods to mineral exploration. *Mineral deposits of Canada: A synthesis of major deposit types, district metallogeny, the evolution of geological provinces, and exploration methods: Geological Association of Canada, Mineral Deposits Division, Special Publication* **5**, 971-982.

- Salisbury M. H., Milkereit B., Ascough G., Adair R., Matthews L., Schmitt D. R., Mwenifumbo J., Eaton D. W. and Wu J. J., 2000. Physical properties and seismic imaging of massive sulfides. *Geophysics* **65** (6), 1882-1889.
- Salisbury M. H., Milkereit B. and Bleeker W., 1996. Seismic imaging of massive sulfide deposits; Part I, Rock properties. *Economic Geology* **91** (5), 821-828.
- Sallarès V., Charvis P., Flueh E. R., Bialas J. and the SALIERI Scientific Party, 2005. Seismic structure of the Carnegie ridge and the nature of the Galápagos hotspot. *Geophysical Journal International* **161** (3), 763-788.
- Schermerhorn L. and Stanton W., 1969. Folded overthrusts at Aljustrel (South Portugal). *Geological Magazine* **106** (2), 130-141.
- Schmidt G., 1959. Results of Underground-Seismic Reflection Investigations in the Siderite District of the Siegerland. *Geophysical Prospecting* **7** (3), 287-290.
- Schneider W. A., 1978. Integral formulation for migration in two and three dimensions. *Geophysics* **43** (1), 49-76.
- Shanks W. C. P., III and Thurston R., 2012. Volcanogenic massive sulfide occurrence model: U.S. Geological Survey Scientific Investigations Report 345 p.
- Sheriff R. E., 1975. Factors affecting seismic amplitudes. *Geophysical Prospecting* **23** (1), 125-138.
- Sheriff R. E. and Geldart L. P., 1995. Exploration seismology, 2nd edition: Cambridge university press
- Sherwood J. W. C. and Poe P. H., 1972. CONTINUOUS VELOCITY ESTIMATION AND SEISMIC WAVELET PROCESSING. *GEOPHYSICS* **37** (5), 769-787.
- Shuey R. T., 1985. A simplification of the Zoeppritz equations. *Geophysics* **50** (4), 609-614.
- Singh S., 2004. Himalayan Tectonics (The HIMPROBE Results). *Gondwana Research* **7** (2), 635-636.
- Soriano C. and Casas J., 2002. Variscan tectonics in the Iberian Pyrite Belt, South Portuguese Zone. *International Journal of Earth Sciences* **91** (5), 882-896.
- Spencer C., Thurlow G., Wright J., White D., Carroll P., Milkereit B. and Reed L., 1993. A vibroseis reflection seismic survey at the Buchans Mine in central Newfoundland. *Geophysics* **58** (1), 154-166.
- Stolt R. H. and Benson A. K., 1986. Seismic migration: Theory and practice: Pergamon
- Strauss G., Madel J. and Alonso F. F., 1977. Exploration Practice for Strata-Bound Volcanogenic Sulphide Deposits in the Spanish-Portuguese Pyrite Belt: Geology, Geophysics, and Geochemistry, Time-and Strata-Bound Ore Deposits: Springer, 55-93.
- Strauss G. K. and Madel J., 1974. Geology of massive sulphide deposits in the Spanish-Portuguese Pyrite Belt. *Geologische Rundschau* **63** (1), 191-211.
- Taner M. T. and Koehler F., 1969. Velocity spectra - digital computer derivation applications of velocity functions. *Geophysics* **34** (6), 859-881.

- Taner M. T. and Koehler F., 1981. Surface Consistent Corrections. *Geophysics* **46** (1), 17-22.
- Taner T. M., Koehler K. and Alhilali K. A., 1974. Estimation and correction of near-surface time anomalies. *Geophysics* **39** (4), 441-463.
- Tatham R. H., Keeney J. W. and Noponen I., 1983. Application of the tau-p transform (slant-stack) in processing seismic reflection data. *Exploration Geophysics* **14** (3/4), 163-172.
- Telford W. M., Geldart L. P. and Sheriff R. E., 1990. Applied geophysics 2nd ed. Cambridge : Cambridge University Press.
- Tertyshnikov K., 2014. Seismic imaging in hard rock environments PhD Thesis, Curtin University.
- Tornos F., 2006. Environment of formation and styles of volcanogenic massive sulfides: The Iberian Pyrite Belt. *Ore Geology Reviews* **28** (3), 259-307.
- Urosevic M., 2013. What can seismic in hard rocks do for you?: ASEG-PESA 2013, 23rd International Geophysical Conference and Exhibition, CSIRO, 1-4.
- Urosevic M., Bhat G. and Grochau M. H., 2012. Targeting nickel sulfide deposits from 3D seismic reflection data at Kambalda, Australia. *Geophysics* **77** (5), Wc123-Wc132.
- Urosevic M. and Evans B., 1998. Seismic methods for the detection of kimberlite pipes. *Exploration Geophysics* **29** (3/4), 632-635.
- Urosevic M., Evans B. and Vella L., 2002. Shallow high-resolution seismic imaging of the Three Springs talc mine, Western Australia. *The Leading Edge* **21** (9), 923-926.
- Urosevic M. and Evans B. J., 2000. Surface and borehole seismic methods to delineate kimberlite pipes in Australia. *The Leading Edge* **19** (7), 756-758.
- Urosevic M., Evans B. J., Poole G., Seman M. and Basso L., 1995. Using seismic data and cross-hole analysis to image fractures. *Exploration Geophysics* **26** (2/3), 340-346.
- Urosevic M. and Juhlin C., 2007. An analysis of seismic information obtained from crooked line seismic surveys in crystalline rocks: Australia: 69th Annual International Conference and Exhibition, EAGE, 4 p.
- Urosevic M., Kepic A., Stolz E. and Juhlin C., 2007. Seismic exploration of ore deposits in Western Australia: Exploration in the new millennium: Proceedings of the Fifth Decennial International Conference on Mineral Exploration, 525-534.
- Van Houten F. B., 1973. Origin of red beds: a review-1961-1972. *Annual Review of Earth and Planetary Sciences* **1**, 39.
- White R. and Simm R., 2003. Tutorial: Good practice in well ties. *First Break* **21**, 75-86.
- Wiggins R. A., Larner K. L. and Wisecup R. D., 1976. Residual statics analysis as a general linear inverse problem. *Geophysics* **41** (5), 922-938.
- Wong J., Hurley P. and West G. F., 1983. Crosshole seismology and seismic imaging in crystalline rocks. *Geophysical Research Letters* **10** (8), 686-689.

- Wu J., Milkereit B. and Boerner D. E., 1995. Seismic imaging of the enigmatic Sudbury Structure. *Journal of Geophysical Research: Solid Earth* **100** (B3), 4117-4130.
- Yavuz S., Kinkela J., Dzunic A., Penney M., Araujo V., Neto R., Ziramov S., Pevzner R. and Urosevic M., 2015. Physical Property Analysis and Preserved Relative Amplitude Processed Seismic Imaging of Volcanogenic Massive Sulfides – A Case Study from Neves Corvo, Portugal. *Geophysical Prospecting - Hard Rock Seismic Imaging Special Issue* **63** (4), 798-812.
- Yavuz S., Kinkela J., Greenwood A., Penney M., Araujo V., Neto R., Dzunic A. and Urosevic M., 2013. Direct Targeting of VMS through Amplitude Consistent Seismic Imaging: 7th Congress of the Balkan Geophysical Society, EAGE, 5 p.
- Yavuz S., Kinkela J., Penney M., Araujo V., Neto R., Dzunic A. and Urosevic M., 2014. Direct VMS Targeting through Preserved Relative Amplitude Processed Seismic Imaging at Neves Corvo, Portugal: 76th EAGE Conference & Exhibition 2014 - Hard Rock Seismic Imaging Workshop, 5 p.
- Yavuz S., Tertyshnikov K., Strobach E. and Urosevic M., 2012. The Use of Seismic Methods for Imaging Complex Mineral Bodies in Hard Rock Environments: Near Surface Geoscience 2012–18th European Meeting of Environmental and Engineering Geophysics, 5 p.
- Yilmaz O., 2001. Seismic data analysis: Processing, inversion, and interpretation of seismic data: SEG
- Young R. P., Hutchins D. A., McGaughey J., Towers J., Jansen D. and Bostock M., 1989. Geotomographic imaging in the study of mining induced seismicity. *Pure and Applied Geophysics* **129** (3-4), 571-596.
- Zoeppritz K., 1919. On the reflection and propagation of seismic waves at discontinuities. *Erdbebenwellen VII B*, 66-84.

Every reasonable effort has been made to acknowledge the owners of copyright material. I would be pleased to hear from any copyright owner who has been omitted or incorrectly acknowledged.

Appendix

Copyright consent

From: Dick West <Dick.West@Lundinmining.com> Sent: Fri 13/03/2015 8:29
 To: Sinem Yavuz
 Cc: Milovan Urosevic
 Subject: RE: PhD Thesis Submission Request

Sinem

Thanks for the reminder on this request of yours. I have reviewed your thesis and you have LMC's approval to submit your thesis for examination on Friday 13th (which I am sure will be your very lucky day). You have consent for the copying and republishing of materials as proposed. There is no special form of acknowledgement required, you adequately acknowledged Lundin Mining and generously included my name as well.

You have spent a great deal of time poring over this data, analyzing the physical properties and developing an alternate method of processing which has enhanced the value of the data to the explorationist. I am no seismologist but I can see your efforts in your results and count ourselves lucky that we had such a dedicated and diligent scientist working on our data. You should be proud of your accomplishments. It is my hope that your thesis will help spur other companies to use seismology to help target mineralization and will also attract for researchers and funds to this special subset of seismology that I love so much - mineral exploration and discovery. Your thesis provides me with good background material and visuals and I did learn quite a bit from the chapters. I am sure I will continue to learn as I reread it.

I never told you but I originally looked at using seismics at NC in 2008 but at the time our then CEO did not want to invest in the technology. My next opportunity came when our leases were running and I started discussions with Peter Williams before the discovery hole was made at Semblana. Had we done the survey a year earlier then Semblana would have been a seismic discovery which would have been great for the tool.

Good luck with your dissertation and keep me posted on your completion and on the publication in Gp.

Sincerely
 Dick

From: Sinem Yavuz [mailto:sinem.yavuz@postgrad.curtin.edu.au]
Sent: Tuesday, March 10, 2015 9:43 AM
To: Dick West
Cc: Milovan Urosevic
Subject: PhD Thesis Submission Request

Dear Dick,

I would like to request permission to use Lundin Mining Corporation's data in my PhD thesis entitled "Seismic characterization of Volcanogenic Massive Sulfides – The Semblana Orebody, Portugal". I'll be submitting my PhD thesis for examination on Friday the 13th of March 2015.

I have uploaded the thesis on Dropbox (please see the link below) for your consideration and would greatly appreciate any feedback you could provide.

https://www.dropbox.com/s/fow6d1qh6fwyxr/thesis_for_permission.pdf?dl=0

Once completed, the thesis will be made available in hard-copy form in the Curtin Library and in digital form on the website: <http://library.curtin.edu.au/find-books-and-resources/theses.cfm>. The material will be provided strictly for educational purposes and on a non-commercial basis.

I would be most grateful for your consent to the copying and republishing of the material as proposed. Full acknowledgement of the ownership of the copyright and the source of the material will be provided in the thesis. I would be willing to use a specific form of acknowledgement that you may require and to communicate any conditions related to the use of this material.

I look forward to hearing from you and thank you in advance for your consideration of my request.

Best regards,

Regards

Sinem Yavuz | *PHD Student*

Department of Exploration Geophysics | Western Australian School of Mines

[Postal Address: GPO Box U1987, Perth, Western Australia, 6845] [Bld 613, Rm 4H23]
 [Street Address: ARRC/CSIRO Building, H Block, Level 4, 26 Dick Perry Avenue, Kensington, WA]

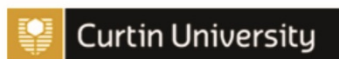
Tel | +61 8 9266 3521

Fax | +61 8 9266 3407

Mobile | +61 424 372717

Email | sinem.yavuz@postgrad.curtin.edu.au

Web | www.geophysics.curtin.edu.au



Curtin University is a trademark of Curtin University of Technology.
 CRICOS Provider Code 00301J (WA), 02537B (NSW)

30/01/2015

Web Content Display

[Print](#)

Permissions

SEG publishes journals, books, and digital works with the primary aim of disseminating research in and theory and applications of applied geophysics. Consistent with this objective, the Society provides mechanisms for those who seek to reuse or republish material from SEG publications while protecting the viability of the SEG publications program. Any further questions about permissions can be sent via email to the SEG publications department at permissions@seg.org.

Fair use

Authors and publishers may present or republish up to two figures or tables per SEG article or per SEG book without seeking written permission from SEG, provided that full acknowledgment of the source is provided in the new work. If SEG has cited a publication for which it is not the publisher, rights should be obtained from that publisher. SEG considers this fair use. There are no fees associated with this permission. Authors who need documentation that SEG is extending this permission are encouraged to print this message and present it to their publishers. Those who require further documentation should contact the SEG publications director. Requests to use any portion of "Seismic Data Analysis: Processing, Inversion, and Interpretation of Seismic Data" should be directed to the SEG publications director.

Permission granting

Those seeking permission to republish more material than described above should contact the SEG publications director. Such requests should include complete citations of works for which permission to republish is sought. If permission for specific figures or tables is sought, please provide figure and table numbers. Requests should include a description of the work in which the SEG material would be republished. Information about the audience and the intended distribution also should be included. The requests should be prepared on institutional letterhead if the requesting party is representing an institution. License fees are assessed only when the request is for a large amount of material or when the proposed usage is commercial in nature or would limit SEG's market. If a license fee is assessed, it must be paid prior to use or the permission is void.

Purchase redistribution rights online

Those seeking to redistribute SEG publications or portions thereof in print, by fax, or online may purchase permission to do so online. SEG publications are registered with the [Copyright Clearance Center](#), and licenses to redistribute SEG articles and portions of books are obtained through this nonprofit agency. Special pricing is available for university professors, including license to distribute SEG material through electronic course packs. Licenses also are available for distribution of journal articles and expanded abstracts via email or posting on Intranets and Extranets for limited time periods.

Authors' right to redistribute

Authors of articles in *GEOPHYSICS*, *INTERPRETATION*, *THE LEADING EDGE*, and the Technical Program *Expanded Abstracts* may post their own articles on their personal Web sites or the Web sites of their institutions without obtaining further permission from SEG. Authors of journal articles and *Expanded Abstracts* retain similar rights for print redistribution. If an author or an author's institution redistributes an author's article online or in print, the original publication venue encompassed in a complete citation and including SEG's status as publisher must be identified. Authors of SEG books, or portions of SEG books, must seek permission from the SEG publications director to redistribute these works in any form. Such permission will not be withheld if SEG's investment in the original publication of the works is not threatened. Questions should be directed to the publications director.

25/02/2015

Geological Association of Canada | Copyright

[HOME](#) [MEMBERSHIP](#) [AWARDS](#) [PUBLICATIONS](#) [EVENTS](#) [MÉLANGE](#) [CONTACT US](#)

Copyright

Copyright / Permissions

Copyright ownership:

Authors submitting articles to GAC for publication are considered to be the owner and originator of all material contained within. Extensive quotation or usage of previously published artwork requires proof of reprint permission from its owner.

Upon acceptance for publication, all copyright ownership transfers to GAC.

Fair Dealing/Fair Use policy:

Permission to use a single figure or table from any one manuscript published by GAC (including those appearing in a Special Paper, Short Course Notes volume, GeoText, Geolog issue, Geoscience Canada issue and Geoscience Canada Reprint Series volume, and —through agreement with their publishers— Paleontographica Canadana and Paleontology Division publications) is considered 'fair dealing' under the Canadian Copyright Act and 'fair use' by GAC, and no other permission need be granted, subject to the image being appropriately cited in all reproductions. The same fair dealing/fair use policy applies to sections of text up to 100 words in length.

Publishers requiring written permission should be advised that charges may apply.

Copying/Coursepacks:

GAC is a Publisher affiliate of Access Copyright, the Canadian copyright licencing agency. Refer all copying inquiries to Access Copyright:

The Canadian Copyright Licensing Agency
1 Yonge Street, Suite 800
Toronto, Ontario
M5E 1E5

www.accesscopyright.ca
1-800-893-5777
416-868-1620
416-868-1621 (fax)
info@accesscopyright.ca

Search

UPCOMING EVENTS

Joint Assembly AGU, CGU, GAC, and MAC
Montreal 3-7 May 2015

[Full listing of events](#)

CORPORATE MEMBERS

Tier I - Patrons:

Alberta Geological Survey
Anglo American Exploration (Canada) Ltd.
Department of Natural Resources (Government of Newfoundland & Labrador)
Memorial University of Newfoundland
Northwest Territories Geoscience Office
Yukon Department of Energy, Mines and Resources

Tier II - Sponsors:

British Columbia Geological Survey (BCGS)
Royal Tyrrell Museum of Palaeontology
Saskatchewan Geological Survey

Tier III - Supporters:

Activation Laboratories Ltd.
Elemental Controls Ltd.
Franklin Geosciences Ltd.
Geoscience Laboratories
IBK Capital Corp
Isomass Scientific Ltd.
Living Sky Geophysics Inc.

Tier IV - Universities:

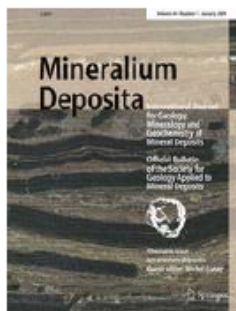
Acadia University
Institut national de la recherche scientifique (INRS)
Laurentian University
McGill University
Université de Genève
Université du Québec à Montréal
University of New Brunswick
University of Toronto
University of Waterloo

19/02/2015

RightsLink® by Copyright Clearance Center



Home Account Info Help Live Chat



Title: The volcanic-hosted massive sulphide deposits of the Iberian Pyrite Belt Review and preface to the Thematic Issue
Author: J. M. Leistel
Publication: Mineralium Deposita
Publisher: Springer
Date: Jan 1, 1997
 Copyright © 1997, Springer-Verlag Berlin Heidelberg

Logged in as:
 Sinem Yavuz
 LOGOUT

Order Completed

Thank you very much for your order.

This is a License Agreement between Sinem Yavuz ("You") and Springer ("Springer"). The license consists of your order details, the terms and conditions provided by Springer, and the [payment terms and conditions](#).

[Get the printable license.](#)

License Number	3572301337402
License date	Feb 19, 2015
Licensed content publisher	Springer
Licensed content publication	Mineralium Deposita
Licensed content title	The volcanic-hosted massive sulphide deposits of the Iberian Pyrite Belt Review and preface to the Thematic Issue
Licensed content author	J. M. Leistel
Licensed content date	Jan 1, 1997
Volume number	33
Issue number	1
Type of Use	Thesis/Dissertation
Portion	Figures
Author of this Springer article	No
Original figure numbers	Fig. 1
Title of your thesis / dissertation	Seismic characterization of Volcanogenic Massive Sulfides – The Semblana orebody, Portugal
Expected completion date	Mar 2015
Estimated size(pages)	150
Total	0.00 USD

CLOSE WINDOW

Copyright © 2015 Copyright Clearance Center, Inc. All Rights Reserved. [Privacy statement](#).
 Comments? We would like to hear from you. E-mail us at customercare@copyright.com

19/02/2015

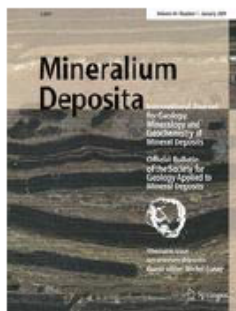
Rightslink® by Copyright Clearance Center



Home

Account Info

Help



Title: Stratigraphy of the tectonically imbricated lithological succession of the Neves Corvo mine area, Iberian Pyrite Belt, Portugal

Author: J. Tomás Oliveira

Publication: Mineralium Deposita

Publisher: Springer

Date: Jan 1, 2004

Copyright © 2004, Springer-Verlag

Logged in as:
Sinem Yavuz

LOGOUT

Order Completed

Thank you very much for your order.

This is a License Agreement between Sinem Yavuz ("You") and Springer ("Springer"). The license consists of your order details, the terms and conditions provided by Springer, and the [payment terms and conditions](#).

[Get the printable license.](#)

License Number	3572300958061
License date	Feb 19, 2015
Licensed content publisher	Springer
Licensed content publication	Mineralium Deposita
Licensed content title	Stratigraphy of the tectonically imbricated lithological succession of the Neves Corvo mine area, Iberian Pyrite Belt, Portugal
Licensed content author	J, Tomás Oliveira
Licensed content date	Jan 1, 2004
Volume number	39
Issue number	4
Type of Use	Thesis/Dissertation
Portion	Figures
Author of this Springer article	No
Original figure numbers	Fig. 1
Title of your thesis / dissertation	Seismic characterization of Volcanogenic Massive Sulfides – The Semblana orebody, Portugal
Expected completion date	Mar 2015
Estimated size(pages)	150
Total	0.00 USD

CLOSE WINDOW

Copyright © 2015 [Copyright Clearance Center, Inc.](#) All Rights Reserved. [Privacy statement](#).
Comments? We would like to hear from you. E-mail us at customercare@copyright.com